Dissertation

Optimisation of an Optomechanical Transducer and its Application as Electric Field Sensor

ausgeführt zum Zwecke der Erlangung des akademischen Grades eines Doktors der technischen Wissenschaften, eingereicht am

Institut für Sensor- und Aktuatorsysteme
Technische Universität Wien

vorgelegt von:
Andreas Kainz
A-1080 Wien

betreut von:
Ao. Univ. Prof. Dr. Franz Keplinger
Dr. Wilfried Hortschitz

Wien, im August 2017

Eidesstattliche Erklärung

Ich erkläre an Eides statt, dass ich die vorliegende Dissertation selbstständig und ohne fremde Hilfe verfasst, andere als die angegebenen Quellen und Hilfsmittel nicht benutzt bzw. die wörtlich oder sinngemäß entnommenen Stellen als solche kenntlich gemacht habe.

Wien, August 2017

Unterschrift (Andreas Kainz)

Wenn wir wüssten, was wir tun, würden wir es nicht Forschung nennen.
- Albert Einstein

Contents

Abstract

This thesis focuses on the physical properties of a highly displacement-sensitive optomechanical transducer based on MEMS technology. Depending on the concrete design, these transducers can be used as sensors for various quantities, e.g. acceleration, vibration, magnetic field or even electric field. One aim of this work was to better understand and optimise the physical properties of the mechanical components and the optical sensitivity. One of the major findings of this part was an accurate analytical model describing the damping of the mechanical structure. The accuracy of this model can compete with computationally expensive and lengthy numerical calculations. Therefore, it can be used to tailor and optimise the characteristic of device already in the design step. In addition, several approaches to improve the optomechanical sensitivity and efficiency of the transducer were explored. Thereby, the collimation of the incident light proved to be the most effective approach.

Another aim was to implement an electric field sensor for low-frequency and constant electric fields based on the optomechanical readout. Since the electromechanical transduction of this sensor, based on electrostatic induction, is completely new, the physical properties, e.g. that the force depends on the square of the electric field, had to be established. The dynamic behaviour of the sensor was analysed numerically and – to a certain extent – analytically. Measurements conducted with actual MEMS devices agree very well with these analyses. Furthermore, it was shown that the experimental results are reproducible and that with the presented sensors, an electric field resolution limit as low as 173 $\mathrm{V/m/\sqrt{Hz}}$ can be achieved. In addition, it was outlined how the layout of future sensors can be designed in order to achieve resolutions in the order of 1 $\mathrm{V/m/\sqrt{Hz}}$.

Since mechanical vibrations or acoustic interferences pose a source of disturbance for these E-field sensors, another, more resilient sensor design was explored. In this design, the mechanical motion induced by the electrostatic force is a rotation rather than a translation. Two different kinds of suspensions (one based on straight beams, one based on U-shaped beams) were investigated with respect to their E-field sensitivity and resilience to interferences. It was shown that, while for both types the mechanical interferences couple less to the sensors, only the sensors with U-shaped beam suspension exhibit a satisfying sensitivity.

Kurzfassung

Diese Dissertation behandelt die physikalischen Eigenschaften eines hochgradig positionsempfindlichen optomechanischen Wandlers, der auf MEMS Technologie basiert. Abhängig vom konkreten Design können diese Wandler als Sensoren für unterschiedliche Größen, wie etwa Beschleunigungen, Vibrationen, Magnetfelder oder elektrische Felder, eingesetzt werden. Ein Ziel diser Arbeit war es, die physikalischen Eigenschaften der mechanischen Komponenten und optischen Empfindlichkeit besser zu verstehen und zu optimieren. Eine der wichtigsten Resultate dieses Teils war ein akkurates analytischel Modell, das die Dämpfung der mechanischen Struktur beschreibt. Die Genauigkeit dieses Modells kann mit aufwändigen und langwierigen numerischen Simulationen mithalten. Es kann daher dazu verwendet werden die Charakteristik des Sensors schon in der Designphase maßzuschneidern und zu optimieren. Weiters wurden mehrere Ansätze zur Verbesserung der optomechanischen Empfindlichkeit und Effizienz des Wandlers untersucht. Dabei hat sich die Kollimierung des einfallenden Lichtes als am effizientesten herausgestellt.

Ein anderes Ziel der Arbeit war es, basierend auf dem optomechanischen Wandler einen Sensor für niederfrequente und statische elektrische Felder zu implementieren. Nachdem die elektromechanische Wandlung, die auf dem Phänomen der Influenz beruht, komplett neu ist, mussten ihre physikalischen Eigenschaften, z.B. die quadratische Abhängigkeit der Kraft vom elektrischen Feld, hergeleitet werden. Das dynamische Verhalten des Sensors wurde numerisch und zum Teil auch analytisch analysiert. Messungen, die mit gefertigten Sensoren durchgeführt wurden, stimmten sehr gut mit diesen Analysen überein. Außerdem wurde gezeigt, dass die experimentellen Ergebnisse reproduzierbar sind und dass mit den präsentierten Sensoren eine Auflösungsgrenze von 173 $\mathrm{V/m/\sqrt{Hz}}$ erreicht werden kann. Weiters wurde skizziert, wie das Layout der Sensoren ausgelegt werden kann um Auflösungsgrenzen in der Größenordnung von 1 $\mathrm{V/m/\sqrt{Hz}}$ zu erreichen.

Da mechanische Vibration und akustische Einflüsse eine Störquelle für diese E-Feldsensoren darstellen, wurde auch ein anderes, widerstandsfähigeres Design untersucht. In diesem Design ist die mechanische Bewegung, die durch die elektrostatische Kraft hervorgerufen wird, eine Rotation statt einer Translation. Zwei verschiedene Arten von Aufhängungen (eine basierend auf geraden Balken, eine basierend auf U-förmigen Balken) wurden im Hinblick auf ihre Empfindlichkeit auf E-Felder und auf ihre Widerstandsfähigkeit gegenüber der Störquellen untersucht. Es wurde gezeigt, dass die mechanischen Interferenzen zwar beide Typen weniger stark einkoppeln, aber dass nur die Sensoren mit U-förmigen Balken eine befriedigende Empfindlichkeit aufweisen.

Acknowledgment

First of all, I would like to express my gratitude towards Prof. Franz Keplinger and Dr. Wilfried Hortschitz for supervising this thesis and giving me the opportunity to work in the field of MEMS sensors and actuators.

I also would like to thank my dear colleagues and coworkers at the Institute of Sensor and Actuator Systems at TU Wien and the Center of Integrated Sensor Systems of the Danube University Krems outpost in Wiener Neustadt, who were always supportive and with whom working together was a great pleasure. Especially, Dr. Artur Jachimowicz, Dr. Johannes Schalko and their team were of tremendous importance for this thesis, because without them there would not be any working MEMS devices. Furthermore, I owe a lot to the support in the form of discussions, advice, insight and great atmosphere provided by Roman Beigelbeck, Jörg Encke, Thomas Glatzl, Dr. Franz Kohl and Dr. Michael Stifter.

I want to thank Prof. Thilo Sauter and Dr. Thomas Schrefl for kindly agreeing to appraise my thesis even on relatively short notice.

Many thanks also to my family for their patience. Last but foremost, I am also very grateful to my girlfriend Amália who always encouraged and supported me and for correcting my Viennese English.

This work was financially supported by the Austrian Science Fund (FWF projects number TRP 226-N24 and P 28404-NBL) and the FFG project Cosiflex co-funded as part of the M-ERA.Net and the Austrian Ministry for Transport, Innovation and Technology (BMVIT).

Introduction

Due to their vast number of possible applications and high level of integration, microelectromechancal systems (MEMS) have over the last decades spread from basic research to industry or consumer electronics [1–5]. This success is partly owed to the level of miniaturisation and to the silicon technology which was not just slightly driven by the advances in microprocessor fabrication. One of the first MEMS sensors that entered the mass market was the airbag sensor, which paved the way for large-scale development and improvement of MEMS devices. Nowadays, with increasing reliability and sensitivity, the demand for MEMS is ever rising. Sensors and sensor systems in general are one of the most important driving factors in the current development of autonomous industry (*Industry 4.0*) or autonomous navigation [6]. Further miniaturisation down to the nano scale (NEMS) even made it feasible to enter the realm of quantum physics by cooling it into its ground state [7,8]. Thus, developing new and improving existing sensing concepts is key for pushing forward state-of-the-art science and technology.

Ever since the development of the airbag sensor, inertial MEMS sensors have made up a large part of the commercial sensors. These include – among others – gyroscopes, accelerometers or vibration sensors. In general, they consist of an inertial, moveable part coupled to a fixed frame and work by transducing the relevant input quantity, e.g. an input acceleration, to a relative displacement between these components [4, 5]. Most of these devices on the mass market rely on sophisticated capacitive readouts that convert the displacement into an electrical output signal. However, these readouts offer good but limited sensitivity and feature some intrinsic drawbacks that call for immense effort to overcome. For example, the capacitive transduction is most effective, if the distance between fixed and moving electrode is small. This leads to small gaps, which, in turn, limit the possible deflection. Furthermore, if the moving electrode is too close to the fixed one, the device becomes unstable an the so-called pull-in happens. This effect causes the rapid collision of the electrodes which will often severely damage the device. The answer to this constraint is an active force feedback that prevents contact of the electrodes but also complicates the device.

Apart from the very common capacitive readouts, also a number of other mechanisms exists, e.g. piezoresistive, piezoelectric, tunneling or optical, each with their own advantages and disadvantages [4,5]. Piezoresistive sensors have the advantage of being easy to fabricate, but they are usually very noisy. Piezoelectric sensors generate their output self-sufficiently needing no voltage supply, but they are burdensome to manufacture and cannot be used for DC measurements. Tunneling sensors are very sensitive and relatively easy to fabricate, but, due to the extremely small gap spacings (~ 1 nm) required for the tunneling current, they need an active feedback to avoid closing of the gap. Optical sensors can themselves be divided in sub-categories, e.g. intensity and phase sensitive devices, that each have their own properties [9–12]. They all, however, have in common high sensitivity and low noise, but in most cases also the necessity for an extensive setup.

In contrast to these optical MEMS, the readout treated in this thesis does not depend on bulky setups [13,14]. The rather simple transduction concept works similar to an optical shutter by modulating a light flux that passes through the MEMS part. The MEMS shutter consists of two identical arrays of holes which, depending on their relative position, are letting more or less light pass. This change in the light flux is detected and yields an output proportional to the change in relative position. Apart from the micromechanical shutter, merely low-cost optoelectronical components such as LEDs and photodiodes/-transistors and a readout circuit are necessary. In addition to the simplicity of the transduction, the MEMS has only few design constraints. For example, it does not require small gap spacings or electrical connections. The latter is especially interesting, since it enables label-free sensing. This property can be exploited for almost perturbation-free electric field sensing.

Objective and Structure of the Thesis

The objective of this thesis is to improve the optomechanical transducer and to optimise it for the given application. Within the scope of this work, these applications are vibration sensing/accelerometry and electric field sensing. The optimisation encompasses the lumped mechanical parameters (resonance frequency ω_0 and dissipation in the form of either the decay parameter γ or the damping parameter d) and the sensitivity of the transducer.

The thesis is organised in the following way:

First, the optomechanical transducer is introduced in chapter 1 explaining its fundamental readout principle and properties. Furthermore, the general mechanical behaviour and the optical sensitivity are explained. The final part of the chapter focuses on the unique electromechanical transduction principle for the application as electric field sensor.

In chapter 2, ways to optimise the damping and the quality factor are shown. These are based on an analytical model for the damping parameter d which was developed within the scope of this thesis. Starting with some analytical background on fluid dynamics, the model is developed and then tested both against numerical calculations and measurements of test structures. Towards the end of the chapter, results of MEMS vibration sensors are presented which are optimised for low Q.

Subsequently, the optomechanical readout itself is subject to optimisation in chapter 3. Several aspects and approaches are explored to increase the sensitivity of the transduction. This includes varying the number of holes, applying optical lenses, diffraction gratings or organic optoelectronics which are promising also in other prospects.

The application as electric field sensor is presented in chapter 4. There, it is shown how to implement the optomechanical readout with the electromechanical transduction. Several device layouts based on numerical simulations are fabricated and tested successfully. Furthermore, rotational devices which offer a better resilience against interfering mechanical disturbances have been investigated.

Chapter 1.

The Optomechanical Transducer

This chapter introduces the transduction mechanism exploited within the scope of this thesis. It is shown how this mechanism can be implemented to measure mechanical quantities such as accelerations or vibrations or electric quantities such as voltages or electric fields.

1.1. Transduction Principle

The optomechanical transducer works similar to an optical shutter and is built up by two chips – one glass and one silicon chip – which are bonded on top of each other. The silicon chip comprises the moveable part of the MEMS which consists of a suspended plate. This plate features an array of holes forming one part of the shutter. The other part is placed on the glass chip. There, the same pattern of holes is achieved by depositing chromium on the glass. A schematic of the transducer is depicted in Fig. 1.1. Note that, due to better visibility, the figure exhibits holes in Si and Cr covers on glass, while the devices treated in this thesis are hole over hole combinations only. These two cases – cover over hole and hole over hole – are equivalent, but due to lower offset light, the hole over hole option is preferable.

Throughout this thesis the holes are of rectangular shape. In general, they can have arbitrary forms [14, 15]. Different forms lead to different light transmission responses with regard of the relative translation of the two gratings. The pairing of different shapes can be used to, e.g., implement a non-linear transmission response. This can increase the measurement accuracy or linearise a nonlinear transduction characteristic.

For holes of rectangular shape, the overlap of a static and a moving hole and, therefore, the area A_{open} permeable for light is also rectangular. If this hole is perfectly aligned in y-direction, the overlap is determined by the width of the hole w_{h}, the relative shift in

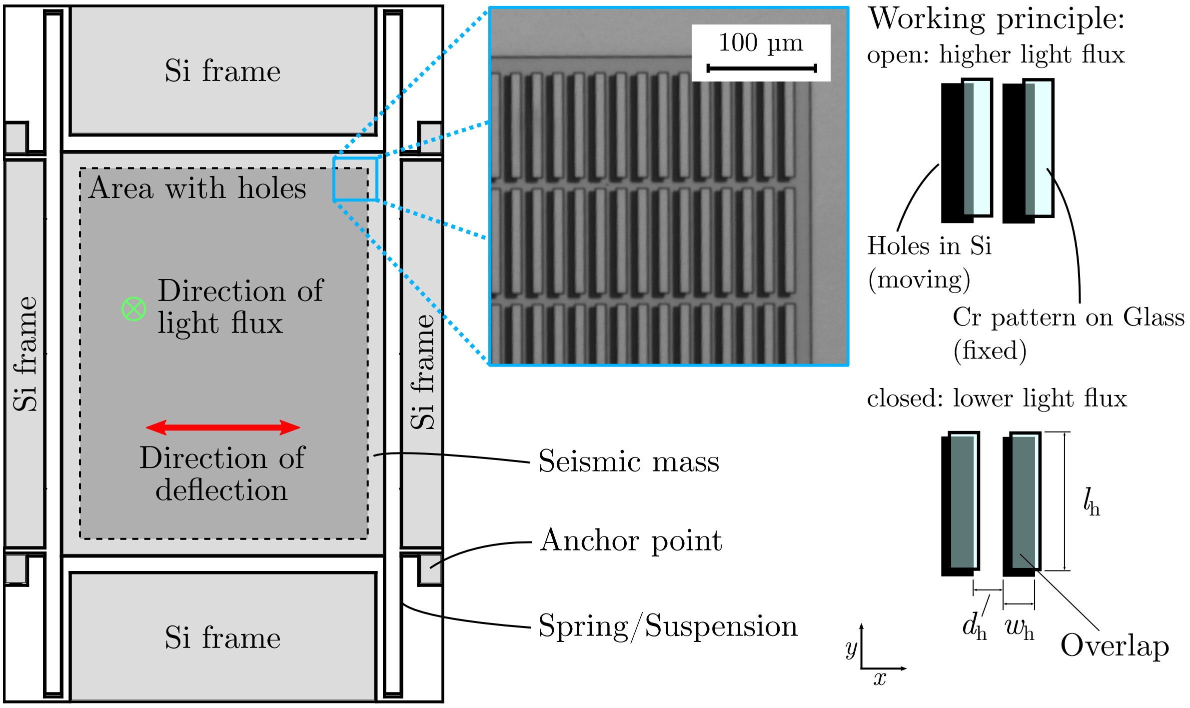

Figure 1.1.: Schematic and possible layout of the optomechanic transducer. The moveable silicon plate is suspended by four U-shaped beams. The darker region marks the array of holes through which a perpendicular light flux is directed. Together with the same pattern of Cr on glass (see the zoomed micrograph), the amount of light that can pass through the device depends on the relative displacement between Si and Cr grid (bottom right).

x-direction s_x and the length of the hole l_h and can be expressed as $A_\mathrm{open} = l_\mathrm{h}(w_\mathrm{h} - s_x)$. For the sake of completeness, if there is a shift in y-direction s_y, e.g. due to alignment errors during fabrication, this reads $A_\mathrm{open} = (l_\mathrm{h} - s_y)(w_\mathrm{h} - s_x)$. Since this shift is usually small and the transducer is susceptible to deflections in x-direction only, it will not be considered from here on. On the other hand, s_x is essential. It determines the resting position and, hence, the maximum detectable distance the moving hole can be displaced until the open area is either zero or equal to the area of one hole $A_\mathrm{h} = l_\mathrm{h} w_\mathrm{h}$. This means $0 \leq A_\mathrm{open} \leq A_\mathrm{h}$. Ideally, the resting position is $s_x = w_\mathrm{h}/2$ which allows a maximum travel range of $|\delta x| = w_\mathrm{h}/2$ in both directions.

The transducer contains not only one pair of holes, but a large number N_h of them. The spacing between the holes needs to be large enough to ensure that one hole can overlap only with one other hole. Otherwise, the light flux would not be proportional to the relative position. This means the pitch d_h in x-direction has to be at least equal to the width of the hole $d_\mathrm{h} \geq w_\mathrm{h}$. The distance in y-direction can be chosen freely, since there will be no relative movement in this direction.

1.1.1. Sensitivity

The sensitivity S of the transducer is given by the change of the output signal δU with respect to the input quantity, in this case the input displacement δx, i.e. $S = \delta U/\delta x$. Any displacement of the moving grid around the resting position causes a change in the open area of each pair of holes $\delta A_\mathrm{open} = l_\mathrm{h}(w_\mathrm{h} - s_x + \delta x) - l_\mathrm{h}(w_\mathrm{h} - s_x) = l_\mathrm{h}\delta x$. Therefore, the total change in the open area is given by $\delta A_\mathrm{open} = \alpha_1 \delta x = N_\mathrm{h} l_\mathrm{h} \delta x$.

This change in the open area effects a change in the light flux $\delta\Phi = \alpha_2 \delta A_\mathrm{open} = (1 - r)E_\mathrm{e}\delta A_\mathrm{open}$ that is able to pass through the optical shutter. The quantity E_e is the (energetic) irradiance on the device and the term $(1 - r)$ accounts for the reflective losses on the glass chip. The photodetector (-diode or -transistor) converts this transmitted light flux into a photocurrent $\delta i = \alpha_3 \delta\Phi = e\eta_\mathrm{q}\delta\Phi$ with e being the charge of an electron and η_q the quantum efficiency of the photodiode. This is finally transformed into the output voltage $\delta U = \alpha_4 \delta i = -R\delta i$ by a transimpedance amplifier with feedback resistance R. Putting together every sub-transduction, the overall sensitivity is given by

$$S = \frac{\delta U}{\delta i}\frac{\delta i}{\delta \Phi}\frac{\delta \Phi}{\delta A_\mathrm{open}}\frac{\delta A_\mathrm{open}}{\delta x} = \prod_{i=1}^{4} \alpha_i = -N_\mathrm{h} l_\mathrm{h} (1 - r) E_\mathrm{e} e \eta_\mathrm{q} R. \tag{1.1}$$

Therefore, high sensitivity can be achieved by increasing a number of quantities. First of all, the product $N_\mathrm{h} l_\mathrm{h} =: L_\mathrm{h}$ which defines the effective edge length of the optical shutter corresponds to the intrinsic sensitivity of the device. The other tunable factors, i.e. E_e and R are given by external light source and circuitry, respectively. To a much smaller extent, also the reflective losses $(1 - r)$ can be minimised by, say, anti-reflection coating on glass or a detector with high quantum efficiency η_q can be chosen.

1.2. Mechanical Response

The mechanical response of the MEMS determines the magnitude of the relative displacement δx for a given input quantity or actuation. In contrast to the sensitivity discussed in the previous section, the correlation between the actuation and δx is not independent of the frequency. A device as in Fig. 1.1 can be understood in a lumped parameter approach as damped, driven, harmonic oscillator. The corresponding parameters are the stiffness

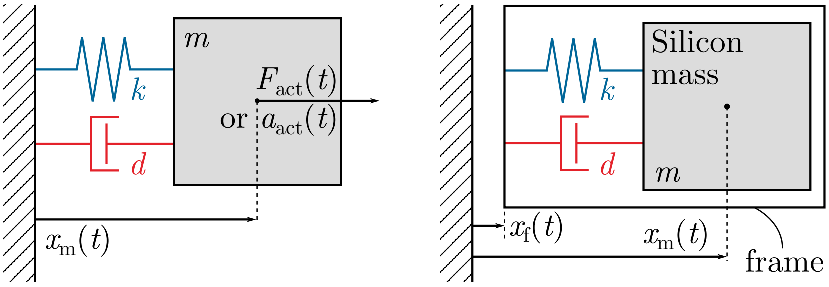

Figure 1.2.: Comparison of the two cases of the oscillator in the lumped parameter picture. The left one describes a force sensor or accelerometer. Here the actuation force F_{act} or acceleration a_{act} affects the mass directly. On the right, the model of a vibration sensor is shown. The input vibration x_{f} is exerted onto the frame, onto which the mass is coupled. The observed displacement corresponds to the difference $x = x_{\mathrm{m}} - x_{\mathrm{f}}$.

of the suspension k, the mass m and the damping parameter d. The actuation can be provided by an external force $F_{\mathrm{act}} = F\mathrm{e}^{\mathrm{i}\omega t}$ or acceleration $a_{\mathrm{act}} = A\mathrm{e}^{\mathrm{i}\omega t}$ that take effect on the mass directly or by a vibration with amplitude $x_{\mathrm{f}} = X_0\mathrm{e}^{\mathrm{i}\omega t}$ that acts on the frame. A comparison of these two cases is shown in Fig. 1.2. The first case corresponds to a force- or acceleration-sensitive MEMS, the second to a vibration-sensitive one. While the parameters for these two cases are the same, the mechanical response differs.

Introducing the decay parameter $\gamma = d/2m$ and the (angular) resonance frequency $\omega_0 = \sqrt{k/m}$, the equation of motion for the oscillator reads

$$\frac{\mathrm{d}^2x}{\mathrm{d}t^2} + 2\gamma\frac{\mathrm{d}x}{\mathrm{d}t} + \omega_0^2 x = \begin{cases} \frac{F}{m}\,\mathrm{e}^{\mathrm{i}\omega t} = a\,\mathrm{e}^{\mathrm{i}\omega t} & \text{force sensor, accelerometer} \\ -X_0\omega^2\mathrm{e}^{\mathrm{i}\omega t} & \text{vibration sensor} \end{cases} . \tag{1.2}$$

Note that the displacement variable x corresponds to the observed quantity δx as in subsection 1.1.1. For the accelerometer, it is given by $x = x_{\mathrm{m}}$, for the vibration sensor as $x = x_{\mathrm{m}} - x_{\mathrm{f}}$.

This ordinary differential equation can be solved with an exponential ansatz $x(t) = X(\omega)\mathrm{e}^{\mathrm{i}\omega t}$ leading to the amplitude function

$$A(\omega) = \frac{1}{\omega^2 - \omega_0^2 - 2\mathrm{i}\gamma\omega} \cdot \begin{cases} -\frac{K}{m}, -a & \text{force sensor, accelerometer} \\ X_0\omega^2 & \text{vibration sensor} \end{cases} . \tag{1.3}$$

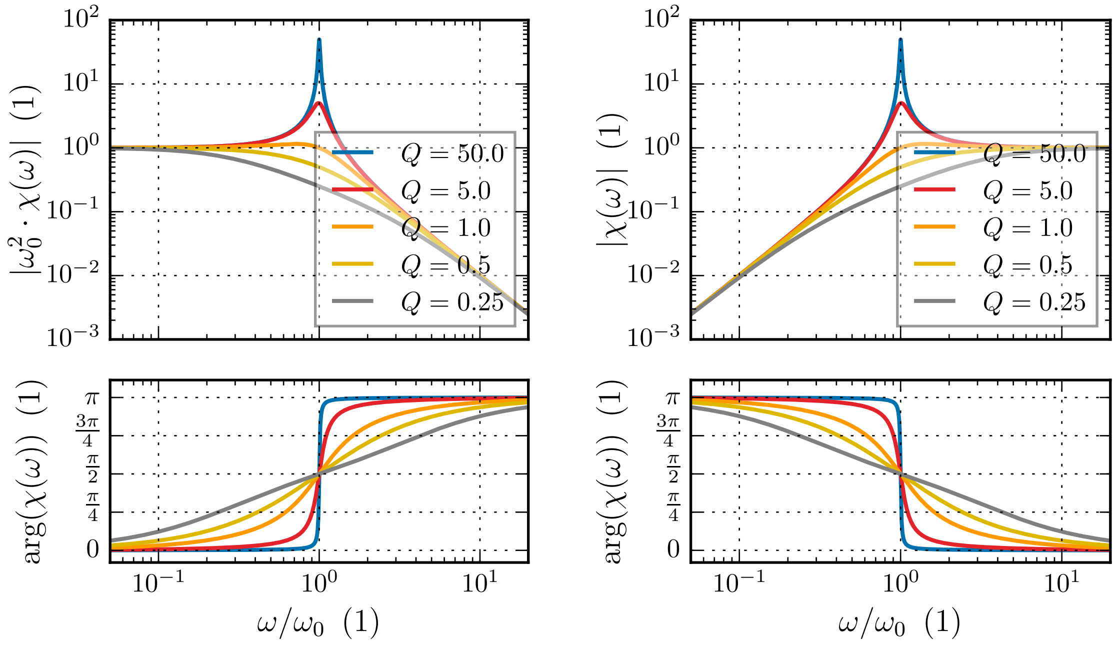

(a) Accelerometer/Force sensor (b) Vibration sensor

Figure 1.3.: Mechanical frequency response of the mass (a) and base (b) excited case for different values of the quality factor Q.

Dividing $A(\omega)$ by the excitation gives the frequency response

$$\chi(\omega) = \frac{A(\omega)}{\{F/m, a, X_0\}} = \frac{1}{\omega^2 - \omega_0^2 - 2\mathrm{i}\gamma\omega} \cdot \begin{cases} -1 & \text{force sensor, accelerometer} \\ \omega^2 & \text{vibration sensor} \end{cases}, \tag{1.4}$$

which is also referred to as transfer characteristic or sometimes as mechanical susceptibility. Fig. 1.3 shows the amplitude and the phase of the two cases of the mechanical response. If the mass is subjected to the excitation directly (Fig. 1.3a), the magnitude of response is approximately constant for frequencies below the resonance, i.e. $\chi(\omega < \omega_0) \approx \omega_0^{-2}$ and decreases proportional to ω^{-2} for frequencies above the resonance, $\chi(\omega > \omega_0) \approx \omega^{-2}$. At the resonance, the magnitude reaches its maximum $\chi(\omega_0) = (2\gamma\omega_0)^{-1}$ forming the resonance peak. Here, the phase turns by $+\pi$.

In the base excited case (Fig. 1.3b), the magnitude increases below the resonance $\chi(\omega < \omega_0) \approx \omega^2/\omega_0^2$ and is constant $\chi(\omega > \omega_0) \approx 1$ above the resonance. The height of the resonance peak is given by $\chi(\omega_0) = \omega_0/2\gamma = Q$ where Q is the mechanical quality factor. The phase turns by $-\pi$.

Analogous to the dimensionless numbers of the similitude in fluid mechanics, the quality factor Q describes the mechanical oscillator almost completely. It is defined as the ratio of the energy stored to the energy dissipated per cycle in the oscillator. Hence, a high value of $Q \gg 1$ means that the damping of the system is weak and a lot of kinetic energy can be stored. This is synonymous with a high and sharp resonance peak and with a slow decay, i.e. ring down, of the oscillation amplitude. Low values of $Q < 1$ correspond to heavily damped systems. The ring down is complete in less than a period $T = 1/f_0 = (2\pi\omega_0)^{-1}$ and the amplitude is strongly reduced. For $Q = 1$, stored energy and dissipation are balanced. The resonance peak is degenerated and on par with the flat region of the magnitude curve.

Depending on the application for the MEMS, different values of Q are favourable. For example, a resonant force sensor is best suited with a high quality factor, since the response is then (at least) by a factor Q higher than for frequencies $\omega \neq \omega_0$. In contrast to that, for a vibration sensor $Q \approx 1$ is a good choice. This is due to the fact that vibrations, in general, comprise a broad spectrum of frequencies and, therefore, the measurement range lies in the flat region above the resonance $\omega > \omega_0$. There is no need for a high peak. Furthermore, a long ring down time $1/\gamma$ is rather obstructive for this kind of application.

1.3. Response to Electric Fields

In order to use the optomechanical transducer as sensor for electric fields, an effect is needed that converts the electric field $\mathbf{E}$ to a relative displacement between the two arrays of holes. Such an effect is given by the electrostatic induction which exploits the finite charge carrier mobility in silicon which can be treated as ideal conductor within the scope of this subsection. If a conductor is placed inside an electric field, charges inside the conductor will rearrange themselves on the surface in order to neutralise the electric field inside the conductor. This happens due to the Coulomb force acting onto the carriers that vanishes when the field is compensated. Hence, the interior of a conductor is field-free.

Since the body of the conductor is neutral in total, there is both a positively and a negatively charged surface region on the conductor. If one imagines a conductive spring between these regions, the pull experienced by these surfaces will expand the spring as depicted in the schematic Fig. 1.4. Thus, the electric field is transduced into a mechanical displacement. Note that since the accumulating charges neutralise the field inside the conductor, the force experienced by the surface is always directed away from the conductor regardless of the direction of $\mathbf{E}$.

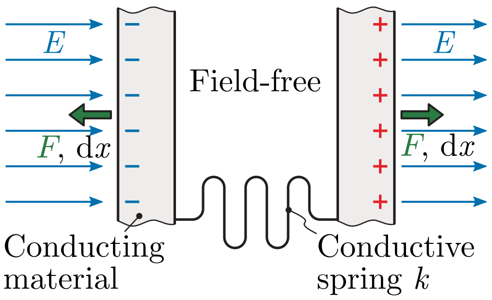

Figure 1.4.: Transduction principle for electric field sensing. The induced surface charges experience an outward force that acts against a conductive spring.

In the case of a conducting sphere inside a homogeneous electric field, the pull experienced by the oppositely charged halves of the sphere can be calculated analytically. Analytical calculation of the force acting on conductors of arbitrary geometry is much more challenging or even impossible. The qualitative behaviour, however, is the same. Therefore, the force acting on the sphere is derived here as an illustrative example which can be found in numerous text books in literature, e.g. [16–18].

The conducting sphere of radius R is placed inside a uniform electric field $\mathbf{E}_0 = E_0\mathbf{e}_\mathrm{z}$ pointing in z-direction. The corresponding potential φ_0 can, thus, be written $\phi_0 = -E_0 z$. Due to the properties of conductors mentioned above, the electric field and, hence, the potential are distorted in the vicinity of the sphere. This can be accounted for by adding the sphere's contribution ϕ_s to the potential of the uniform field yielding the total potential $\phi = \phi_0 + \phi_\mathrm{s}$. This potential has to fulfill Laplace's equation $\Delta\phi = 0$. A general solution to Laplace's equation in spherical coordinates (r, ϑ, φ) [17] is given by

$$\phi = (C_1 r^l + C_2 r^{-(l+1)})(C_3 \cos m\varphi + C_4 \sin m\varphi)[C_5 P_l^m(\cos\vartheta) + C_6 Q_l^m(\cos\vartheta)], \qquad (1.5)$$

where C_i are coefficients and l, m are integer parameters with $l \geq 0$ and $-l \leq m \leq +l$. The functions P_l^m and Q_l^m are the Legendre polynomials and Legendre functions of the second kind, respectively.

Taking into account the symmetry of the problem, it is obvious that $m = 0$. Furthermore, the potential or at least the corresponding electric field is required to be finite, thus, $C_6 = 0$ and $l < 2$. This leads to

$$\phi = \sum_l (A_l r^l + B_l r^{-(l+1)}) P_l(\cos\vartheta) = A_0 + B_0 \frac{1}{r} + A_1 r \cos\vartheta + B_1 \frac{\cos\vartheta}{r^2}. \qquad (1.6)$$

Gauge freedom allows for setting $A_0 = 0$ and, since the total charge of the sphere is zero, also

$B_0 = 0$. The coefficent A_1 can be determined via the asymptotic behaviour of ϕ. Far away from the sphere the potential is unperturbed and corresponds to ϕ_0 which sets $A_1 = -E_0$. The final coefficient B_1 follows from the fact that the surface of the sphere ($r = R$) is an equipotential region. This means that the ϑ dependence has to cancel out and, hence, $B_1 = E_0 R^3$. The final expression for the electric potential is now given as

$$\phi = -E_0 r \left(1 - \frac{R^3}{r^3}\right) \cos\vartheta. \tag{1.7}$$

It can be seen that the contribution of the sphere corresponds to a dipole[1] which reflects the separation of charges in the conductor.

The electrostatic force acting onto the (hemi)sphere can be obtained by integration of $\mathrm{d}\mathbf{F}_{\mathrm{es}} = \sigma_{\mathrm{c}}(\mathbf{E}\cdot\hat{\mathbf{n}})\hat{\mathbf{n}}\,\mathrm{d}A = \sigma_{\mathrm{c}}^2\,\hat{\mathbf{n}}\,\mathrm{d}A/2\varepsilon_0$ and, thus, depends on the induced surface charge density σ_{c}. The surface charge density can be obtained via the interface condition of the electric displacement field $\mathbf{D} = \varepsilon_0\mathbf{E}$ which reads $(\mathbf{D}_{\mathrm{out}} - \mathbf{D}_{\mathrm{in}})\cdot\hat{\mathbf{n}} = \sigma_{\mathrm{s}}$. Here, $\hat{\mathbf{n}} = \mathbf{e}_{\mathrm{r}}$ denotes the unit normal vector of the sphere's surface which corresponds to the radial unit vector. Thus, σ_{s} is determined by the difference between the normal components of $\mathbf{D}$ inside and outside the sphere. Inside the sphere, $\mathbf{D} = \mathbf{E} = 0$, outside the sphere the radial component of $\mathbf{D}$ is given by

$$D_{\mathrm{r}} = -\varepsilon_0 \partial_{\mathrm{r}}\phi = E_0 \cos\vartheta \left(1 + 2\frac{R^3}{r^3}\right), \tag{1.8}$$

which, infinitesimally close to the surface, becomes $D_{\mathrm{r}} = 3\varepsilon_0 E_0 \cos\vartheta$. Therefore, the charge density evaluates to $\sigma_s = 3\varepsilon_0 E_0 \cos\vartheta$ which means that the surface charge depends linearly on the z-coordinate. Integration over the whole sphere yields a total charge of zero, integration over the upper half-sphere a charge of $q = 6\pi\varepsilon_0 R^2 E_0$.

The total force experienced by the upper half-sphere follows from integration of σ_s^2 over the the respective upper surface and results in

$$\mathbf{F}_{\mathrm{es}} = \frac{9}{4}\pi R^2 \varepsilon_0 E_0^2 \mathbf{e}_{\mathrm{z}} = a_{\mathrm{s}}\varepsilon_0 E_0^2 \mathbf{e}_{\mathrm{z}}. \tag{1.9}$$

The factor $a_{\mathrm{s}} = \frac{9}{4}\pi R^2$ takes into account the spherical geometry of the conductor. For arbitrary shapes, this factor has to be replaced by a tensor a_{ij}. Eq. (1.9) would then read $F_i^{\mathrm{es}} = a_{ij} E_0 D_{0,j}$ which is very similar to the fluid flow around a body [18, 19]. Fig. 1.5 compares the pattern of the electrical field of a sphere and a cube. Nevertheless, the force

---

[1] The potential of a dipole reads $(4\pi\varepsilon_0)^{-1}\mathbf{P}\cdot\mathbf{r}/r^3$, with $\mathbf{P}$ being the dipole moment. The sphere, thus, has a dipole moment of $P = 4\pi\varepsilon_0 R^3 E_0$

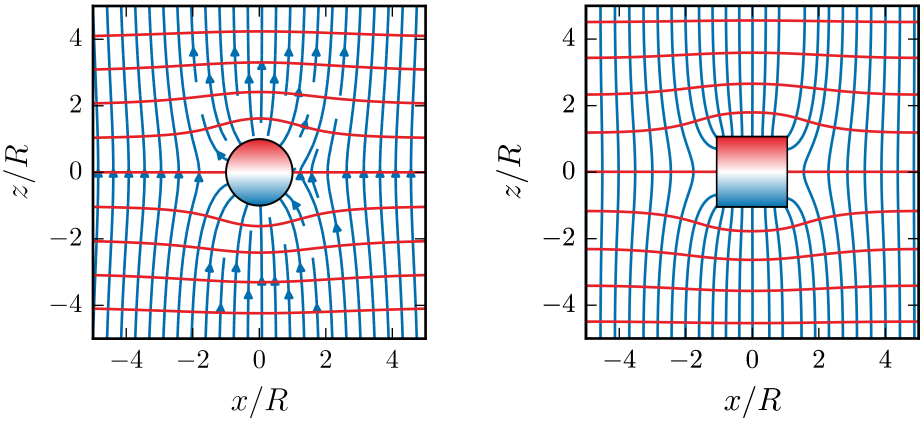

Figure 1.5.: Qualitative influence of a conducting object on an external electric field (field lines are blue, equipotential lines red). The left plot was obtained by the analytical solution for the sphere and the right one by a FEM simulation of a cube. For both cases it is evident that noteworthy perturbations of the field are only local as expected from a dipole. The colour of the bodies indicates the surface charge that changes with the z-coordinate.

experienced by the respective conducting body is proportional to the square of the external field. This implies several interesting properties. First of all, the force is independent of the sign of $\mathbf{E}_0$, which reflects the fact that if the sign of the external field changes, so does the sign of the induced surface charges. Another property can be observed for *quasistatic* fields $\mathbf{E}_0 \sin \omega t$, i.e. fields that change sufficiently slow with respect to the time scale the surface charges develop. There, the force changes with twice the frequency $F_{\mathrm{es}} \propto E_0^2 \sin^2 \omega t = E_0^2 (1 - \cos 2\omega t)/2$.

The optical transduction principle (section 1.1) can now be used to measure such an external field $\mathbf{E}_0$ based on the induction of surface charges and the corresponding force F_{es}. The idea is that the electrostatic force is exerted on the moving part of the optical shutter and the arising displacement with respect to the resting grid modulates the light flux passing through. More details on the specific MEMS layout for electric field sensing are presented in chapter 4. One of the most prominent advantages of the optomechanic transduction of the electric field is that it allows for remote sensing without massively distorting the field itself. The latter is one of the draw-backs of the very common field-mills and MEMS field mills, since they depend on a grounded electrode [20–27]. Figure 1.6 illustrates this property of the optomechanical transducer. The remote field sensing can be implemented by optical fibres such that the light source and detector as well as the readout electronics can be placed at a distance from the sensing location.

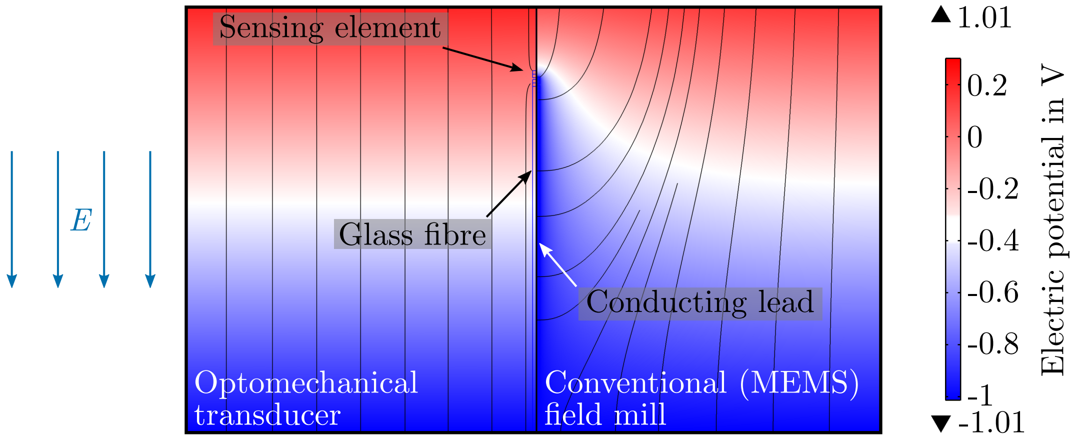

Figure 1.6.: Comparison between the conventional field mill that requires a grounded electrode (right) and the optomechanic transducer (left) that acts as a floating electrode. Due to the grounded connection, the field on the right side is massively distorted while the dielectric connection for the optomechanic transducer hardly affects the field.

Since the electrostatic force acts onto the moving mass, the mechanical response corresponds to the accelerometer/force sensor case of section 1.2 or Fig. 1.3a. The response of the transducer, however, happens at twice the frequency of the input quantity $\mathbf{E}_0$. This reduces the bandwidth for E-field sensing, since the mechanical system is compliant to the input force only for frequencies below the resonance frequency $\omega < \omega_0$ or, in this case, $\omega_{\text{E-field}} < \omega_0/2$. The frequency doubling, however, also comes along with some positive aspects. The measurement effect is fully decoupled from interfering sources which occur at the input frequency such as cross-talk. Furthermore, due to the dependency of the electrostatic force on the square of the electric field, the response of the mechanical system grows very rapidly with the strength of the field.

Another aspect of the quadratic dependence on the E_0 affects the sensitivity of the sensor. While the displacement sensitivity S of the readout is the same as in Eq. (1.1), the total sensitivity S_{es} relating the input E-field to the output voltage can be understood as an extension of the expression for S. The output voltage of the electric field sensor is given by $U_{\text{out}}(2\omega) = S\,\frac{F_{\text{es}}}{m}\,\chi(2\omega)$. Since the force $F_{\text{es}} \propto E_0^2$, the sensitivity can be defined as in

$$U_{\text{out}}(2\omega) = S\,\frac{F_{\text{es}}}{m}\,\chi(2\omega) = S_{\text{es}}\,E_0^2\,\chi(2\omega), \tag{1.10}$$

and contains everything except for the mechanics of the system. Note that S_{es} comes in units of $\mathrm{V/s^2/(V/m)^2}$. For a given device employed at frequencies $\omega < \omega_0$, another definition

$\tilde{S}_{\mathrm{es}} := S_{\mathrm{es}}/\omega_0^2$ in more plausible units of $\mathrm{V}/(\mathrm{V}/\mathrm{m})^2$ is possible, since $\chi(\omega < \omega_0) \approx \omega_0^{-2}$. This, however includes the mechanics of the device.

Chapter 2.

Optimisation of Damping and Quality Factor

The damping of the mechanical system is responsible for dissipation of its kinetic energy. Therefore, it determines the so-called quality of the system which is expressed by the quality factor Q. As discussed in subsection 1.2, this quantity is defined as the quotient of the energy stored to the energy dissipated per cycle. In the lumped parameter picture of the harmonic oscillator, it is given as $Q = \sqrt{k\,m}/d = \omega_0/2\gamma$. The damping reflects here as either the damping parameter d or the decay constant $\gamma = d/2m$.

The damping force F^{d} is proportional by d to the oscillator velocity $v = \mathrm{d}x/\mathrm{d}t$, i.e. $F^{\mathrm{d}} = d\,v$ which corresponds to the second term of Eq. (1.2). The aim of this chapter is to find a model for F^d that can be used to design devices with fine-tuned quality factors. Energy dissipation of micro- and nanomechanical systems can have a lot of different sources [4, 28] each of which can be attributed an individual quality factor Q_i. Assuming mass and stiffness do not change substantially due to the individual effects, the total quality Q is then determined as

$$\frac{1}{Q} = \sum_i \frac{1}{Q_i} = \frac{2}{\omega_0} \sum_i \gamma_i = \frac{1}{\sqrt{k\,m}} \sum_i d_i. \tag{2.1}$$

Thus, the total damping parameter and force can be composed as a sum of the individual contributions $F^{\mathrm{d}} = v \sum_i d_i = 2m\,v \sum_i \gamma_i$. Since the MEMS treated in this thesis is intended for operation in ambient air, the leading contribution is the air damping. In fact, it is so much larger than the other contributions that they can safely be neglected from here onwards. The air damping is governed by the flow induced by the moving structure and engages at its surface. Therefore, in the following sections, the basics of fluid dynamics are introduced and an analytical model for the air damping is derived.

2.1. Governing Equations of Fluid Dynamics

In the following discussion the air is treated as continuum, even though it consists of a large number of small constituents (particles, molecules, atoms) in mostly individual motion between collisions. This continuum hypothesis is, however, intact, if the particle density and the volume of interest are large enough [29]. This is expressed by the so-called Knudsen number $Kn = \lambda_\mathrm{f}/L_\mathrm{c}$, which compares the mean free path λ_f in the fluid to a characteristic length scale L_c of the underlying geometry. For $Kn < 1$, the gas can be described as continuum. The mean free path of air at ambient pressure is $\lambda_\mathrm{f} \approx 70$ nm and the characteristic length scale given by the MEMS geometries throughout this thesis $L_\mathrm{c} > 1$ µm, thus $Kn < 1$ is certainly fulfilled. For reduced pressure already in the rough vacuum regime ($\lesssim 300$ hPa) the mean free path exceeds 1 µm which leads to $Kn \gtrsim 1$. There, the molecular nature of the gas cannot be neglected anymore and statistical mechanics has to be considered.

The behaviour of fluids is, in general, described by the velocity, pressure, density and temperature fields denoted as $\mathbf{v}(\mathbf{r},t)$, $p(\mathbf{r},t)$, $\rho(\mathbf{r},t)$ and $T(\mathbf{r},t)$, respectively. These fields are governed by the conservation of mass, momentum and energy. The corresponding set of equations poses five equations for six unknowns. It can be closed by constitutive equations, equations of state and boundary or initial conditions.

The conservation of mass of a fluid during flow can be expressed by the continuity equation

$$\frac{\partial \rho}{\partial t} + \nabla \cdot (\rho \mathbf{v}) = \frac{\mathrm{D}\rho}{\mathrm{D}t} + \rho \operatorname{div} \mathbf{v} = 0, \tag{2.2}$$

with $\mathrm{D}/\mathrm{D}t = \partial/\partial t + \mathbf{v} \cdot \nabla$ being called the substantial time derivative. This operator yields the temporal change of a quantity upon following the flow. For incompressible flow, the density is constant. Eq. (2.2), thus, reduces to $\nabla \cdot \mathbf{v} = \partial_i v_i = 0$[1].

2.1.1. Navier-Stokes Equation

The widely used Navier-Stokes equation is the equation of motion and, therefore, the embodiment of the conservation of momentum of a Newtonian fluid [19, 30]. In general, the equation of motion of a fluid is given by

$$\rho \frac{\mathrm{D}v_i}{\mathrm{D}t} = \rho \frac{\partial v}{\partial t} + \rho v_j \frac{\partial v_i}{\partial x_j} = \frac{\partial \sigma_{ij}}{\partial x_j} (+f^\mathrm{b}), \tag{2.3}$$

---

[1] Note that Einstein's summation convention is used and that ∂_i denotes the i-th component of the nabla operator.

and sums up all forces acting onto the fluid. The force f^{b} can stand for, e.g., gravity ($f^{\mathrm{b}} = \rho\mathbf{g}$ with $\mathbf{g}$ being the gravitational acceleration) or other body forces which will be neglected in this thesis. The second term stemming from the substantial derivative corresponds to convection in the fluid. Due to the nonlinearity of this term, an analytical solution is only possible for highly symmetric problems or if the equation can be linearised. The term on the right hand side contains the divergence of the stress tensor $\sigma_{ij} = -p\delta_{ij} + \sigma'_{ij}$ and considers the effects of pressure (p) and friction (σ'_{ij}). Here, δ_{ij} is the Kronecker delta.

The properties of an isotropic Newtonian fluid reflect in the constitutive equation $\sigma' = \sigma'(\mathbf{v})$ which is given by $\sigma'_{ij} = \bar{\mu}(\nabla\cdot\mathbf{v})\delta_{ij} + \mu(\partial_i v_j + \partial_j v_i)$. The first term corresponds to the friction during compression of the fluid with $\bar{\mu}$ being the volume viscosity. This term vanishes for incompressible flow due to the conservation of mass. The second term corresponds to shear friction and is composed of the dynamic viscosity μ and the symmetric part of the velocity gradient $\partial_i v_j$. Inserting this expression into the momentum balance yields under the assumption of constant material values the Navier-Stokes equation

$$\frac{\mathrm{D}v_i}{\mathrm{D}t} = \frac{1}{\rho}\partial_i\left[-p + (\bar{\mu} + \mu)\partial_j v_j\right] + \nu\Delta v_i, \tag{2.4}$$

where $\Delta = \partial_j\partial_j$ denotes the Laplace operator and $\nu = \mu/\rho$ the kinematic viscosity. For incompressible flow, the continuity equation eliminates the dilational stress via $\partial_j v_j = 0$ and the equation reduces to

$$\frac{\mathrm{D}v_i}{\mathrm{D}t} = -\frac{1}{\rho}\frac{\partial p}{\partial x_i} + \nu\Delta v_i. \tag{2.5}$$

2.1.2. Reynolds Equation for Squeeze Films

Another important equation is Reynold's lubrication equation with which the flow in fluid films inside narrow gaps can be described [19,30,31]. It is commonly used for lubrication applications as in bearings or to calculate squeezing of a fluid. It follows from the Navier-Stokes Eq. (2.4) and the conservation of mass under certain assumptions. A schematic of such a fluid film is depicted in Fig. 2.1. The first assumption imposes that the film thickness $h(x, y, t)$ is much smaller than the lateral dimensions L in x- or y-direction, i.e. $\varepsilon := h/L \ll 1$. Another assumption is that the pressure is approximately constant across the film, $p = p(x, y, t)$. Furthermore, the fluid is considered an ideal gas under isothermal conditions, which means that the equation of state is given as $p \propto \rho$.

Analysing the scaling behaviour of the Navier-Stokes Eq. (2.4) under the assumption that ε is small, one finds that the inertial and convective terms as well as the dilational

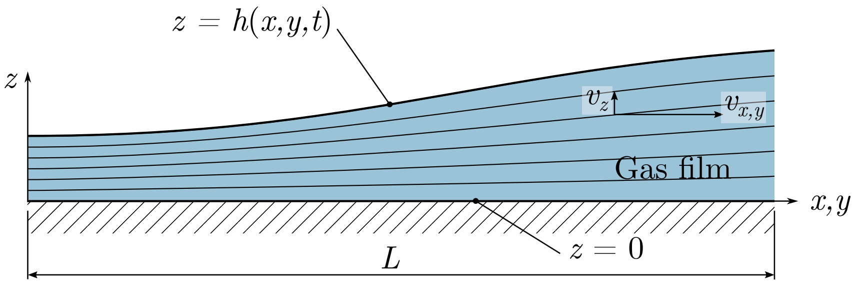

Figure 2.1.: Illustration of a thin film flow. The gas is trapped inside the narrow gap with height $h \ll L$ much smaller than the lateral length scale of the geometry. The gas velocity $\mathbf{v}$ points mainly into the lateral direction. The solid walls, here at $z = 0$ and $z = h(x, y, t)$, can in principle have arbitrary shapes.

term are negligible compared to the viscous shear stress. This is the usual situation in thin fluid films. A rigorous perturbation analysis regarding ε motivating this, in which all terms of the order $\mathcal{O}(\varepsilon^2)$ or higher are discarded, can be found in [31]. Omitting these terms, Eq. (2.4) reduces to $\nabla p = \mu\Delta\mathbf{v}$ which is called Stokes equation. Considering the Laplacian, one notices that the derivative with respect to z $\partial_z^2 \to h^{-2}$ scales larger than the lateral derivatives $\partial_{x,y}^2 \to L^{-2}$. This means that $\Delta \approx \partial_z^2$ and the Stokes equation can be written componentwise as

$$\partial_{x,y} p = \mu \partial_z^2 v_{x,y} \quad \text{and} \quad \partial_z p = 0. \tag{2.6}$$

This means that the gas only escapes in the lateral directions and that $v_i = v_i(z,t)$ is a function of time and z only. Thus, the velocity can be obtained directly by integration which leads to

$$v_{x,y} = \frac{\partial_{x,y} p}{\mu} \left(\frac{1}{2} z^2 + A_{x,y} z + B_{x,y} \right). \tag{2.7}$$

The integration constants $A_{x,y}$ and $B_{x,y}$ follow from the no-slip boundary conditions at $z = 0$ and $z = h$. There, the gas velocity $\mathbf{v}$ equals the velocity imposed by the solid boundary surfaces $\mathbf{v} = \mathbf{U} = (U_0, V_0, W_0)$. The bottom wall at $z = 0$ shall be at rest which corresponds to $\mathbf{v}|_{z=0} = 0$. If, as in the present case, one is concerned about squeezing only, the top wall defined by $z = h$ shall move in z-direction only. Hence, $\mathbf{v}|_{z=h} = (0, 0, W_0)$. Note that the wall at $z = 0$ is assumed a flat surface, while the shape of the opposing wall is given by $z = h(x, y, t)$. These boundary conditions lead to purely Poiseuille-like flow $v_{x,y} = \frac{\partial_{x,y} p}{2\mu}(z^2 - hz)$. Lateral velocity components of the top wall would effect Couette-type flow which is characterised by being proportional to the quotient z/h (see Eq. (2.13)).

To ensure the conservation of mass, the continuity equation has to be considered. For the presumed isothermal, ideal gas, Eq. (2.2) can be expressed in terms of the pressure as

$\partial_t p + \partial_i(pv_i) = 0$. Integration across the film and applying the integration rule of Leibniz to the divergence term leads to

$$h\frac{\partial p}{\partial t} + \partial_{x,y}\int_0^h (pv_{x,y})\mathrm{d}z + pW_0 = 0. \tag{2.8}$$

After inserting here the velocity Eq. (2.7), the integral can be performed. Using the kinematic boundary condition at the upper integration limit $\frac{\mathrm{D}}{\mathrm{D}t}(z - h(x,y,t)) = 0$, one can express W_0 in terms of h as $W_0 = \partial_t h$. This leads ultimately to the Reynolds equation for squeeze films

$$\frac{\partial hp}{\partial t} = \nabla\cdot\left(\frac{h^3}{12\mu}p\nabla p\right), \tag{2.9}$$

which is as the Navier-Stokes Eq. (2.4) nonlinear.

2.2. Modelling the Air Damping

In this section, a model of the air damping of the MEMS sensor is derived based on the governing equations introduced above. The work on this model has been published in the references [32–37] which will be compiled in this section. Due to the high influence of the air damping in micro- and nanomechanical resonators, a lot of work has been invested to this matter already from the early stage of MEMS. Some highlighted references this work is based on, are [38–43] for the viscous damping in subsection 2.2.1 and [44–48] for squeeze film damping in subsection 2.2.2.

First of all, the fluid mechanics problem needs to be defined and building on that necessary assumptions are made. The resulting model will then be tested against finite volume method (FVM) simulations and measurements of several different test structures. The results were used to design devices that exhibit very low quality factors of $Q \gtrsim 1$ which is favorable for vibration sensing as briefly discussed in subsection 1.2.

Bearing in mind the behaviour of the Q-factor with respect to different dissipation sources as in Eq. (2.1), a reasonable approach for the model of the air damping is to divide the total force into manageable contributions. This means for the total damping force F that it corresponds to the sum of these contributions, $F = \sum_i F_i$. The basic geometry of the MEMS is partly depicted in Fig. 1.1. Not shown is the glass part which is bonded on top of the silicon structure and takes significant influence on the damping. Therefore, a schematic of the cross-section of the MEMS chip is shown in Fig. 2.2, which also highlights the damping contributions to be expected.

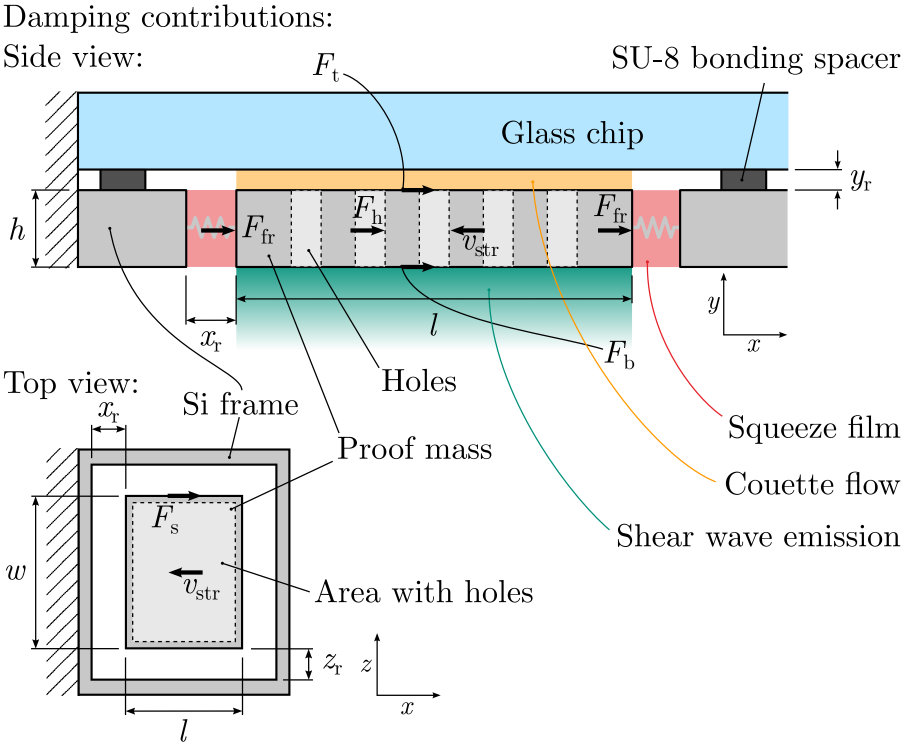

Figure 2.2.: Cross-sectional view of the schematic depicted in Fig. 1.1. The oscillation of the proof mass is damped by the air via the forces F_i acting onto the respective faces off the mass. The damping forces are proportional to the velocity of the proof mass $F_i = -d_i v_{\mathrm{str}}$. The total damping corresponds to the sum $\sum_i F_i$ with the (by far) leading contributions due to squeeze film damping, Couette flow and shear wave emission.

The figure shows the individual damping forces F_i pointed in the opposite direction of the momentary velocity v_{str} of the proof mass. Since these forces are surface forces, they are indicated at the respective faces they are exerted on. The leading contributions, as will be shown in this section, are the ones acting onto the top face F_{t}, the bottom face F_{b} and the two front faces F_{fr}. The damping due to the side faces lying in the x, y-plane in Fig. 2.2, F_{s}, shows no perceptible contribution. Furthermore, the effect of the holes which concerns the effective mass m as well as the damping d will be discussed.

2.2.1. Viscous Shear Damping

First, the viscous forces exerted onto the top and bottom faces (x, z-plane) of the proof mass are discussed. Due to the relatively large corresponding area $A_{\mathrm{m}} = wl$, these forces are expected to be large. Since the physics of these two contributions is very similar, they can be modelled at the same time as the flow between two infinite parallel plates of which one is oscillating with velocity $\mathbf{U} = v_{\mathrm{str}} e^{\mathrm{i}\omega t} \mathbf{e}_{\mathrm{x}}$. The moving plane is placed at $y = 0$, while the other, resting plane is located at $y = y_{\mathrm{r}}$. Since the velocities v involed are sufficiently small compared to the speed of sound $c_0 \gg v$, the Mach number $M = v/c_0 \ll 1$ is far smaller than one[2]. This, in turn, means that the flow can be treated as incompressible. Hence, the conservation of mass Eq. (2.2) reduces to $\nabla \cdot \mathbf{v} = 0$ and with that, the Navier-Stokes equation (2.5) can be used as starting point.

Following from the symmetry of this configuration, the velocity of the air $\mathbf{v}$ can have only one nonzero component which is the x-component. Furthermore, it can only depend on the coordinate y of the gap between the plates. Thus, with $\mathbf{v} = v_{\mathrm{x}}(y, t)\mathbf{e}_{\mathrm{x}}$, Eq. (2.5) reduces to

$$\partial_t v_{\mathrm{x}}(y, t) = \frac{\mu}{\rho} \partial_y^2 v_{\mathrm{x}}(y, t). \tag{2.10}$$

The velocity follows from this straightforwardly via separation of variables and employing an exponential ansatz. Applying the no-slip boundary condition of $v_{\mathrm{x}}(0, t) = v_{\mathrm{str}} \mathrm{e}^{\mathrm{i}\omega t}$ at the oscillating plate and $v_{\mathrm{x}}(y_{\mathrm{r}}, t) = 0$ at the opposite plate, the air velocity inside the gap can be written

$$v_{\mathrm{x}} = v_{\mathrm{str}} \frac{\sinh \kappa (y_{\mathrm{r}} - y)}{\sinh \kappa y_{\mathrm{r}}} \mathrm{e}^{\mathrm{i}\omega t}, \tag{2.11}$$

with the inverse length $\kappa = (1 + \mathrm{i})\sqrt{\omega\rho/2\mu}$. This parallel flow solution corresponds to the emission of shear waves into the air. These waves decay very rapidly and usually do not reach far into the medium. A measure thereof is the factor $(1 + \mathrm{i})/\kappa = \sqrt{2\mu/\omega\rho} =: \delta$ which is called penetration depth. Note that δ depends on the frequency and the higher ω, the smaller is δ. Obviously, these shear waves are not able to fully develop if the spacing of the gap y_{r} is of the same order of magnitude as δ or smaller, while for $y_{\mathrm{r}} \gg \delta$ they are undisturbed by the resting wall. This is depicted in Fig. 2.3. Furthermore, for $v_{\mathrm{r}} \lesssim \delta$, the velocity profile is linear. This behaviour corresponds to Couette-type flow. In the present case, i.e. air at ambient conditions and a frequency of $f = \omega/2\pi \approx 1$ kHz, the penetration depth is approximately $\delta \approx 68$ µm, which means that the Couette behaviour is valid for a large range of gap widths.

The force damping the oscillating plate can now be calculated via evaluating the shear-stress $\sigma_{ij}(y = 0, t)$ directly at the plate. Since only the xy-component of this tensor

---

[2] Typical velocities of the plate are of the order $v_{\mathrm{str}} \lesssim 1\mathrm{mm/s}$. With the speed of sound in air at ambient pressure and 20°C of $c_0 \approx 340$ m/s, the Mach number $M \lesssim 3 \cdot 10^{-6}$ is sufficiently small to assume incompressibility.

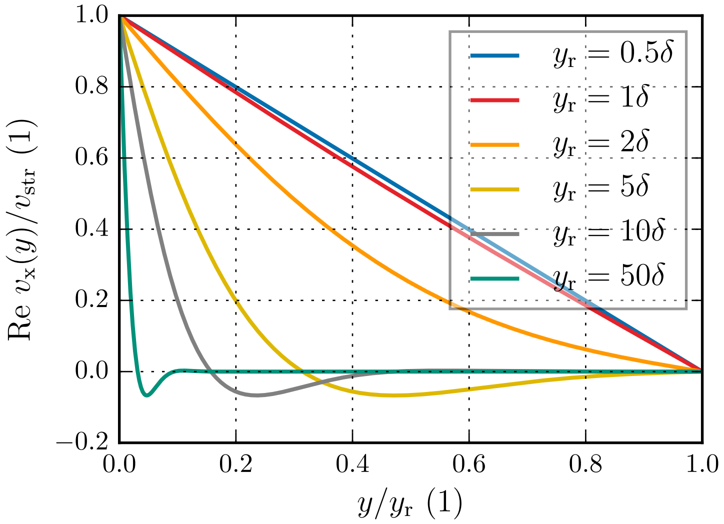

Figure 2.3.: Velocity profile between one oscillating and one still parallel plate given by Eq. (2.11). The form of the profile depends on the relation between gap width and penetration depth y_r/δ.

corresponds to damping, the other components shall be neglected. Furthermore, only the spatial part will be considered, as the temporal part works only as a phase factor with respect to time. Thus, the shear stress is given as

$$\sigma_\mathrm{xy}(y=0) = -(1+\mathrm{i})\frac{\mu}{\delta}v_\mathrm{str}\coth\left[(1+\mathrm{i})\frac{y_\mathrm{r}}{\delta}\right]. \tag{2.12}$$

Multiplying this expression by the top/bottom area of the proof mass A_m, yields a force which is still complex valued. Only the real part of this force corresponds to the damping force.

Looking again at Fig. 2.2, the orange region confined between proof mass and glass is very narrow, typically in the range of $5\ \mu\mathrm{m} < y_\mathrm{r} < 15\ \mu\mathrm{m}$ which is much smaller than δ. The damping in this region is, therefore, dominated by Couette flow and the hyperbolic cotangent can be sufficiently accurately approximated by its lowest order term of its series expansion around $y_\mathrm{r} = 0$[3]. Thus, the force in this region increases for decreasing gap width as $1/y_\mathrm{r}$ and reads

$$F_\mathrm{t} = A_\mathrm{m}\sigma_\mathrm{xy}(y=0)|_{y_\mathrm{r}\ll\delta} \approx -A_\mathrm{m}\mu\frac{v_\mathrm{str}}{y_\mathrm{r}}. \tag{2.13}$$

---

[3] Note that the hyperbolic cotangent features a singularity at $y_\mathrm{r} = 0$. Therefore, the Laurent series expansion has to be employed which reads $\coth(z) = z^{-1} + \frac{1}{3}z - \frac{1}{45}z^3 + \ldots$.

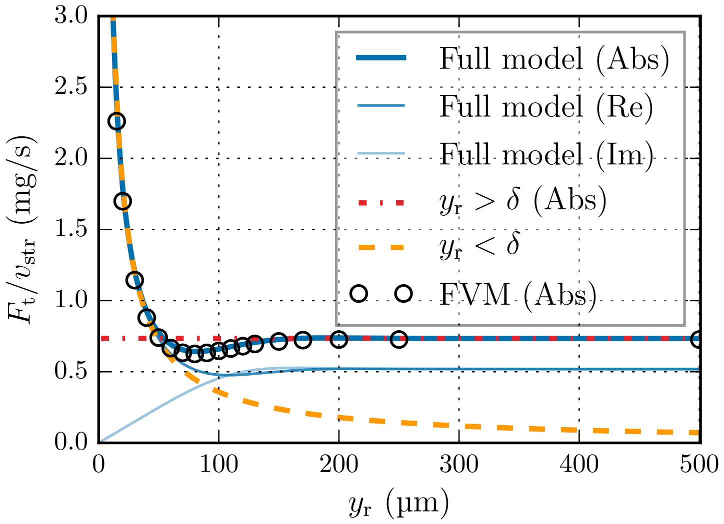

Figure 2.4.: Damping force F_t/v_{str} divided by the plate velocity for a plate with area $A_m = 1 \times 2\ \text{mm}^2$ for varying gap width y_r. The plot compares the full model Eq. (2.12) and the asymptotics in terms of the absloute value to the FVM simulations. The damping parameter corresponds to the real value (Re).

On the opposite side of the proof mass coloured green in Fig. 2.2, the gap width is very large compared to the penetration depth $y_r \gg \delta$. Therefore, the asymptotic value for the hyperbolic cotangent for $y_r \to \infty$ can be employed, i.e. $\coth(y_r)|_{y_r\to\infty} \to 1$. The corresponding damping force on the bottom side is therefore given by

$$F_b = A_m \mathrm{Re}\, \sigma_{xy}(y=0)|_{y_r\to\infty} = -A_m \sqrt{\frac{\mu\rho\omega}{2}}\, v_{str}. \tag{2.14}$$

To give an idea how large this viscous shear damping can be expected to be for different values of y_r, one can, e.g., assume a plate with a width of $w = 2$ mm and a length of $l = 1$ mm that oscillates at $f = 1000$ Hz. The corresponding damping force with regard to the plate velocity F_t/v_{str} obtained via the model Eq. (2.12) in dependency of y_r is depicted in Fig. 2.4. Furthermore, the two approximations Eqs. (2.13) and (2.14) are shown. The comparison to FVM simulations suggests the validity of the model.

2.2.2. Squeeze Film Damping

In contrast to the viscous shear damping at the top and bottom side, the damping at the front sides is controlled by an out-of-plane oscillation, which is due to the orientation of the corresponding faces of the moving mass. This movement periodically compresses and expands the air inside both volumes marked red in Fig. 2.2. Since these two regions are equivalent, only one will be treated in this subsection. The corresponding three dimensional volume be called V_0. Due to the out-of-plane movement, the problem is more complex than in the previous section. Starting point for deriving an expression for the squeeze film damping force is the Reynolds lubrication equation (2.9) which will be solved for the present problem based on the very general Green's function approach of [46, 49].

Eq. (2.9) is quadratic with respect to the pressure. Thus, the first step is to linearise it. This is achieved by exploiting the fact that, first, the oscillation amplitude δg is small compared to the gap width x_r and, second, that the pressure variation is also small compared to the ambient pressure P_0. Inserting for $p = P_0 + \delta p$ and for $h = x_\mathrm{r} + \delta g$, and omitting terms of order $\mathcal{O}(\delta p^2)$ and $\mathcal{O}(\delta p \delta g)$ one arrives at a linearised equation. In terms of the normalised quantities $P = \delta p / P_0$ and $g = \delta g / x_\mathrm{r}$ it reads

$$(\Delta - \alpha^2 \partial_t) P = \alpha^2 \partial_t g, \tag{2.15}$$

where $\alpha^2 = 12\mu / x_\mathrm{r}^2 P_0$. This equation can now be solved with the help of Green's functions.

The Green's function $G(\mathbf{r}, t | \mathbf{r}', t')$ corresponds to the response at point $\mathbf{r}$ and time t of the given system to an excitation at $\mathbf{r}'$ and t'. It is defined for a point source and the differential operator in Eq. (2.15) as

$$(\Delta - \alpha^2 \partial_t) G(\mathbf{r}, t | \mathbf{r}', t') = -4\pi \delta(\mathbf{r} - \mathbf{r}') \delta(t - t'). \tag{2.16}$$

In the present case, however, the source $\alpha^2 \partial_t g =: -4\pi\tilde{\rho}$ is distributed. It is given by the oscillation with amplitude X_0 of the plate and can, thus, be written as $4\pi\tilde{\rho} = -\mathrm{i}\alpha^2 X_0 \omega \mathrm{e}^{\mathrm{i}\omega t}$. The Green's function, therefore, links the compression/expansion at all points $\mathbf{r}' \in V_0$ and times t' to the pressure at the observation point $(\mathbf{r}, t)$. The solution for P in this inhomogeneous equation can be expressed by means of the Green's function as

$$P(\mathbf{r}, t) = \int_{V_0, t} G(\mathbf{r}', t' | \mathbf{r}, t) \tilde{\rho}(\mathbf{r}', t') \mathrm{d}\mathbf{r}' \mathrm{d}t'. \tag{2.17}$$

Hence, if the Green's function is known, the pressure can be calculated.

In order to find an expression for G, one can start by separation $G = u(\mathbf{r}|\mathbf{r}') T(t|t')$. This leads to $\Delta u / u = -k^2 = \alpha^2 \partial_t T / T$ with k acting as a constant for now. The temporal part follows directly from integration and reads $T = \frac{4\pi}{\alpha^2} \exp[-\frac{k^2}{\alpha^2}(t - t')] \Theta(t - t')$. The Heaviside

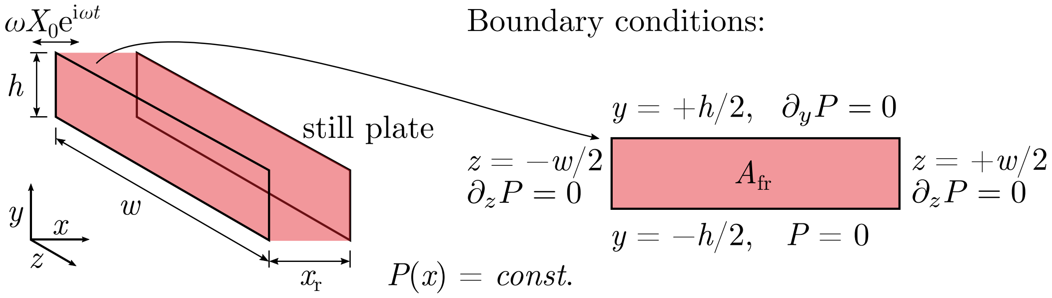

Figure 2.5.: Volume V_0 compressed/expanded by the oscillation of the inertial mass (red areas in Fig. 2.2). Since the pressure is assumed constant in the direction of compression, the boundary conditions are enforced on the edges of the two-dimensional region depicted on the right.

function $\Theta(t-t')$ ensures that the answer of the system happens after the excitation. The spatial part now reads $\Delta u + k^2 u = 0$ which is an eigenvalue equation. One can now take into account the fact that the pressure can be assumed constant along the direction of compression which was already required in subsection 2.1.2. The dimensionality thus reduces and the spatial part of the Green's function can be put together from the eigenfunctions u_{mn} of the two-dimensional Helmholtz equation $\Delta u_{mn} + k_{mn}^2 u_{mn} = 0$.

These eigenfunctions are both orthonormal, i.e.

$$\int_{V_0} u_{mn}^*(\mathbf{r}) u_{kl}(\mathbf{r}) \mathrm{d}\mathbf{r} = \delta_{mk}\delta_{nl}, \tag{2.18}$$

and complete

$$\sum_{mn} u_{mn}^*(\mathbf{r}') u_{mn}(\mathbf{r}) = \delta(\mathbf{r} - \mathbf{r}'). \tag{2.19}$$

The Green's function can now be composed as an expansion in these eigenfunctions and reads including the temporal part

$$G(\mathbf{r}, t|\mathbf{r}', t') = \frac{4\pi}{\alpha^2} \sum_{mn} \mathrm{e}^{-k_{mn}^2 (t-t')/\alpha^2} u_{mn}^*(\mathbf{r}') u_{mn}(\mathbf{r}) \Theta(t-t'). \tag{2.20}$$

The specific form of these eigenfunctions u_{mn} depends on the boundary conditions. Since the pressure is assumed constant across the compressed gap, the volume V_0 of interest reduces to an area $A_{\mathrm{fr}} = h\,w$ corresponding to the front face of the proof mass. The point of origin be located at the centre of this face, i.e. $y \in [-h/2, +h/2]$ and $z \in [-w/2, +w/2]$. The boundary conditions are enforced at its edges. The *standard* boundary condition which corresponds to an ideally open edge is $P = 0$. It is, e.g., employed in Blech's solution of the Reynolds equation [44] which is the base for most works on squeeze film damping in MEMS. Applying these boundary conditions on all edges for the present microstructure, however yields wrong results for the damping force. In fact, there is only one edge that can be described as ideally open, the bottom edge $y = -h/2$. The other three edges are essentially closed. The air is not able to escape well through these boundaries. At the top, i.e. $y = +h/2$, the glass chip and the narrow gap with diameter y_r impedes the air flow. Since $h \ll w$, the air is more likely to escape through the bottom edge than through the edges at $z = \pm w/2$. Therefore, one can assume these edges to be closed as well. The corresponding boundary condition is the vanishing derivative of the pressure, i.e. $\partial_y P = 0$ at $y = +h/2$ and $\partial_z P = 0$ at $z = \pm w/2$. See Fig. 2.5 for an overview of where which boundary condition is applied.

The eigenfunctions and -values for this configuration read

$$u_{mn} = \frac{2}{\sqrt{w\,h}} \cos\left[\frac{m\pi}{2h}\left(y + \frac{h}{2}\right)\right] \cdot \begin{cases} \cos\frac{n\pi z}{w} & n\,\text{even} \\ \sin\frac{n\pi z}{w} & n\,\text{odd} \end{cases} \quad \text{and} \tag{2.21}$$

$$k_{mn}^2 = k_m^2 + k_n^2 = \left(\frac{m\pi}{2h}\right)^2 + \left(\frac{n\pi}{w}\right)^2, \tag{2.22}$$

respectively. The index m can only take on odd values. An expression for the pressure can now be obtained by inserting Eq. (2.20) and these eigenfunctions into Eq. (2.17). While performing the integration over $\mathbf{r}'$, one finds that the only possible value for n is $n = 0$ which corresponds to a constant pressure distribution along the z direction. Thus, one obtains

$$P = -\sum_{m,\text{odd}} \frac{4}{m\pi}(-1)^{(m-1)/2} \frac{X_0 \mathrm{i}\omega \mathrm{e}^{\mathrm{i}\omega t}}{x_\mathrm{r}\left(\frac{k_m^2}{\alpha^2} + \mathrm{i}\omega\right)} \cos\left[\frac{m\pi}{2h}\left(y + \frac{h}{2}\right)\right] \tag{2.23}$$

for the pressure. The force f_fr due to this pressure acting on the front face of the oscillating mass follows now by integration over the face area. Introducing the squeeze-number $\sigma = \alpha^2\omega h^2 = 12\mu\omega h^2/x_\mathrm{r}^2 P_0$, it reads

$$f_\mathrm{fr} = -P_0 A_\mathrm{fr} \frac{32}{\pi^4}\frac{X_0}{x_\mathrm{r}}\sigma \sum_{m,\text{odd}} \frac{1}{m^2}\frac{1}{m^2 + \mathrm{i}\frac{4}{\pi^2}\sigma} = -P_0 A_\mathrm{fr}\frac{X_0}{x_\mathrm{r}}\left[\mathrm{i} + \frac{\mathrm{i}-1}{\sqrt{2\sigma}}\tan\left(\frac{\mathrm{i}-1}{\sqrt{2}}\sqrt{\sigma}\right)\right]. \tag{2.24}$$

The damping force F_fr is again given by the real part of this complex expression and is thus given by

$$F_\mathrm{fr} = -P_0 A_\mathrm{fr}\frac{X_0}{x_\mathrm{r}}\frac{1}{\sqrt{2\sigma}}\mathrm{Re}\left[(\mathrm{i}-1)\tan\left(\frac{\mathrm{i}-1}{\sqrt{2}}\sqrt{\sigma}\right)\right]. \tag{2.25}$$

The total damping force follows now as the sum of Eqs. (2.13), (2.14) and (2.25). It depends, apart from the dimensions of the proof mass, on the spacings x_r and y_r of the in-plane gap and the out-of-plane gap, respectively, and reads

$$F_\mathrm{tot} = -A_\mathrm{m} v_\mathrm{str} \left(\frac{\mu}{y_\mathrm{r}} + \sqrt{\frac{\mu\rho\omega}{2}} \right) - P_0 A_\mathrm{fr} \frac{X_0}{x_\mathrm{r}\sqrt{2\sigma}} \mathrm{Re}\left[(\mathrm{i}-1) \tan\left(\frac{\mathrm{i}-1}{\sqrt{2}} \sqrt{\sigma} \right) \right]. \tag{2.26}$$

This dependency on the geometry can – to a certain point – be used to design MEMS devices with specific quality factor.

2.2.3. Numerical Model

Since the individual components of the analytical model are based on ideal geometries such as infinitely large plates, second order effects are not considered. These include finite size and edge effects as well as mutual interactions between the components. Even though these effects are small, the reliability of the model is affected by them. A possible way to take into account these effects that are often challenging to model analytically are numerical methods. There exist several methods to solve partial differential equations for a given geometry. Some of the most commonly used are, e.g., the finite element method (FEM), the finite difference method (FDM) or the finite volume method (FVM). While the FEM is the default choice for most physical problems such as structural mechanics or electrostatics, a natural choice for computational fluid mechanics is the FVM. One of the advantages of the FVM is that the laws of conservation are intrinsically fulfilled. The fluid dynamics computations within the scope of this thesis were performed with the open source software OpenFOAM. The solver that was employed relies on the FVM. The numerical results presented in this section were published in the references [32–34, 36, 37].

The geometry for the simulations conicides with the cross-section used as basis for the analytical model (Fig. 2.2). A two-dimensional domain was chosen to save computational cost and time. Note that, since only fluid dynamic computations were performed, only the air and not the Si structure comprises the geometry. The velocity imposed by the oscillating plate is given by the no-slip boundary conditions $\mathbf{v} = v_\mathrm{str} \sin \omega t\, \mathbf{e}_\mathrm{x}$ set at the corresponding edges. At all other edges the velocity is set zero $\mathbf{v} = 0$. The boundary corresponding to the resting plate of the model for F_b was placed far enough from the moving plate at a distance of 2 mm which corresponds to roughly thirty times the penetration depth.

The meshing was performed using rectangular meshes. This seems to be an obvious choice due to the also rectangular geometry. The mesh was condensed towards the moving

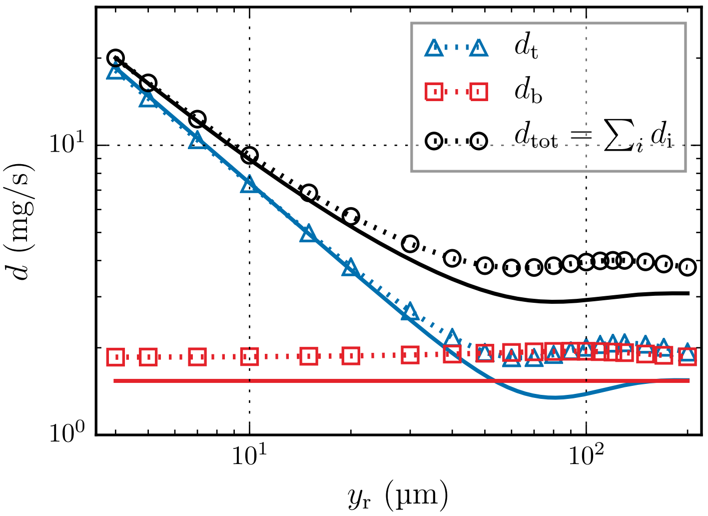

Figure 2.6.: Comparison of the damping parameter d obtained with FVM simulations (markers, dotted lines) and with the analytical model (solid lines) for a sweep of y_r.

plate in order to increase the accuracy of the computations with reasonable effort. Due to the small given velocities, the corresponding displacements of the plate are smaller than the minimum mesh element size. Therefore, no moving mesh has to be considered. The simulations were performed in time domain with a duration of ten oscillation periods. The forces acting on the plate boundary were calculated on the fly without involving any post processing.

In order to compare the individual contributions of the analytical model with results of the FVM, the forces had to be calculated for each of the respective faces individually rather than for the whole plate at once. The viscous shear contributions were subject to a parameter sweep of the silicon glass gap width y_r ranging from 4 µm to 200 µm. The distance at the bottom side was not varied. The in-plane gap width x_r was set to a large value of 1000 µm and also not varied. The results of this parameter sweep is depicted in Fig. 2.6 in terms of the damping parameter $d = F/v_{str}$. Even though the front faces were also part of the simulations, only the shear forces on the top and bottom were considered and compared to the analytical model.

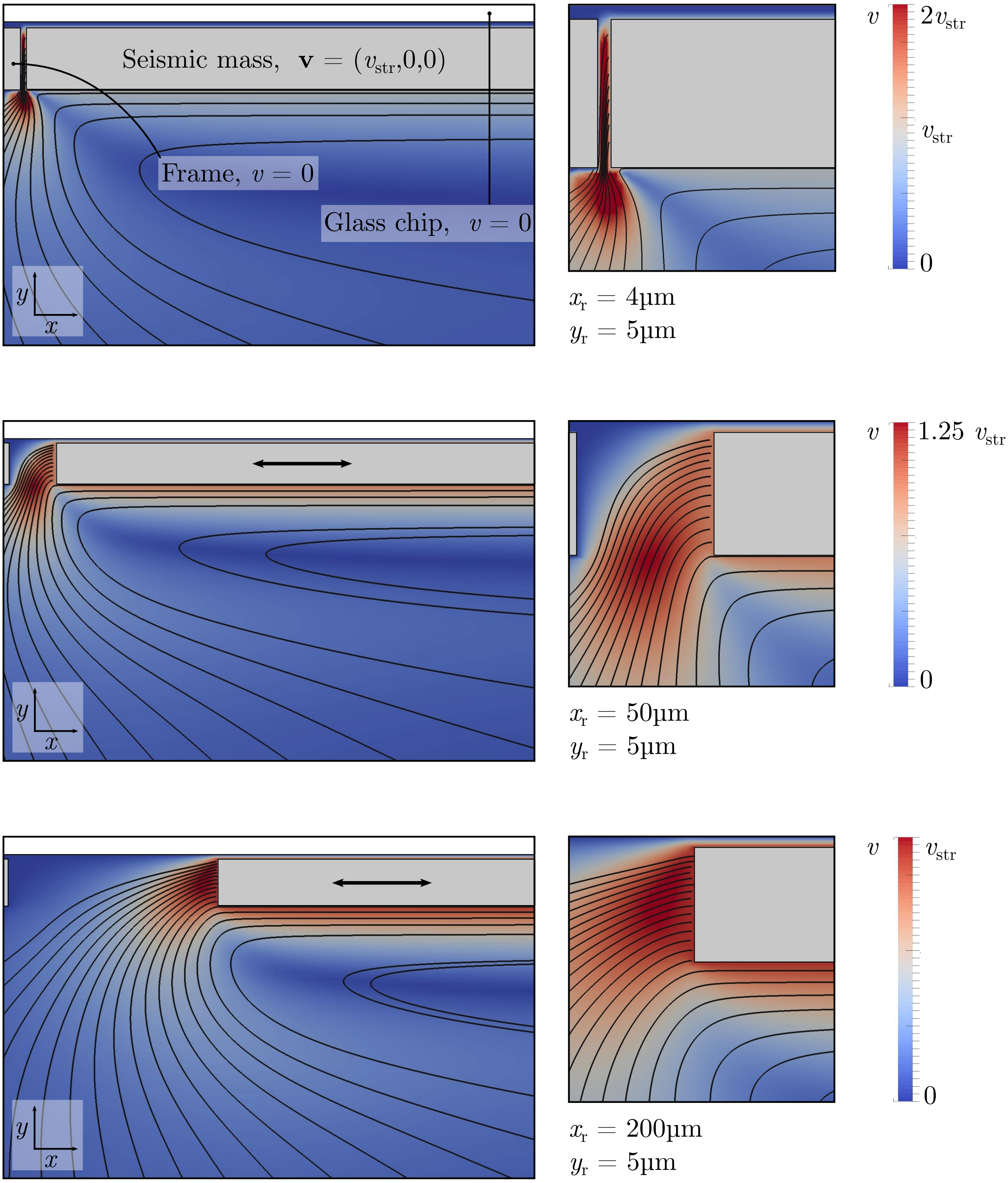

Figure 2.7.: Magnitude of the velocity field $|\mathbf{v}|$ and streamlines obtained from FVM simulations at a time step of maximum velocity. The zooms on the side show the in-plane gap in more detail. The velocity of the air escaping the gap can be much higher than the plate velocity. For $x_{\mathrm{r}} = 4\ \mu\mathrm{m}$, $v_{\max} \approx 10 v_{\mathrm{str}}$ while being coloured the same way as $2v_{\mathrm{str}}$ due to better visibility of other regions [34].

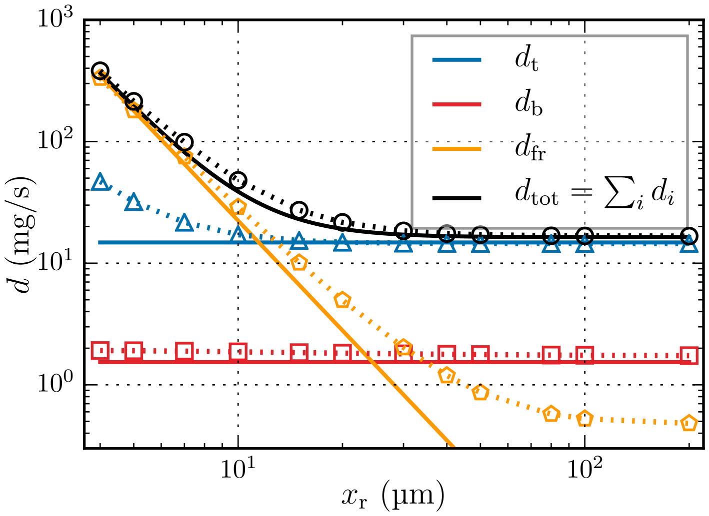

Figure 2.8.: Comparison of the damping parameter d obtained with FVM simulations for a sweep of y_r (markers, dotted lines) with the analytical model (solid lines).

Obviously, the model works very well for small values of $y_\mathrm{r} \lesssim 20$ µm, which is at the same time a reasonable upper limit for the height of the SU8 spacer between glass and silicon chip[4]. For larger y_r and also for the bottom side, the FVM differs from the analytic model. A reasonable explanation for this is that an additional flow is generated from one front face to the other which is not considered by the analytical model. Since at the bottom the fluidic resistance is low, this flow passes the plate mostly at the bottom. This increases the velocity gradient and in turn the stress applied on the plate. The widening y_r opens the channel at the top side, thus increasing the stress there as well. This is indicated by the streamlines in Fig. 2.7. Nevertheless, the analytical model is sufficiently accurate for the intended gap widths of $y_\mathrm{r} < 20$ µm.

To investigate the squeeze film damping under more realistic conditions, a parameter sweep for the in-plane gap width x_r was set up with $y_\mathrm{r} = 5$ µm held constant. This rather small value for y_r was chosen since it reflects the actual gap width of the MEMS and ensures that the air escapes only through the lower end. The sweep values were ranging from $x_\mathrm{r} = 4$ µm to 200 µm.

The velocity fields obtained by the numeric simulation for $x_\mathrm{r} = 4$, 50 and 200 µm is shown in Fig. 2.7. These three examples represent cases where the aspect ratio of the in-plane gap is small, intermediate and large, respectively. For small aspect ratios x_r/h, the assumption

---

[4] From a technological point of view, the height of the SU8 spacer can even exceed 100 µm.

of a narrow gap which was required in the derivation of the Reynold's equation (subsection 2.1.2) is definitely valid, whereas for large aspect ratios it is not. Here, the corresponding analytical model yields incorrect results. This can be seen in Fig. 2.8 where the results of the individual components of the model Eq. (2.26) are compared to the FVM.

The numerics reveal that for values of x_r higher than ~ 20 µm which corresponds to an aspect ratio of ~ 0.5 the numeric model for d_fr diverges from the analytical one until it reaches a steady value for $x_\mathrm{r} \gtrsim 100$ µm. For small values, however, the model works expectedly well. This is at the same time the regime where the squeeze film damping dominates. For larger in-plane gaps the damping is dominated by the viscous shear forces. The contribution from the front faces degenerates there to a second order effect which can be neglected. Furthermore, it can be observed that there is a coupling between the squeezing and the viscous shear force at the top side of the plate that gets stronger for decreasing values of x_r. As for the y_r sweep, the individual flows influence each other in a non-trivial way.

Nevertheless, it has been shown that for the discussed dimensions of the proof mass the total damping parameter can be varied by a factor of ~ 10 for each of the gap widths x_r and y_r. This can be used to design a specific quality factor by adjusting the geometrical dimensions of the oscillator. The results from both analytical and numerical modelling were tested by measuring several series of test structures. These include also second order contributions such as the influence of holes or the effects of the other in-plane gap z_r which are not considered in the models.

2.3. Measurements

To ensure that the analytical model and also the numerical simulations are truly able to describe and predict the air damping of lateral MEMS oscillators, actual measurements of devices are necessary. Details on the fabrication procedure are presented in appendix A. The geometrical parameters that determine the damping force Eq. (2.26) are, apart from length, width and height of the oscillating plate, the gap widths x_r and y_r. The in-plane gap in z-direction, z_r (see Fig. 2.2) was neglected in the model since the corresponding damping force is expected to be small. This applies also to the effect of the holes in the proof mass. In spite of their large number, the corresponding forces F_t and F_b are assumed to be mostly unaffected by them. All these aspects were tested by accordingly designed MEMS structures [32–37]. The only exception is the parameter y_r. This parameter is determined by the SU-8 bonding spacer, which has the same height across the whole wafer being processed. Thus, a sweep of y_r with a reasonable number of values would have required a large number of individually processed wafers which would have been far too expensive.

2.3.1. Measurement Setup

Since the MEMS transducers are passive devices, optoelectronics and mechanic actuation have to be provided externally for characterisation. The measurements in this section were performed applying constant mechanic actuation amplitudes while stepping through a range of frequencies. This corresponds to the case referred to as vibration sensor in subsection 1.2.

The MEMS chip itself was held by a PEEK (polyether ether ketone) slice and fixed onto that by a metal spring. Both the spring and the slice contain a hole in their centres that allows the light to pass through the MEMS. As light source an LED was used. In this case a near infrared LED (Osram SFH 4680) which features a curved reflector that minimises the emission divergence. The modulated light that had passed through the MEMS was detected with a phototransistor (Osram SFH 3600). Both the LED and the phototransistor were mounted onto a PEEK slice identical as the one holding the MEMS [13,14]. The stack comprising LED, MEMS and phototransistor was then inserted in a PEEK housing. This housing was mounted onto a custom made piezoelectric shaker [50] which provided the actuation. It was supplied with a sinusoidal voltage from a waveform generator Agilent 33220A. For larger mechanical amplitudes, an optional amplifier for the piezo voltage was available. The resulting displacement amplitude is measured by the laser-Doppler vibrometer of a Polytec MSA 400 microsystem analyser[5]. Since the housing features a hole at the top, it was possible to measure the amplitude directly at the frame of the MEMS. During the measurement, the analogue output signal of the vibrometer was recorded by a lock-in amplifier (Stanford Research SR830). An overview of the setup is given in Fig. 2.9.

The reference measurement of the actuation amplitude is necessary to monitor if eigenmodes of the shaker and/or the sensor mounting are excited. These modes occur usually at frequencies above 2 – 3 kHz. Based on this monitoring the recorded characteristic of the sensor can be cleaned from the corresponding artifacts. Furthermore, the vibrometer provides the information on the mechanical displacement of the actuation. This way, the output voltage of the sensor's readout can be linked with the input vibration.

At the same time the actuation was picked up by the MEMS transducer. The photocurrent

---

[5] The laser-Doppler vibrometer actually measures the velocity of the moving object. The displacement is thereby obtained via integration.

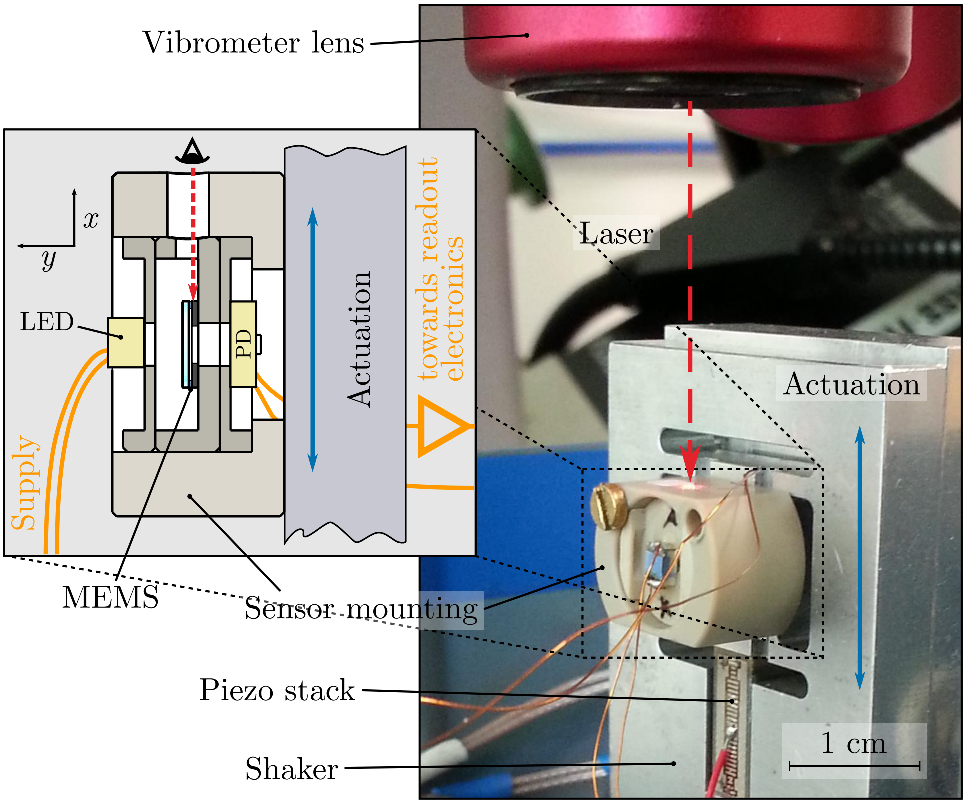

Figure 2.9.: Measurement setup. The optoelectronics and the MEMS transducer are positioned inside the housing in such a way that the light emitted by the LED is detected by the phototransistor after being modulated by the MEMS. The mounting is fixed to the piezoelectric shaker that provides the mechanical actuation.

produced by the optomechanical sensor was converted into a voltage by a transimpedance amplifier circuit [14] (see appendix B). The resulting signal was then recorded by a second lock-in amplifier (also Stanford Research SR830).

The measurements were performed fully automated using a PC running a Python script that controls the waveform generators as well as both of the lock-in amplifiers. See Fig. 2.10 for a schematic of the setup. The script also took care of removing the eigenmodes of the excitation system, integration of the vibrometer data and calculating the transfer characteristics of the individual MEMS sensors. The corresponding values of the resonance frequency, decay parameter and sensitivity could then be extracted from the data. This was achieved by fitting the lumped parameter model Eq. (1.4) to the data using a least-squares routine.

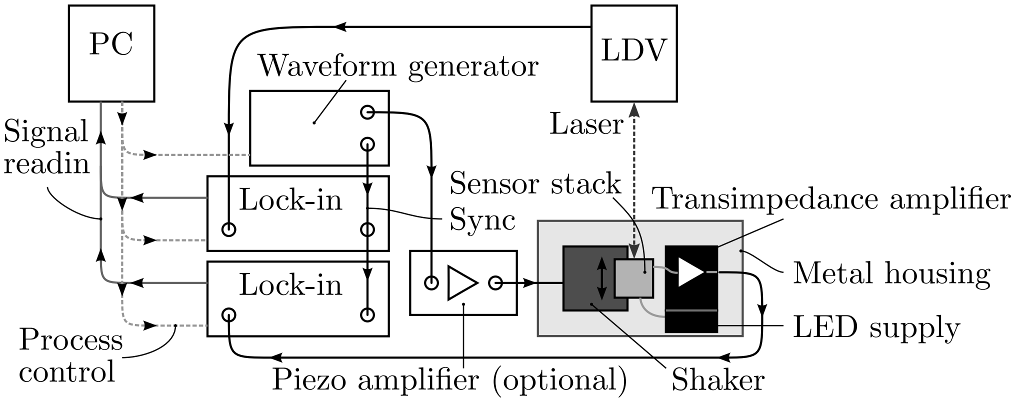

Figure 2.10.: Schematic of the measurement setup.

2.3.2. Results of the Parameter Sweeps

The first parameter that was investigated was x_r which is the width of the squeezing gap. Five layouts were designed with different values of $x_\mathrm{r} \in [4, 10, 20, 100, 200]$ µm [34, 36, 37]. As mentioned above, the other dimensions were kept constant and matched the ones used in the analytical and numerical models. The size of the proof mass was given by $l = w = 2$ mm and $h = 45$ µm. The other in-plane gap was set to $z_\mathrm{r} = 50$ µm and the out-of-plane gap given by the height of the SU8 bonding spacer was $y_\mathrm{r} = 5$ µm. The width and length of the holes was $w_\mathrm{h} = 10$ µm and $l_\mathrm{h} = 100$ µm, respectively and they were placed at a distance of 10 µm from one another. Furthermore, the layout of the springs was the same for all these MEMS. It was, thus, ensured that the test structures had the same effective mass and stiffness and, therefore, the same resonance frequency. For each value of x_r five identical MEMS were fabricated. This way, possible losses due to handling or during fabrication were accounted for and the reproducibility of the fabrication process was investigated.

The test structures were measured in the setup described in the previous subsection by stepping through a range of frequencies that contains the resonance peak. To avoid systematic errors during evaluation of the data, the step width was set sufficiently small in the region of the resonance. The obtained mean resonance frequency of all MEMS devices was determined to be $\omega_0 = 9006$ s^{-1} or $f_0 = 1433$ Hz with a standard deviation of 925 s^{-1} or 147 Hz, respectively. This fluctuation of roughly ten percent reflects variations in the fabrication processes. These were also observed in the actual width x_r of the test devices. Measurement of the width with an optical microscope revealed that the gaps were enlarged by approximately 1 - 2 µm. This had of course a large influence on the observed damping, especially for small values of x_r where the damping is mainly determined by the squeeze

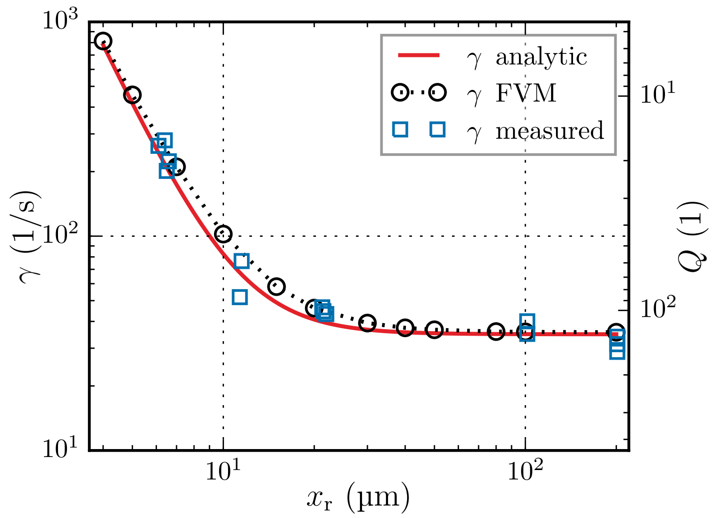

Figure 2.11.: Decay parameter $\gamma = d/2m$ and corresponding quality factor Q depending on the in-plane gap x_r. The measured data points (blue squares) is in good agreement with the analytical (red line) and numerical models (black circles) depicted in Fig. 2.8.

film.

The corresponding decay parameters in dependence on the measured x_r are shown in Fig. 2.11. The results prove that both the analytical model and the FVM describe the damping of the MEMS very well. Furthermore, this parameter sweep reveals that by setting x_r during MEMS design the quality factor can be adjusted in a wide range, in this configuration roughly 1 - 1.5 orders of magnitude. Note, however, that if the gaps are designed too small, the etching will remain incomplete rendering the proof mass immobile and the MEMS faulty.

The second parameter sweep was intended to check if the in-plane gaps in z-direction affect the damping noticably. Therefore the parameter z_r was varied. It was set to four different values, $z_\mathrm{r} \in [3, 6, 10, 50]$ µm [34, 36, 37]. Again five copies were fabricated for each value. The remaining dimensions were the same as for the x_r sweep but with fixed $x_\mathrm{r} = 200$ µm. The resulting decay parameters are plotted in Fig. 2.12. No evident effect of the gap spacing on the damping was observed. There might be an effect for values of z_r even smaller than 3 µm, but this would be neither practical nor feasible. Nevertheless, it can be concluded that it was in order to neglect the corresponding damping force F_s (see Fig. 2.2) during modelling.

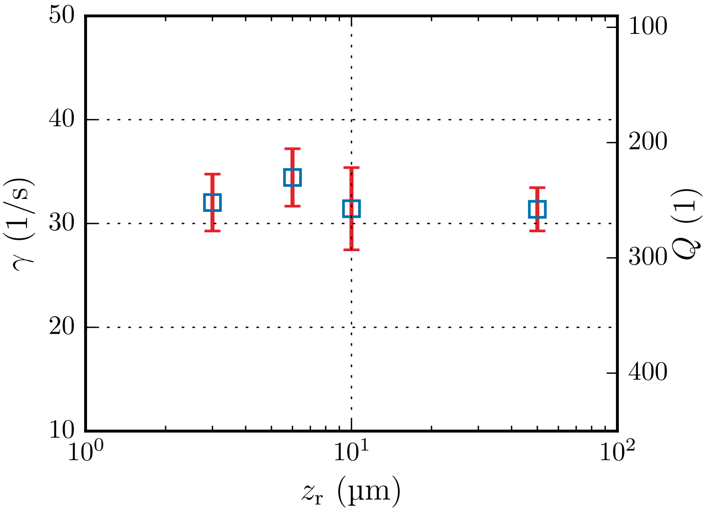

Figure 2.12.: Decay parameter $\gamma = d/2m$ and corresponding quality factor Q depending on the in-plane gap z_r. It can be seen that the gap has no measurable influence on γ or Q.

Another contribution that was not considered in the analytical model was the effect the holes have on the damping. Due to these holes, the assumption of a perfect plate that was made for modelling the forces F_t and F_b is certainly not fulfilled. A preliminary FVM simulation [32] suggested that the holes have little influence, since pressure forces increase almost at the same rate as viscous forces decrease with the number of holes. Since these simulations were based on just one configuration of holes (w_h, l_h, d_h), a more thorough investigation was performed experimentally [35, 37].

This investigation consisted of two parameter sweeps, one varying both the width of and the distance between the holes while ensuring $w_\mathrm{h} = d_\mathrm{h}$, the other keeping $w_\mathrm{h} = 10$ µm constant while varying d_h (compare Fig. 1.1). The undertaken variation of $w_\mathrm{h} \in [5, 7, 10, 12, 15, 20, 25, 30]$ µm changes the distribution of *open* regions on the inertial plate while the mass approximately stays the same. The sweep of $d_\mathrm{h} \in [10, 12, 15, 20, 25, 30]$ µm, on the other hand, effects a change in mass. In both cases the total number of holes N_h decreases with increasing sweep parameter. As before, five copies each were fabricated and all other dimensions were the same for all layouts. Since these MEMS were processed on a different wafer than the ones before, the value for $y_\mathrm{r} \approx 6$ µm differed slightly. Additionally, the stiffness was reduced by a factor of four, resulting in a lower resonance frequency. For the w_h MEMS, the mean resonance frequency was $\omega_0 = 4739$ s^{-1} with a standard deviation

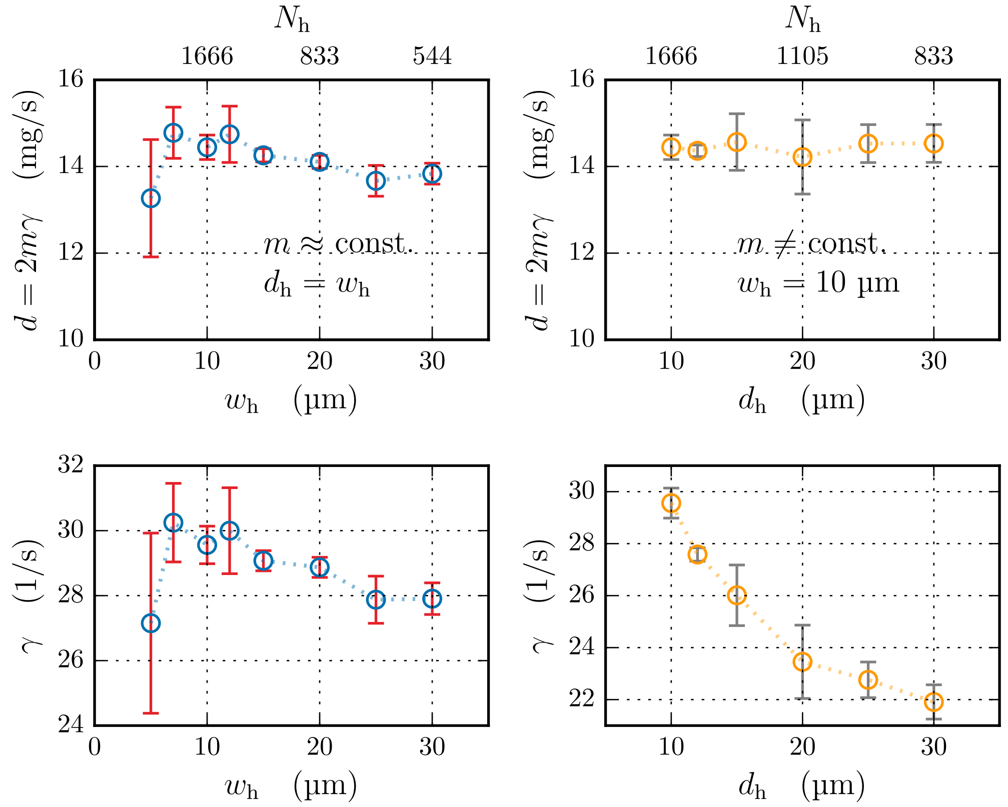

Figure 2.13.: Dependence of the damping on the holes in terms of both the damping parameter d (top) and decay parameter γ (bottom). The left panels correspond to the variation of w_h with $d_h = w_h$ and the right panels to the variation of d_h with $w_h = 10$ µm (compare Fig. 1.1).

of 188 s^{-1} or $f_0 = 754$ Hz with a standard deviation of 30 Hz which is approximately by a factor of $\frac{1}{2}$ lower than in the previous sweeps. Throughout the d_h set the mass and hence ω_0 changes, i.e. $[4668, 4620, 4439, 4144, 4262, 4051]$ s^{-1} with standard deviations of $[74, 157, 109, 190, 144, 136]$ s^{-1}.

The observed damping of both test series is depicted in Fig. 2.13 in the form of both d and $\gamma = d/2m$. The plots of d show no evident dependence on w_h or d_h within the respective range of values. This means that the actual damping force which is proportional to d is also not affected by the holes. Only the decay parameter of the d_h series exhibits a considerable dependence. This effect, however, is solely due to the accompanied change in mass on which γ depends. Thus, it can be concluded that the quantitative influence of the holes on the damping can be neglected and that the model Eq. (2.12) can safely be used even though it is, strictly speaking, not correct.

2.4. Potential for Optimisation

As seen in the previous sections, the strength of the damping d can be fine tuned by adjusting the size (l, w, h) of the proof mass and the gap widths $(x_{\mathrm{r}}, y_{\mathrm{r}})$. Since this applies to the remaining two parameters of the oscillator (m,k), too, it is, in principle, possible to design a transducer with a specific transfer characteristic. The accuracy of this is, however, still limited by remaining imprecisions of the model and fluctuations during the fabrication processes. Furthermore, while it is possible to exploit the air damping design to a MEMS that completely suppresses overshoot, i.e. $Q = 1$, it is not possible to achieve arbitrarily high quality factors. Such high Qs are only feasible in a reduced pressure environment.

Given the example of a vibration sensor, a low quality factor is preferable to avoid ringing and a low resonance frequency to extend the measurement range (compare Eq. (1.4)). Therefore, it was attempted to manufacture transducers with $Q \gtrsim 1$ and a reasonably low f_0 of a few hundred Hz. The first attempt was processed on the same wafer as the structures of the x_{r} and z_{r} test series. Thus, $y_{\mathrm{r}} = 5$ µm and $h = 45$ µm. The gaps were made *as narrow as reasonably possible* meaning that $x_{\mathrm{r}} = 4$ µm and $y_{\mathrm{r}} = 3$ µm which correspond to the smallest values of the respective sweeps. The mass was designed slightly larger, i.e. $w, l = 2.5$ mm$, 2$ mm to increase the amount of squeeze film damping. Given these parameters, the decay parameter was estimated using the analytical model Eq. (2.26) and an FVM simulation. These yielded $\gamma = 741$ s^{-1} and $\gamma = 799$ s^{-1}, respectively. Again five copies were intended, of which only one survived fabrication and handling. This structure named *E0* was then characterised in the setup described in the previous subsection. The transfer function was recorded using several different mechanical actuation amplitudes and is depicted in Fig. 2.14.

The fit of the data revealed a resonance frequency of $f_0 = 325$ Hz and a decay constant of $\gamma = 449$ s^{-1} which corresponds to a quality factor of $Q = 2.275$. These values were obtained by averaging over the results corresponding to the three different actuation amplitudes. The measured decay constant differed from both the analytically and numerically estimated ones, since at that time the broadening of the gaps due to fabrication was not considered. In the case of the E0, the in-plane gap increased to $x_{\mathrm{r}} \approx 5$ µm. Taking that into account, the analytical model yielded $\gamma = 396$ s^{-1} and the FVM simulation $\gamma = 448$ s^{-1}, which both agree well with the measurement. Due to this broadening, however, the quality factor was

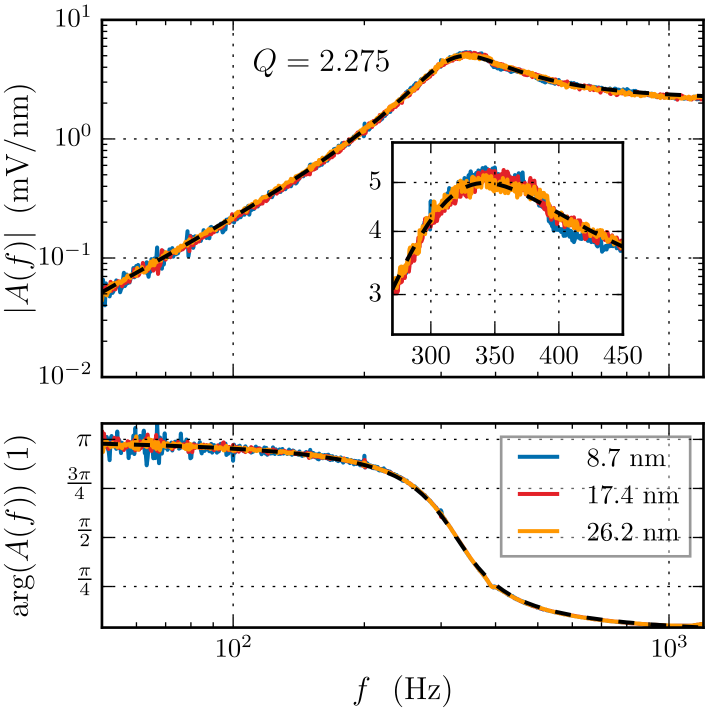

Figure 2.14.: Transfer function of the strongly damped structure E0. The coloured lines represent the measured data obtained for different actuation amplitudes, whereas the black dashed line corresponds to a least-squares fit.

nearly doubled and thus the goal of $Q \approx 1$ was not reached.

Therefore, another attempt was made which involved even smaller gaps. The nominal gap width for the MEMS layout was reduced to $x_{\mathrm{r}} = 3.5$ µm while the dimensions of the proof mass were the same as for the E0. The SU8 bonding spacer was $y_{\mathrm{r}} = 6$ µm thick. Furthermore, the stiffness was reduced since a resonance frequency causes a lower Q. Compared to the E0 which featured a nominal stiffness of $k = 3.1$ N/m, two layouts with lower stiffnesses of 1.6 N/m and 2.3 N/m were designed. Of these layouts five copies each were fabricated which will be referred to as *group 1* and *group 2*. Note that the fabrication process also affects the width of the springs significantly. Thus the actual spring constants are lower than their nominal values. In the case of the E0, the resonance frequency was 325 Hz instead of the nominal 516 Hz. Therefore, it had to be expected that the resonance frequency of the test groups were also lower than their nominal values of $\omega_0^{\mathrm{group1}} = 2090\ \mathrm{s}^{-1}$ and $\omega_0^{\mathrm{group2}} = 2522\ \mathrm{s}^{-1}$, respectively. The nominal decay constants were calculated to be $\gamma^{\mathrm{group1}} = \gamma^{\mathrm{group1}} = 1163\ \mathrm{s}^{-1}$ using the analytical model and $\gamma^{\mathrm{group1}} = \gamma^{\mathrm{group2}} = 1193\ \mathrm{s}^{-1}$

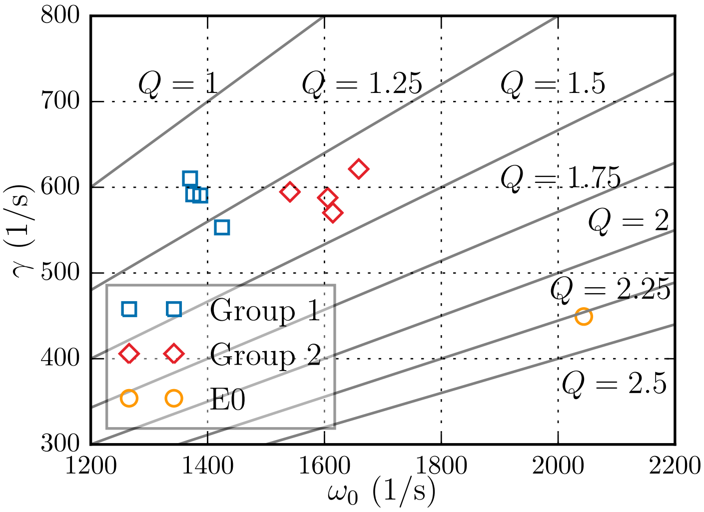

Figure 2.15.: Parameters of the E0 (orange circle) compared to the sets entitled group 1 (blue squares) and group 2 (red diamonds). The decay parameter γ is plotted against the (angular) resonance frequency ω_0. In this representation, the straight grey lines are lines of equal Q.

using the FVM. Taking into account an estimated broadening of the gap by 1 µm, the analytical and numerical decay constants were approximately halved, i.e. 564 s^{-1} and 562 s^{-1}, respectively.

The results for the two sets of test structures are plotted in Fig. 2.15. The mean resonance frequencies were $\omega_0^{\mathrm{group1}} = 1389$ s^{-1} and $\omega_0^{\mathrm{group2}} = 1604$ s^{-1} and the decay parameters $\gamma^{\mathrm{group1}} = 586$ s^{-1} and $\gamma^{\mathrm{group2}} = 594$ s^{-1}. This suggests that the assumed broadening of 1 µm was a good estimation. The corresponding mean quality factors were, therefore, $Q^{\mathrm{group1}} = 1.16$ and $Q^{\mathrm{group2}} = 1.35$. This proved that $Q \approx 1$ is achievable by design of the MEMS alone and that active force feedback is not necessary to suppress ringing. Since the measured values deviate from the nominal ones, it is, however, crucial to know the processes used for the fabrication.

If the opposite case of high Q is desired, e.g. for resonant sensing applications, it might be necessary to reduce the air pressure. While it is possible to make the gaps x_r and y_r *as large as possible*, the air damping can only be minimised to a certain extent. The lower limit for that is given by the viscous shear force $F_\mathrm{min} \approx 2F_\mathrm{b}$ acing on the area A_m (see Figs. 2.6 and 2.11). The area A_m can, of course, also be reduced, but only at the expense of the number of holes and hence of the sensitivity. The same is true for increasing the stiffness k. All in

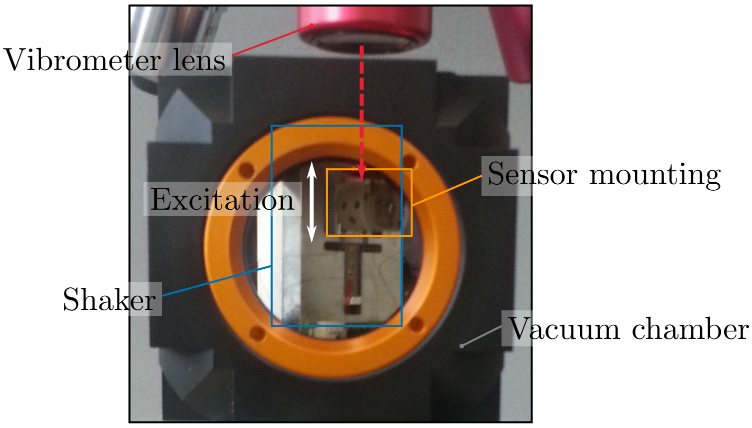

Figure 2.16.: Measurement setup using a vacuum chamber.

all, the quality factor of the MEMS transducer can be increased in ambient pressure up to a several hundred or even one thousand. If an even higher Q is necessary, this is only possible by reducing the pressure. This was tried out by measuring the transfer characteristic in vacuum.

In order to realise that, the MEMS stack already mounted onto the shaker was put into a vacuum chamber (see Fig. 2.16). The electronic readout circuit was placed outside the chamber. The electric connections to the optoelectronics and the piezo were established via a vacuum-tight feed-through. The chamber was placed under the sensing head of the vibrometer. It featured a glass window on the top side so that the actuation vibration could be picked up by the laser. After installation, the air was pumped out using a turbomolecular pump with a rotary vane prepump. By these means, the pressure could be lowered to $p = 3 \cdot 10^{-4}$ mbar which is in the high vacuum regime.

Exemplatory Bode plots of a test structure measured in both ambient pressure and in high vacuum are shown in Fig. 2.17. The fit of the measurements in ambient pressure revealed an angular resonance frequency of $\omega_0 = 4870\ \mathrm{s}^{-1}$ ($f_0 = 775$ Hz) and a decay constant of $\gamma = 38.7\ s^{-1}$ which corresponds to a quality factor of $Q = 63$. In vacuum a much weaker dissipation was observed manifesting in $\gamma \approx 0.29\ \mathrm{s}^{-1}$. Thus, the quality factor increased to $Q \approx 8400$. Note that the values of γ and Q in the low pressure case are entailed with uncertainties. This is due to the way they were acquired as a fit of the measured frequency responses. This method is less reliable for low damping, since it critically depends on the frequency resolution at the resonance peak. In hindsight, a ring-down measurement would have been more appropriate.

Nevertheless, it was shown that also high Qs are feasible with this transducer. If the

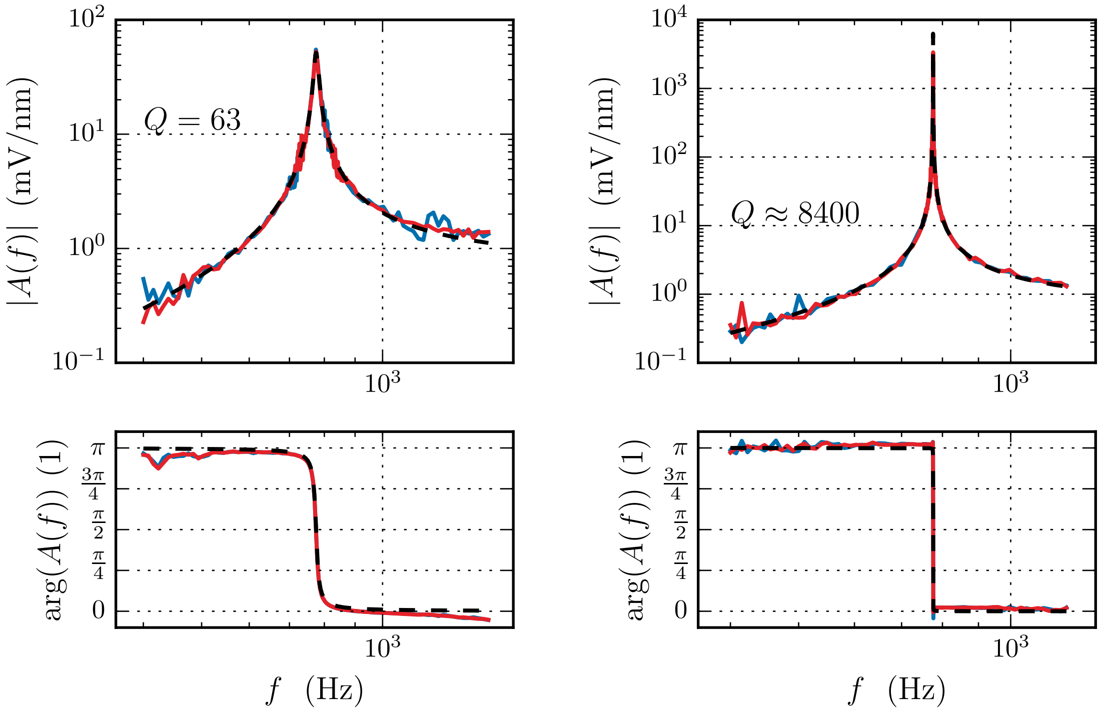

(a) $p = 1$ bar

(b) $p = 3 \cdot 10^{-4}$ mbar

Figure 2.17.: Frequency response of a test structure. The quality factor increases dramatically if the pressure decreases. The red and blue lines correspond to different actuation amplitudes.

sensor is placed in a vacuum-tight package, the quality factor can be controlled in the range $1 \lesssim Q \lesssim 10^4$. If, for some reason, even higher values of Q are desired, one has to optimise damping mechanisms other than air damping.

The model derived in this chapter also helps to explain the relatively low quality factors of the electric field sensors introduced in chapter 4. There, the sensitivity of the electric field transduction depends on the gap width x_r. Since small gaps are favourable for high electrostatic forces, the model well applies to this type of MEMS.

Chapter 3.

Optomechanic Sensitivity and Efficiency

The sensitivity S of the optomechanical transducer is one of its strongest advantages. As briefly discussed in subsection 1.1.1, the larger the effective edge length $L_\mathrm{h} = N_\mathrm{h} l_\mathrm{h}$ the larger output voltage for a given input displacement. Thus, S can in theory be chosen arbitrarily high by increasing the number of holes on an available area A_m. In practice, this is, of course, not true. The number of holes N_h would be increased at the cost of the width w_h of the holes. This, in turn, limits the maximum displacement, ideally $w_\mathrm{h}/2$, that can be detected and, therefore, the dynamic range.

Another aspect affecting the sensitivity is the energetic irradiance E_e and this way the MEMS is illuminated. Ideally, the two grids are illuminated by perpendicularly incident light that is perfectly collimated. That way, unwanted shadowing effects due to the distance between the grids are minimised. Furthermore, only the *active area*, i.e. the grid area, should be illuminated in order to efficiently use all of the light provided. In reality, a simple, commercial LED was used as light source which does not comply with the aforementioned properties. Instead, it can be sufficiently accurately viewed as point source with a certain radiation angle. Thus, both the local irradiance and incidence angle are not constant at the MEMS surface. Therefore, only the holes located at the centre of the chip are used efficiently, whereas the ones at the edges hardly add to the transduction. These effects lead to a considerable loss in sensitivity for a given LED current.

In this context, several approaches to deal with these issues were tried out. First, a simple Fresnel grating was structured in order to increase the light flux inside the holes in the proof mass of the MEMS. The illumination of the active area was attempted to be homogenised by using large area organic optoelectronics[1] and ray divergence losses of the conventional LEDs were reduced using an optical lens. As reference, measurements of

---

[1] These offer also other opportunities to improve the transducer; see subsection 3.2.3.

MEMS devices with varying N_h were conducted with a collimated laser diode.

3.1. Impact of the Number of Holes

Since the effective edge length L_h is the central parameter defining the sensitivity S of the optomechanical transduction, it was investigated if the linear behaviour $S \propto L_\mathrm{h} \propto N_\mathrm{h}$ stated in Eq. (1.1) is observed even if non-collimated light sources are used.

In order to test that, measurements of MEMS transducers with varying L_h were performed. The devices used for that purpose were the same devices as for the d_h sweep (see subsection 2.3.2). These devices previously used to investigate the influence of the holes on the damping have the exact same layout differing only in the distance between the holes and thus in N_h. The size of one hole was set to $w_\mathrm{h} = 10$ µm and $l_\mathrm{h} = 100$ µm. The resulting six layouts featured a number of holes ranging from 833 to 1666 which corresponds to $8.33\ \mathrm{cm} \leq L_\mathrm{h} \leq 16.66\ \mathrm{cm}$.

The measurement setup was, in principle, the same as presented in subsection 2.3.1. The only difference were the light sources and detectors used. The reference measurement was performed with a perfectly collimated light source. This was provided by a laser diode CPS532 (Thorlabs) which emits a peak wavelength of $\lambda_\mathrm{peak} = 532$ nm. Thus, the phototransistor (Osram SFH 3600) used previously has to be replaced by a suitable detector. In this case, a photodiode (Vishay TEMD5510FX01) was chosen. For the LED measurements in this context, the same detector should be used. Hence, an LED emitting green light (Osram LT T673-N2S1-35, $\lambda_\mathrm{peak} = 529$ nm) was installed.

The transducers were measured once with the laser diode and once with the LED as light source. The sensitivities of the test devices were obtained via a least-squares fit of the measured frequency response. The results for the sensitivity are shown in Fig. 3.1. Since the laser and the LED have different emission power which reflects in E_e, the sensitivity is normalised relative to the corresponding one of the first set of test devices S_0. It can be seen that using collimated light the sensitivity increases linear with the number of holes. The measurements with the LED also exhibit this linear behaviour, but less clearly. This might be due to the LED's emission angle which makes the system more prone to alignment or tilt errors.

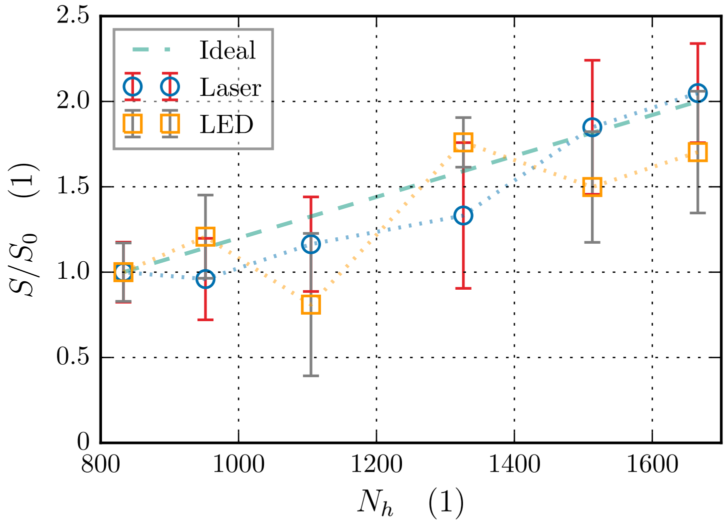

Figure 3.1.: Normalised sensitivity S of the optomechanical transducer as function of the number of holes N_h. Both measurements performed with laser and LED follow the ideal linear behaviour (dashed line). Having a non-collimated light source (LED), however, seems to make the system's sensitivity more error prone.

3.2. Increasing the Optical Efficiency

As proven in the previous section, the sensitivity is proportional to the effective edge length. Another parameter that can be optimised in this regard is the irradiance E_e. The easiest way is, of course, to increase the driving current of the LED. The photocurrent of the detector and, thus, also the output voltage would, therefore, increase at the same rate [14]. This would be at the cost of higher power consumption which might be a limiting factor. There are, however, other possibilities to increase the irradiance without changing the LED current. Since the light of the LED originates at the PN junction and the semiconductor material is not very transparent, most of the light is emitted along the edges of the LED [51]. As a result, LEDs have a very high emission angle θ_e that can be narrowed down to a certain extent by the package. For instance, the package of the green LED used in the previous section consists only of a white plastic casing with a small circular cavity containing the LED. Thus, the emission angle is quite high, i.e. $\theta_\mathrm{e} = 60°$. In contrast to that, the package of the near IR LED used in the previous chapter features a semispherical reflector resulting in $\theta_\mathrm{e} = 20°$. In the following, several approaches to tap that unused light are investigated.

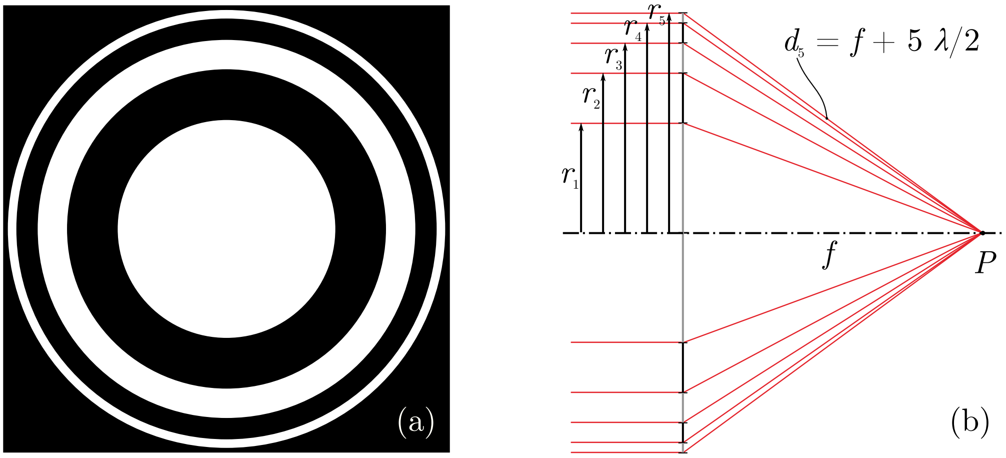

Figure 3.2.: Fresnel zone plate consisting of alternating transparent (white) and opaque (black) rings (a) and its working principle (b). The light arriving at point P from the transparent zones interferes constructively leading to increased irradiation in P.

3.2.1. Diffraction Grating

Up to now diffraction phenomena were not considered. This was due to the fact that the geometrical spacings of the grid and along the optical path were large enough to neglect such effects. Diffraction would disturb the exploited *simple* shadow sensing principle utilised by the transducer. Nevertheless, it is in theory possible to exploit such diffraction phenomena to increase the sensitivity. One attempt was made by implementing diffraction gratings in the first grid in order to focus the incident light into the apertures of the second one, thus increasing the usable light flux through constructive interference.

The underlying principle of this approach is inspired by the Fresnel zone plate, a circular diffraction grating consisting of alternatingly transparent and opaque rings [52], which is a basic component especially in X-ray optics [53–55]. An example is depicted in Fig. 3.2. The width of these rings decreases with the distance from the centre. Thus, given, e.g., an incoming plane wave, the light is focussed at a point P by superposition. The distance f of this point from the zone plate, i.e. the focal length, is determined by the wavelength λ of the light and the radii r_n defining the rings. The distance the light has to travel from the edges of the rings to P is given by $d_n = \sqrt{r_n^2 + f^2}$. If the length of the path d_{n+1} is $d_n + \lambda/2$, the alternating opaqueness guarantees that the light from the transparent zones arrives at

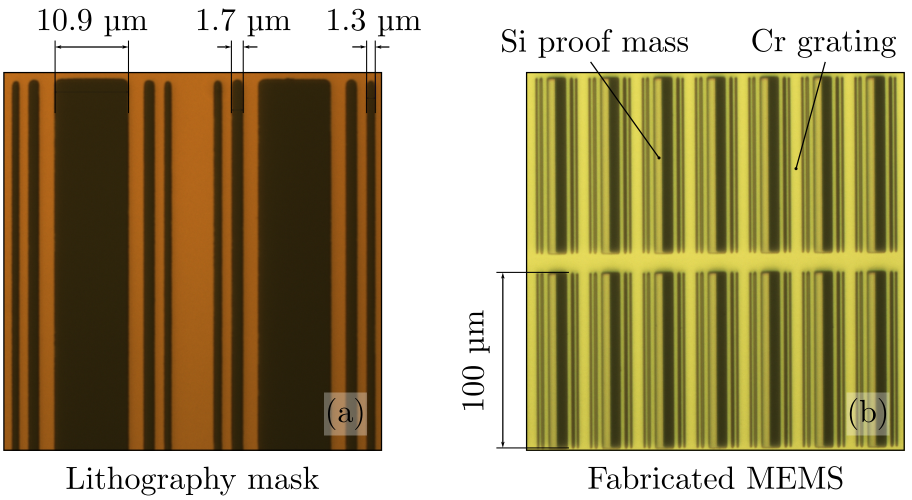

Figure 3.3.: Micrographs of the implemented Fresnel grating. (a) shows the lithography mask, (b) a manufactured MEMS including the Si chip. The smallest structure on the mask was measured to be 1.3 µm matching the calculated width of $r_5 - r_4 = 1.32$ µm.

P with the same phase. Thus, the radii of the zones are given by

$$r_n = \sqrt{n\lambda \left(f + \frac{n\lambda}{4} \right)} \tag{3.1}$$

The more zones are available, the greater the intensity at the focal point.

Circular gratings are not optimal for the transducer, if one wants to exploit the large effective edge length L_h. Thus, the intended diffraction grating was designed as parallel rectangles featuring the same cross-section as the original Fresnel zone plate. By this means, each of the holes in the Si proof mass was provided a Cr grating of equal length. The zones were tailored to the peak wavelength of the LED (880 nm) and a focus lying in the Si hole. However, since the lithography process did not allow for arbitrarily thin zones, only radii until r_5 could be included in the layout. Fig. 3.3 shows the fabricated gratings. Results of FEM simulations of the diffraction of these gratings are depicted in Fig. 3.4 in which the qualitative performance is compared to the normal hole. It can be seen in (f) that due to the relatively high thickness of the device layer, most secondary waves coming from the lateral slits are blocked by the Si proof mass. Only the inner slit on the lower side contributes. Unfortunately, this diminishes the desired enhancement significantly.

Nevertheless, based on these simulations, a small enhancement could be expected. Thus, test devices featuring these gratings were designed and measured. As reference, identical

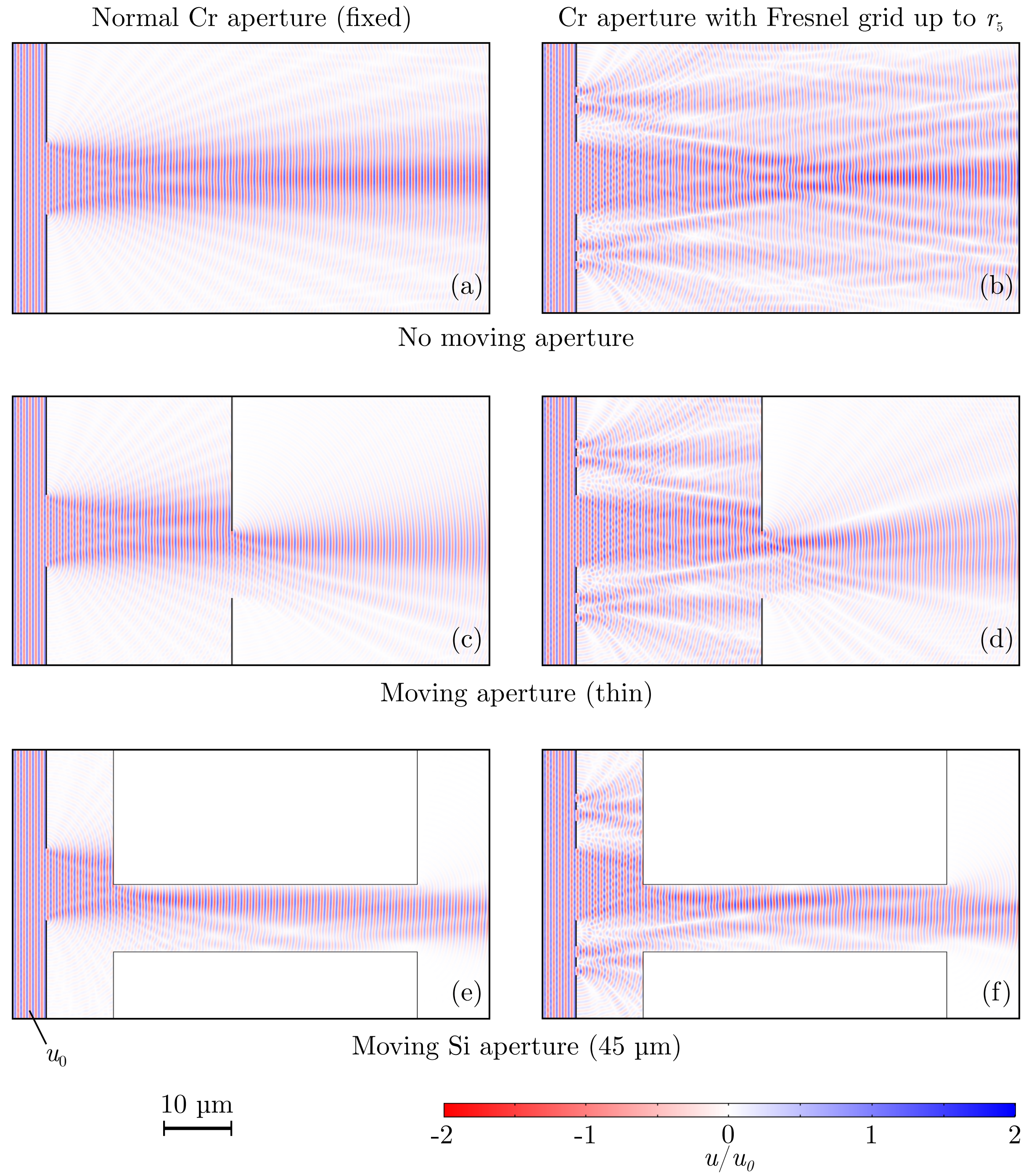

Figure 3.4.: FEM simulation of the focussing behaviour of the diffraction grids compared to the normal hole in terms of the wave amplitude u with respect to the incoming wave amplitude u_0. In (a) and (b) there is no hole in the focal plane, in (c) and (d) a *thin* hole and in (e) and (f) an actual hole with 45 µm height.

MEMS with regular were fabricated. The holes of reference structures had the same width ($2r_1 = 10.7$ µm) as the central zone of the diffraction grating. Furthermore, the pitch (25 µm) was equal. The measured structures (five with and five without grating) had a resonance frequency and decay parameter of $f_0 = 637.4 \pm 68.4$ Hz and $\gamma = 34.26 \pm 3.1$ s^{-1}, respectively.

Unfortunately, the sensitivities of the two groups did not differ clearly. The diffraction group exhibited a mean sensitivity of $S = 3.25 \pm 0.88$ mV/nm while one of the reference group was $S = 3.68 \pm 1.35$ mV/nm.

Due to alignment and tilt errors arising while exchanging the individual MEMS, the margin of fluctuations is quite large. Furthermore, the finite bandwidth of the LED causes a blurring of the desired superposition. Thus, based on these measurements it unfortunately can neither be clearly argued in favour of the effect nor against it. Nevertheless, even if there is any effect, it is too small to matter.

3.2.2. Collimating the LED light

Another attempt to increase sensitivity and efficiency was made using optical lenses to collimate the divergent light emitted by the LED. For the sake of compactness the lens had to have very small dimensions and focal length. Therefore, a large refraction index and small radius of curvature is necessary. For the present case a plano-convex lens (Edmund Optics # 65-301) with an effective focal length and diameter of 2.5 mm each was chosen. The area of the lens fits well to the sensitive area of the MEMS transducer. The lens material was *N-LASF9*[2] which has a very high refractive index of $n = 1.86$.

The lens was mounted onto a PEEK slice the same way as the LED and Photodetector (compare subsection 2.3.1). This slice was placed in between the slices holding the LED and the MEMS. The aim was to place the emitting surface (actually frame - due to the electric contacts) of the LED in the focal plane of the lens, i.e at a distance equal to the back focal length $BFL = 2.05$ mm. It had to be considered that the emitting semiconductor material of the LED was embedded in silicone to keep it safe. As a result, the emitting plane appeared closer to the surface of the LED housing than it actually was. The appearing distance $s' = s\,n_\mathrm{a}/n_\mathrm{s} \approx s/n_s \approx 0.71s$ from the surface to the plane is given by the actual distance s according to the data sheet and the refractive indices of silicone and air, n_s and n_a, respectively. However, since neither the refractive index nor the type of the silicone was mentioned in the data sheet, the correct value of n_s is unclear. It was estimated taking a refractive index of $n_\mathrm{s} = 1.4$. With a distance of $s = 0.8$ mm given in the data sheet, the

---

[2] Lanthanium dense flint optical glass

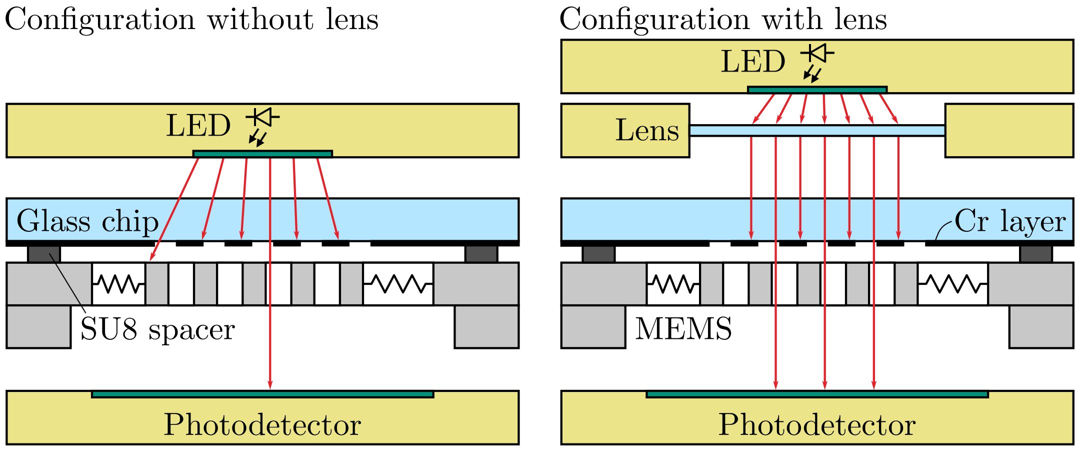

Figure 3.5.: Schematic of the configuration with and without lens. The lens collimates the divergent light of the LED and thus increases the irradiation and the sensitivity of the sensor.

emitting surface appears roughly 0.23 mm closer.

The required distance was approximately achieved through the height of the PEEK slices of 2.5 mm. A schematic of the alignment with and without lens is shown in Fig. 3.5 and a ray tracing analysis in Fig. 3.6. In this simulation the LED was approximated as a point source and the reflector of the SFH 4680 as spherical. Despite the plainness of the simulation it can be observed, that the lens effects an increase in irradiation on the MEMS gratings which, in turn, enhances the sensitivity.

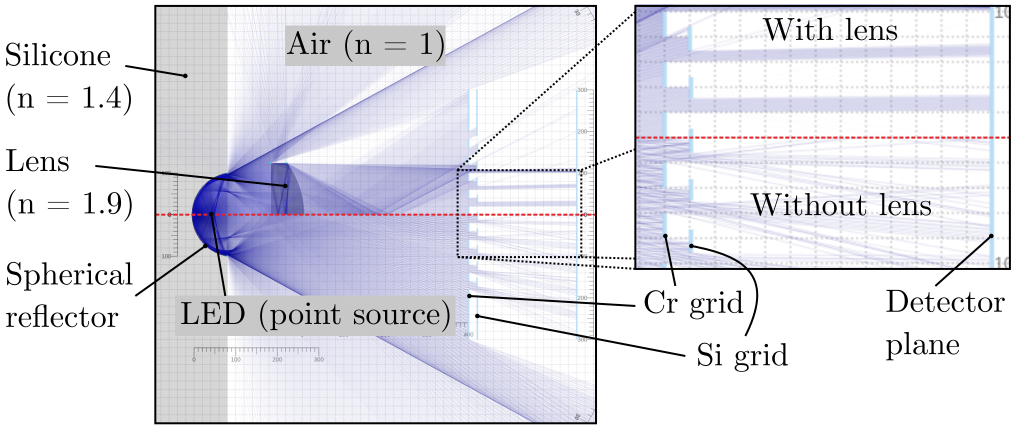

Figure 3.6.: Raytracing simulation comparing the configuration with lens (top) and without lens (bottom).

In order to test if this effect is indeed observable, the transfer characteristic of a transducer was measured for both cases; without and with collimating lens in the setup described

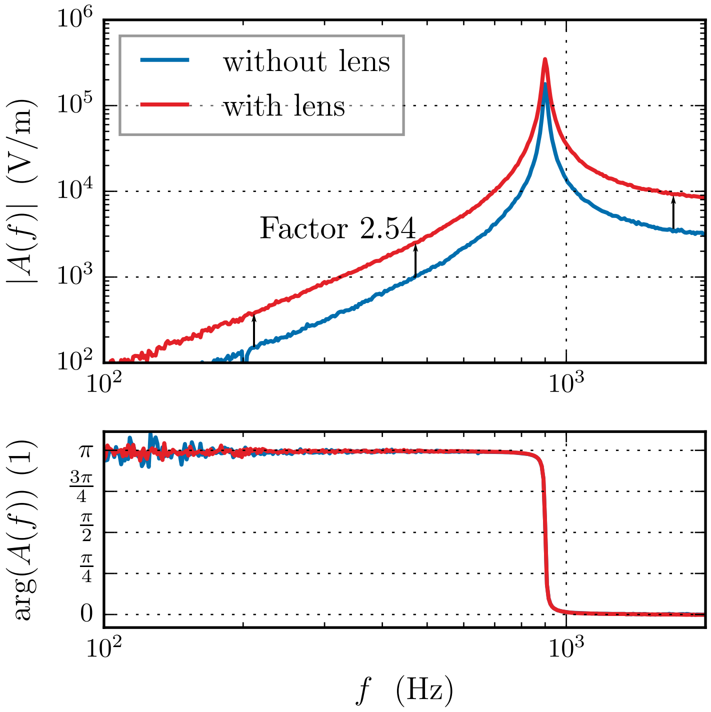

Figure 3.7.: Transfer functions of a transducer with $f_0 \approx 910$ Hz. The blue curve was measured without lens, the red one with the collimating lens revealing an increase in sensitivity of a factor 2.54.

in subsection 2.3.1. Both measurements were conducted with the same LED current of $I_{\mathrm{LED}} = 10$ mA. The resulting bode plots comparing both measurements are shown in Fig. 3.7. The lens improved the sensitivity by a quite large factor of 2.54, showing a way to more efficently exploit the available light flux. This improvement was investigated in more detail in a project work [56], that compared different lenses and also analysed the collimation behaviour as well as the power saved due to the lenses.

3.2.3. Organic Optoelectronics

Over the last one to two decades, more and more consumer electronics devices have emerged relying on organic optoelectronics. Today, e.g., most smartphone displays, monitors and TVs employ organic LEDs (OLEDs) as light source. This is primarily due to the inherent advantages of the technology. Organic optoelectronics can be fabricated at low cost and featuring extensive areas. Furthermore, since the substances can be processed in solution, they offer the possibility to be ink-jet or screen printed which is favourable regarding

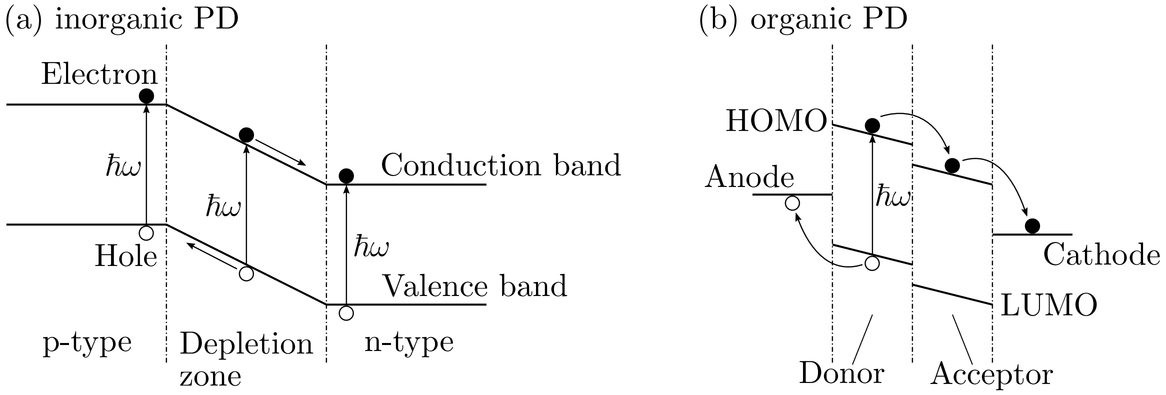

Figure 3.8.: Energy level diagrams showing the working principle of an inorganic photodiode (a) and an organic PD (b). The highest occupied molecular orbitals (HOMO) of the OPD's donor and acceptor molecules correspond to the conduction band of the PD and the lowest unoccupied MOs (LUMO) to the valence band.

throughput. In addition, they can be applied on flexible substrates. However, the most prominent downsides of these organic components are their limited robustness and lifetime, since they are by far less resilient against high temperatures or chemical decomposition (e.g. due to atmospheric oxygen or water). Nevertheless, they are approaching more and more the performances of silicon based devices [57].

The working principle of the organic optoelectronics is very similar to the inorganic ones. In both cases, the emission or absorption of light requires an energy gap in the band structure of the device [51,58–62]. The inorganic one ensures that by the PN junction of oppositely doped semiconductor material. The energy levels of the valence and conduction band differ in the p- and n-doted region. The bands in the n-doted region are of lower energy. At the junction, these bands connect forming a slope with decreasing energy from p- towards n-type region which is called depletion zone. If a photon with enough energy $\hbar\omega \geq E_\mathrm{a}$ enters this zone, it is possible that a charge carrier pair (electron and hole) is generated that is separated due to the slope of the respective bands (see Fig. 3.8). Thus, a current is generated which can be measured.

The organic counterpart consists of two compounds that are either blended together (bulk heterojunction) or deposited in two separate layers (discrete heterojunction). One is acting as donor and corresponds to the n-type region of the inorganic semiconductor. The other one, i.e. the p-type, is acting as acceptor. In the case of the OPDs used in this work, the blended active material consists of P3HT:PCBM with P3HT[3] being the p-type and PCBM[4]

---

[3] Poly(3-hexylthiophene-2,5-diyl)

[4] Phenyl-C61-butyric acid methyl ester

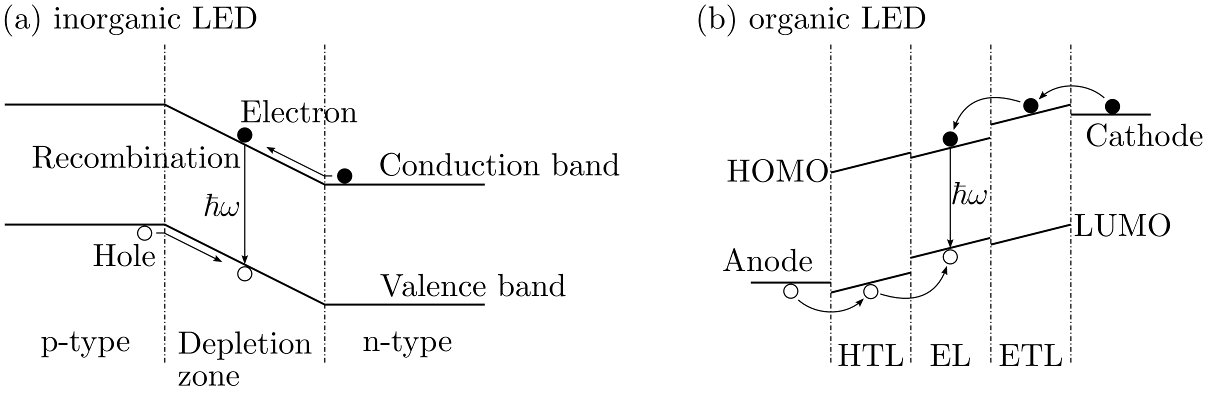

Figure 3.9.: Energy level diagrams of inorganic LED (a) and organic LED (b). The recombination of the electron injected into the electron transport layer (ETL) and the hole injected into the hole transport layer (HTL) in the OLED takes place in the emission layer (EL). Note that the relative energy levels of the electrodes differ from Fig. 3.8, due to the different sign of the bias voltage.

being the n-type compound [63]. To ensure that light reaches this sensitive material, one side of the OPD is usually contacted via transparent electrodes, most commonly made of indium tin oxide (ITO). The opposite electrode is in the present case made of Al.

An LED works so to say in the opposite way (see Fig. 3.9). If the LED is biased in forward direction, the electrons and holes from the n- and p-doped region move into the junction. There they can recombine, converting the released energy into light and heat. The energy E_a available due to one recombination event is given by the band gap of the LED and defines the wavelength of the emitted photon $\hbar\omega = E_\mathrm{a}$. Note that for light emission to happen, the semiconductor has to have a direct band gap, i.e. the energetic minimum of the coduction band lies at the same crystal momentum as the maximum of the valence band. Since the refractive index most of the conventional LED materials is rather high or not translucent, the light generated at the junction is not emitted to a large extent. This inherent draw-back is one of the challenges of LED development.

Due to their thin layer structure, OLEDs do not have this kind of issue. In the simplest form, an OLED can consist of a single layer of organic semiconductor material placed in between two electrodes. The highest occupied molecular orbital (HOMO) and the lowest unoccupied molecular orbital (LUMO) of the material cover the respective roles of valence and conduction band in the LED [59,60]. For a current flowing through the OLED, electrons enter the material at the LUMO. At the opposite side, electrons can only leave from the HOMO. Thus, holes are generated. These holes can now recombine with the electrons in the LUMO allowing for light emission similar to the LED. Nowadays, OLEDs consist of more

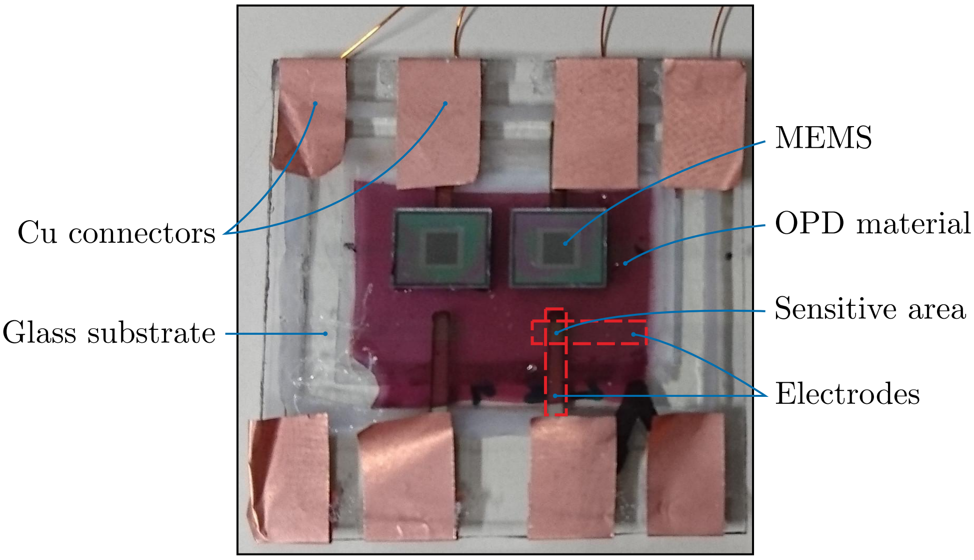

Figure 3.10.: OPD with four electrode pairs used within the scope of this thesis. The overlap of the electrodes (marked by red dashed lines) defines the sensitive area – here 2 × 2 mm^2. The MEMS are glued onto the OPD such that the optical shutter is perfectly aligned with the OPD's sensitive area.

than just one layer in order to increase the charge carrier mobility or quantum efficiency.

The OLEDs used in this work consist of four layers [63]. The first layer that is deposited on the transparent ITO electrode is PEDOT:PSS[5], a transparent polymer with high conductivity connecting the electrode to the active layers. The subsequent layer consists of TCTA[6] which works as hole transport layer. The light emitting layer is made of CBP[7] with 6% Ir(mppa)$_3$[8]. The Ir complex ensures a green colour of the emitted light. Finally, an electron transport layer made of TPBi[9] and an Al electrode are applied on top. It is crucial for the lifetime and yield of these optoelectronics that the encapsulation prevents substances such as oxygen or water to reach the inside of the device. For the tests performed within this thesis, the encapsulation was achieved by glass slides. In future works, other substrates have to be applied to achieve flexibility.

Since the custom made OPDs and OLEDs[10] were produced in a larger size than the conventional optoelectronics, the measurement setup (subsection 2.3.1) had to be modified.

---

[5] Poly(3,4-ethylenedioxythiophene) polystyrene sulfonate

[6] Tris(4-carbazoyl-9-ylphenyl)amine

[7] 4,4'-Bis(N-carbazolyl)-1,1'-biphenyl

[8] Iridium tris[2-(p-tolyl)pyridine]

[9] 2,2',2"-(1,3,5-Benzinetriyl)-tris(1-phenyl-1-H-benzimidazole)

[10] The organic optoelectronics used in this work were kindly provided by the groups of Prof. H.W. Zan and Prof. H.F. Meng of the National Chiao Tung University, Hsinchu, Taiwan.

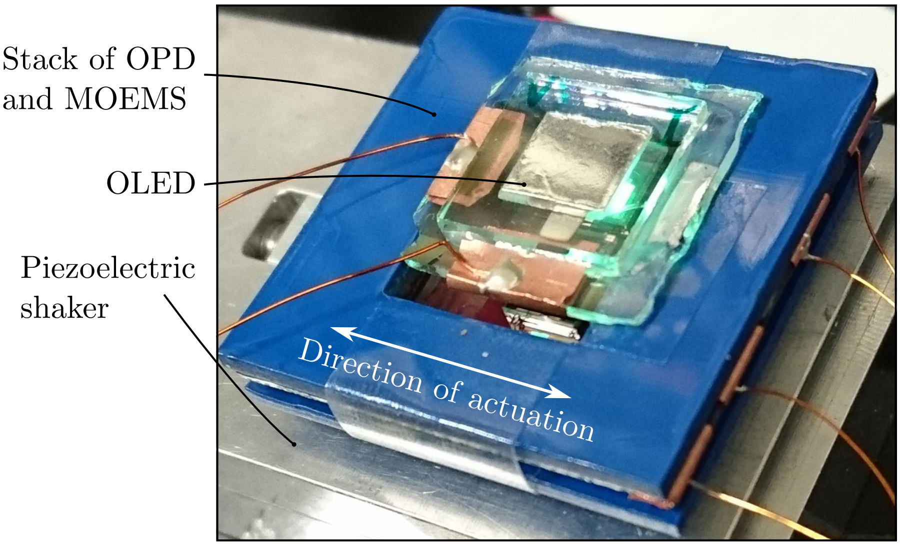

Figure 3.11.: Stack of OPD (bottom – not visible), MEMS (middle – not visible) and OLED (top) fixed on the shaker for characterisation.

Figure 3.10 shows an OPD that was used for testing. The PEEK housing used before is obviously too small to hold the organic optoelectronics. Therefore, the OPD bearing the MEMS were fixed onto a plastic table that was screwed on the shaker. The OLED featured the same active area of 2×2 mm^2 and was placed on top of the OPD/MEMS compound. To avoid contact of the OPD and OLED electrodes, a second plastic slice was placed in between. The complete setup is depicted in Fig. 3.11.

Note that since in order to fix the MEMS structures to the OPD they have to be glued on, the same devices cannot be used on other OPDs. Thus, they were characterised in advance using inorganic optoelectronics. In addition, a measurement was conducted using the OPD/MEMS stack in combination with the conventional LED in order to compare the performances of the individual components. Fig. 3.12 shows an exemplary comparison of all the individual components [64]. Due to the large size of the stack, it was not possible to use the vibrometer as reference. Therefore, the transfer characteristics are plotted in terms of the output voltage of the readout circuit U_{out} and the input voltage for the shaker U_{sh}.

These measurements revealed several issues. The most prominent one was that the performance of the OLED was not satisfying. Another one was that due to the exactly equally spaced active areas of OPD, MEMS and OLED, the alignment across the stack was quite sensitive to lateral displacements. A larger area of OPD and OLED was, therefore, intended for a new batch of devices. A closer inspection of the OLEDs revealed that most of the light was emitted at the edges of one electrode. Since this was not visible with the naked

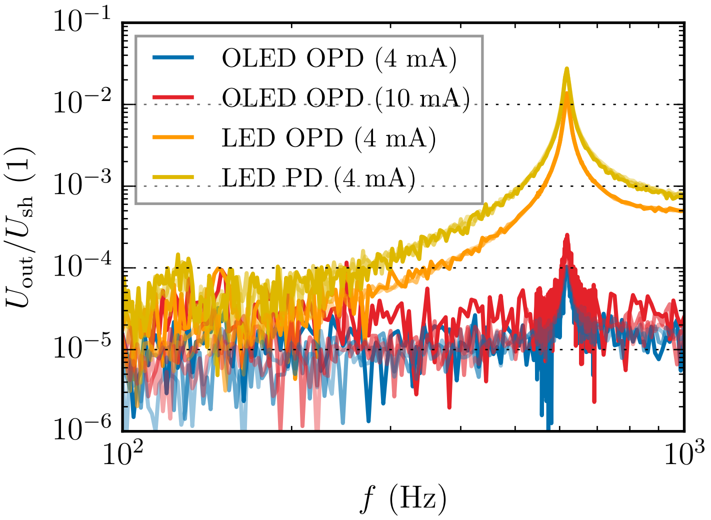

Figure 3.12.: Comparison of the performances of the different combinations of organic and inorganic optoelectronics. While the performance of the OPD was satisfying, there were clearly issues with the OLED. The (O)LED current was set to 4 mA for all measurements except for the one marked red where 10 mA were used.

eye, a neutral density filter (*OD1*) had to be used. Fig. 3.13 shows this *fringing* behaviour. This problem was solved in the successive batch of OLEDs which featured already a larger emitting area of 3×3 mm^2. Additionally, new OPDs with 3×3 mm^2 sensitive area were provided.

Another adaption had to be made to account for using a photodiode instead of a phototransistor which allows much higher currents than the diode. The smaller photocurrents suggested a higher amplification in the readout circuit. This was achieved by using a feedback resistor of $R = 1$ MΩ instead of $R = 10$ kΩ. The higher resistor increased the noise ($\propto \sqrt{R}$) but also the output voltage ($\propto R$). Thus, the signal to noise ratio was improved by a factor of 10.

The characterisation of the new batch of OLEDs and OPDs with the MEMS transducers was performed in the same setup as described above, and within the framework of a master's thesis [65]. The transfer function obtained using the new devices were much more encouraging. The data plotted in Fig. 3.14 shows that the sensitivity using the OLED is equal to the one using the conventional LED.

Furthermore it was observed that the lifetime of the OLEDs was still an issue. The consequences of this issue are portrayed in Fig. 3.15. The recording of one individual

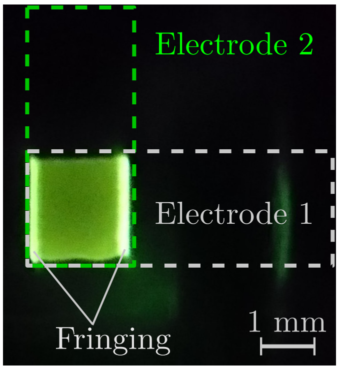

Light distribution of OLED (top view)

Figure 3.13.: Fringing effect due to arched edges of electrode 2.

curve took approximately 50 min. Thus, since the sensitivity was roughly halved after six subsequent measurements, the OLED would stop working after a few days. However, the lifetime of the OLED would significantly increase if the current was reduced. Reducing the current density from the hitherto applied 44.4 mA/cm^2 to 5 mA/cm^2 would increase the lifetime to weeks or even months [66]. This would, however, reduce the sensitivity of the whole stack, too.

Summarising, the use of the organic semiconductors did not deliver the expected increase in sensitivity. However, it was possible to obtain results very similar to those employing the conventional optoelectronics. Since the custom made devices featured in this work were quite rudimentary, it is expected that more advanced integration with the MEMS, e.g. compactification by processing the OLED directly onto the glass wafer and a reflective coating on top, will yield improvements in both sensitivity and efficiency. Also placing the MEMS transducer on flexible substrate bearing OLEDs and OPDs is envisioned.

All in all, the sensitivity and efficiency of the optomechanical part of the transducer can be improved by passive means. Based on the experiments performed within the scope of this section, the most promising approach was to utilize a collimating lens to increase the irradiation on the MEMS. While putting the lens separately onto the MEMS would be error prone and enlarge the device significanly, it is possible to integrate these lenses on the glass wafer on top of the MEMS.

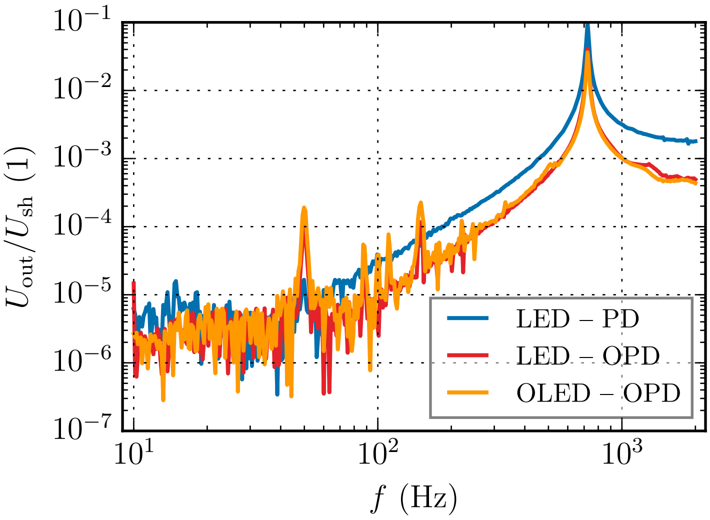

Figure 3.14.: Comparison of the performances of the different combinations of organic and inorganic optoelectronics with the new improved optoelectronic devices. The (O)LED current was set to 4 mA.

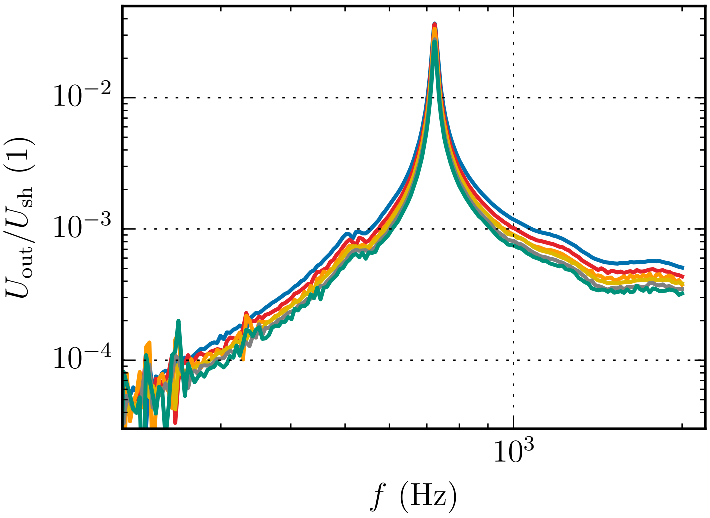

Figure 3.15.: Subsequently recorded transfer characteristics of the OLED/MEMS/OPD stack. The decreasing sensitivity was caused by the decay of the emitting material of the OLED. Starting with the blue line, each recording lasted approximately 50 min.

Chapter 4.

Electric Field Sensing

The measurement of electric fields has always been of great interest for various scientific communities and engineering. For example, meteorologists are interested in the electrostatics of the atmosphere, since the local atmospheric E-field provides information on changing weather conditions[1]. Especially approaching thunderstorms alter the field severely [67] and individual lightning events cause abrupt changes of the field. Apart from these (close-to) ground level weather effects, there is still little known about the electric field inside cloud systems which is partly due to the unpractical circumstances state-of-the-art sensors work [68,69] in. Furthermore, the release of radioactive material into the atmosphere causes a massive drop in the electric field strength at ground level which was observed, e.g., after the nuclear incident in Fukushima [70]. But the atmospheric fields are of interest also on a larger scale in the so-called global atmospheric circuit [71]. In engineering, a reliable electric field sensor poses a valuable safety asset for workers near high-voltage power lines or transformer stations [72].

In this chapter, a unique miniaturised electric field sensor is presented which is intended for low frequency down to DC applications. It is based on the optomechanical readout of the vibration sensor treated in the previous chapters. The underlying principle of transduction of the electric field into a mechanical displacment is described in section 1.3. Due to this way of transduction, the sensor can operate completely passively and without noteworthy perturbation of the electric field to be measured. After a brief introduction to the state-of-the-art sensors, section 4.2 presents basic MEMS layouts which makes the transducer susceptible to an external electric field. In the subsequent sections 4.3 and 4.4, the MEMS fabricated based on these layouts were tested numerically and by measurements.

---

[1] The fair weather electric field strength at ground level lies in the order of 100 V/m. Above ground level this can increase up to 100 kV/m.

Finally, as mechanical vibrations pose a source of disturbance, rotational E-field sensors are presented in section 4.5.

4.1. State-of-the-art Overview

As of today, numerous different methods to measure the electric field have been developed, each having their own advantages and draw-backs with regard to resolution limit, size, temperature stability or field distortion.

Probably the most common sensors are the so-called **field mills** [20, 73] and MEMS field mills [21–23, 25, 74]. They consist of sensing electrodes that are alternatingly exposed to and shielded from the external electric field. For the macroscopic field mills, this is achieved by a rotating grounded electrode. In the case of their MEMS counterparts, the grounded electrode oscillates linearly. The electric field induces a surface charge in the exposed regions of the measurement electrodes which reflects in the output voltage. While the field mill principle can easily be miniaturised and the resolution limit lies in the order of $50\ \mathrm{V/m/\sqrt{Hz}}$, it is evident, however, that the shielding electrode causes a severe distortion of the field. This is taken into account by extensive calibration of the measurement system. Furthermore, the periodic shielding mechanism requires a mechanical actuation which makes the sensing head of the field mill an active part.

Another possible way to measure electric fields are (dipole) **antennae** [75]. They have been used as implantable devices for measuring electric fields in biological tissue [76] or plasma physics [77]. While these antennae feature a very low resolution limit of down to $\sim 0.5\ \mathrm{V/m/\sqrt{Hz}}$, it is clear that the frequency regime is determined by their size. Low frequencies require large antennae, thus miniaturisation is counterproductive.

In space survey [78, 79], **double probes** are used which achieve remarkable resolutions of about $10^{-7}\ \mathrm{V/m/\sqrt{Hz}}$. These probes, however, are designed for diluted plasma environments and require well-defined probe electrodes and several metres distance between the probes. Furthermore, it is necessary to separate the probes with actively shielded booms which hardly distort the electric field to be measured.

A quite elegant approach to E-field sensing is exploiting the **electrooptic effects**, due to which optical properties change with respect to an electric field. Especially noteworthy is, thereby, the dependence of the refractive index $n = n(E) = \sum_{i=0}^{\infty} c_i E^i$ on the E-field. The most prominent effects thereof are the Pockels and the Kerr effect. The Pockels or linear electro-optic effect ($i = 1$) is, in general, the strongest one. It depends linearly on E and can also be used to measure low-frequency or static fields [80–82]. The Kerr effect ($i = 2$) is the quadratic electro-optic effect. It is usually much weaker than its linear counterpart, but is practical for strong electric fields [83, 84]. These sensors, however, have in common that they are extremely prone to temperature changes. As of now there is no electro-optic sensor that has solved this issue, even though a resolution limit as low as 0.6 $\mathrm{V/m/\sqrt{Hz}}$ can be achieved [85].

4.2. Basic E-field Sensor Layout

The electromechanical transduction of the electric field introduced in section 1.3 poses a novel concept for MEMS electric field sensors. In order to translate the effect of electrostatic induction into a measurable mechanical displacement (Fig. 1.4), the layout of the vibration sensor has to be adapted. The closed Si frame of the vibration sensor effectively shields the inertial mass from the electric field, thus perventing the electrostatic force F_{es} from deflecting it. Therefore, the frame has to be interrupted. Two possible ways to achieve that are depicted in Fig. 4.1.

These two configurations basically differ by a second stationary Si part as seen in the semi-covered case. The bare structure poses the straightforward implementation of the transduction principle and is probably the most simple one. It is, however, also not practical, since the MEMS is then much more fragile. Furthermore, the fabrication process is much more complicated which is due to the massive water inflow during the dicing step with a wafer saw (see appendix A). The additional Si part helps to control these issues. It causes not only an increase in stability and a reduction of the water inflow, but also affects the strength of the electro-mechanical transduction. Since the external field separates the charges in both of the domains, there will develop inversely charged surfaces opposing each other inside the gap. The closer these surfaces are, the larger the electric field and, hence, the force between them (see Fig. 4.5b). Furthermore, given an appropriate shape, this Si part can act as a field concentrator, increasing the charge opposite of the moving mass even further. Obviously, water inflow during dicing is still an issue for this configuration, though not as severe as for the bare structure. Thus, this approach was taken to be superior and the other one was not further pursued.

As was shown in preliminary FEM simulations, the electrostatic force is maximised by increasing the edge length along which the surface charge should develop [86]. Thus, the width w of the moving mass needs to be large. Additionally, the mechanical system should

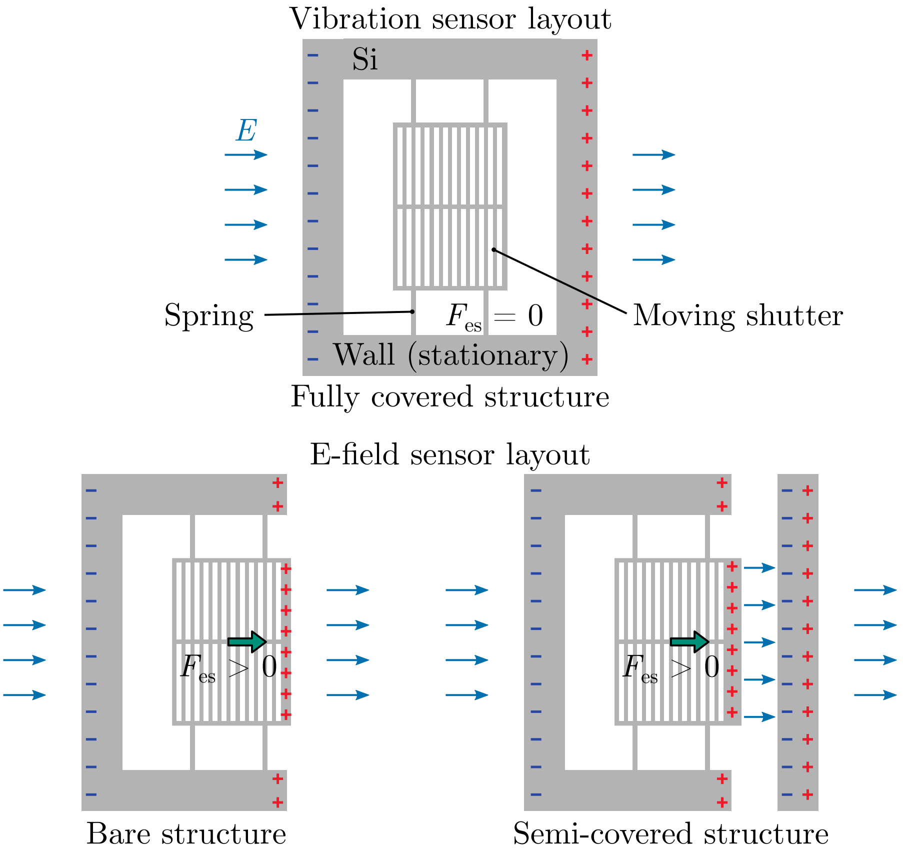

Figure 4.1.: Intended layouts of the optomechanical E-field sensor. The top schematic is not sensitive to electric fields due to the shielding of the Si wall. If the shielding is interrupted as in the bottom configurations the MEMS can act as transducer for electric fields.

not be too stiff in order to achieve detectable deflections. Thus, the beams comprising the springs need to be long enough. In the conventional vibration sensor design, as in Fig. 1.1, these two requirements are mutually inhibitive. Furthermore, the largest part of the surface charges would develop on the springs and their anchor points, which affects the electromechanic transduction in a negative way. The solution was to relocate the springs to a *pocket* inside of the mass.

Fig. 4.2 shows a prototype layout of such a MEMS electric-field sensor. The springs were moved *inside* the mass. Furthermore, the stationary Si part on the right acts as a field concentrator which is ensured by choosing the gap towards the moving mass smaller than the one towards the other stationary frame. Note that these two domains are not separated until the dicing step in which the egdes of the chip are removed as far as to the saw markers. The corresponding handle layer geometry (Fig. 4.2 bottom left) also has to feature two

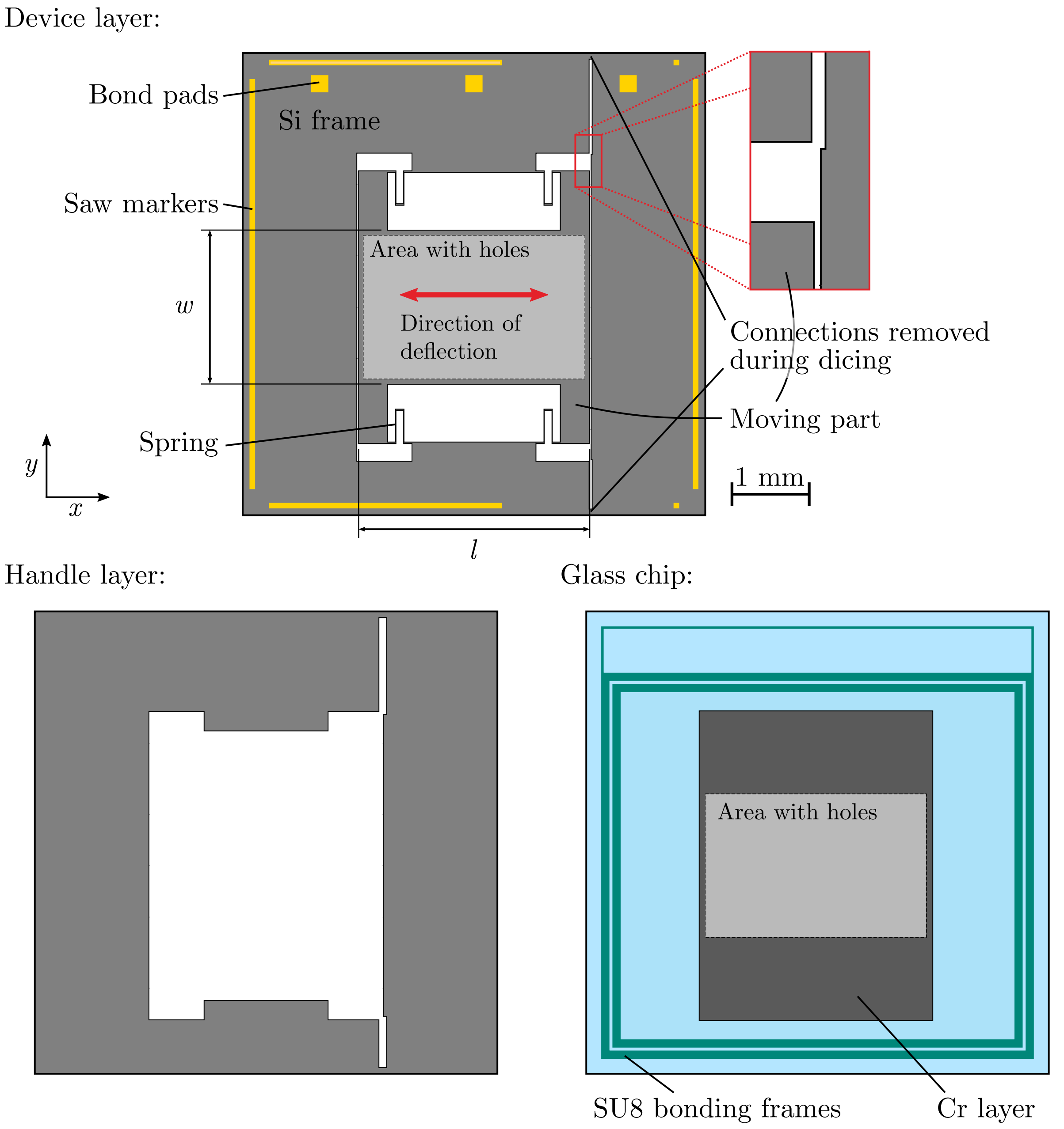

Device layer:

Handle layer:

Glass chip:

Figure 4.2.: Exemplatory prototype layout of an E-field sensor. The device layer of the SOI chip contains the moving part of the optical shutter. The springs are now located inside of a *pocket* in the moving mass to increase the electrostatic force. The gap between the mass and the Si wall is 20 µm wide in this design. The gap between the immobile Si regions is wider in order to concentrate the charges at and opposite of the mass.

separated Si domains. Otherwise, the handle layer would act as shielding and significantly diminish the electrostatic force exerted on the moving mass. The stationary part of the optical shutter is again made by depositing Cr onto glass. Since Cr is a conductor as well, care must be taken that the Cr does not reach over the gap. This, too, would affect the force acting onto the moving mass. Both of these effects have been studied by FEM analyses in [86].

Additionally, there are bond pads located at the top side of the device layer. These fulfill two purposes. First, they allow for self testing which, in this case, means measuring the electrical resistance, e.g., by microprobing. If there is any conducting connection between the left and right domain of the chip, the Si frame shields the moving shutter from the field similar to the top of Fig. 4.1. These unwanted connections might arise during the sawing process, if Si particles accumulate inside the gaps or if the mass sticks to the opposing Si frame. Second, the chips can be wire-bonded onto a PCB substrate and actuated by applying a voltage. This can be useful if one wants to test the behaviour of the MEMS independent from the shaker system. Furthermore, it can be used as MEMS voltage sensor with optical read-out.

Note that the problematic water inflow during dicing had to be accepted within the scope of this thesis, since there were no other dicing methods available at the time. Some sophisiticated channels have been tried out to avoid the inflow but without success [86].

4.3. Numerical Analyses of the Sensor

In order to get an impression of the behaviour of the MEMS layout introduced in the previous section, the lowest eigenmodes, their shapes and the response of the movable shutter to mechanical and electrostatic excitation are analysed numerically. For this purpose, FEM simulations with Comsol Multiphysics were performed on the representative geometry of the device layer in Fig. 4.2 yielding the qualitative behaviour.

First, the eigenfrequencies and the corresponding mode shapes were determined. The plane geometry was extruded to 50 µm which matches the thickness of the device layer of the SOI wafer used for fabrication. Apart from the wanted mode that comprises the linear deflection in x-direction, also other modes arise, e.g. torsional modes or deflections in y or z. Fig. 4.3 shows the mode shapes of the lowest four modes obtained by the FEM calculation. The measurement regime for this structure is bounded from above by the fundamental frequency f_0 which, in reality, is lower than the value resulting from the FEM simulations.

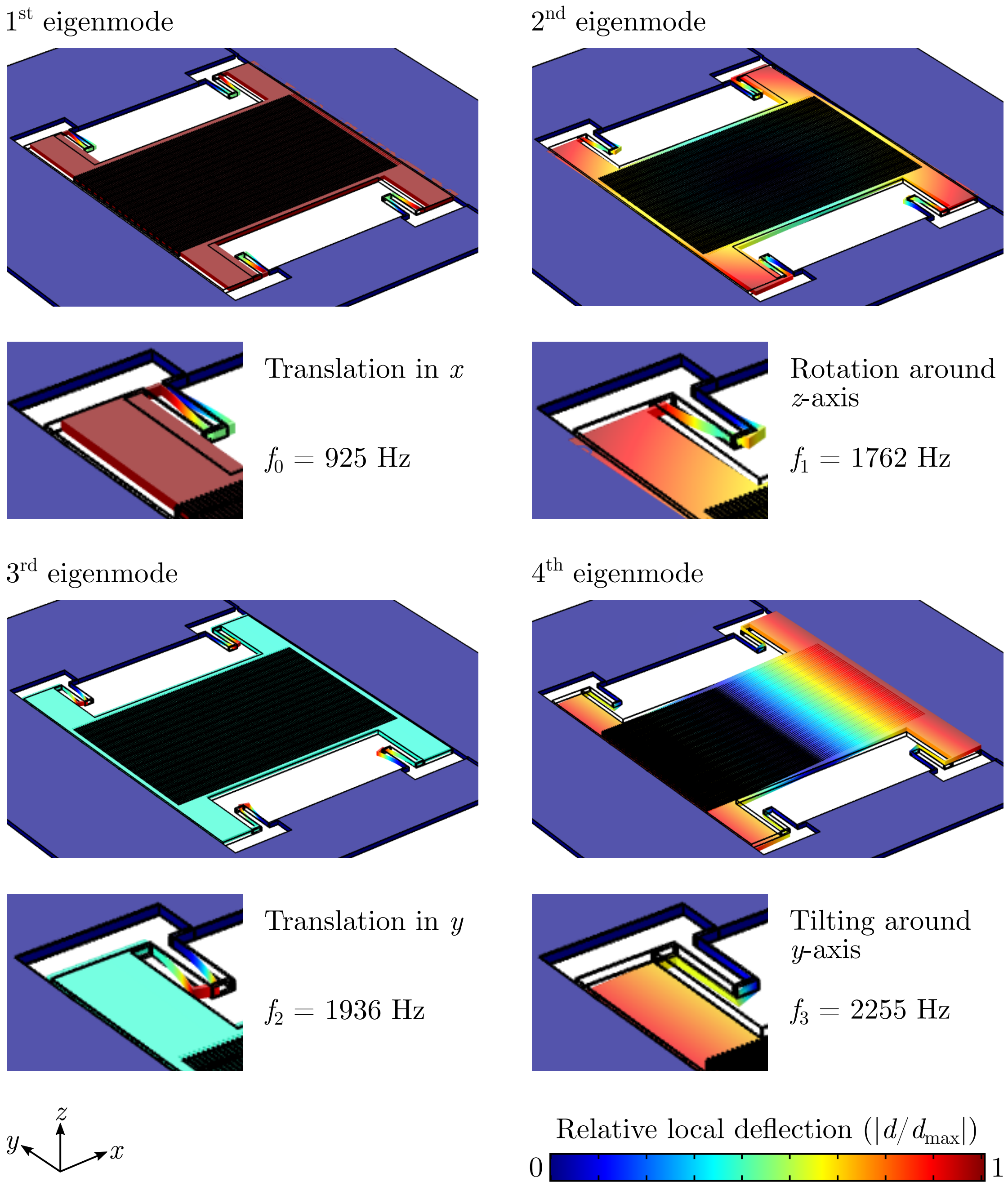

Figure 4.3.: Mode shapes of the first four eigenmodes of the MEMS electric field sensor. The fundamental mode with calculated frequency $f_0 = 925$ Hz corresponds to the wanted deflection of the shutter in x-direction. The other depicted modes are the in-plane rotation, deflection in y-direction and tilting around the y-axis. Due to the known properties of the fabrication process, the fundamental eigenfrequency of the actual MEMS is lower and also the other modes will shift.

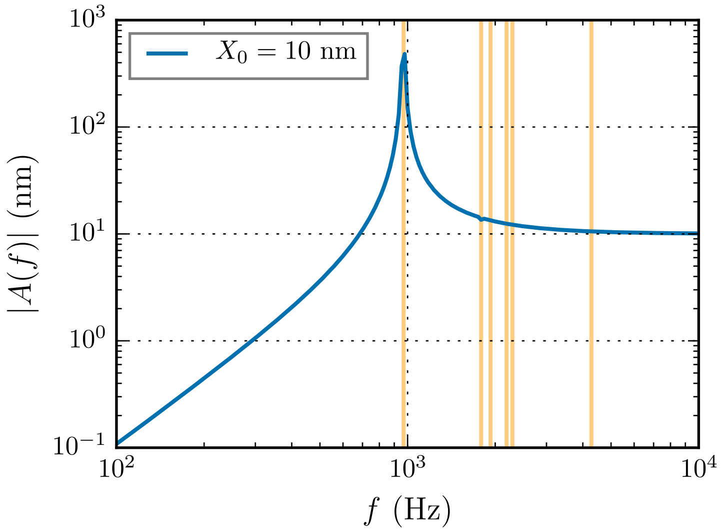

Figure 4.4.: FVM results of the frequency response of the E-field sensor to an input displacement of $X_0 = 10$ nm in x-direction in terms of the total displacement magnitude of the inertial mass. The vertical orange lines correspond to the individual modes. Apart from the small dent due to the second eigenmode, only the fundamental mode is excited.

This results from the etching process (compare subsection 2.3.2). The higher modes are not of interest, since they lie out of the measurement regime.

In a second step, the frequency response of the moving mass with respect to a mechanical excitation was calculated in order to have a comparison with the known system of the vibration sensor. Note that this structure can also be applied as vibration sensor or accelerometer. The simulation was performed with a prescribed displacement of $X_0 = 10$ nm in x-direction applied to the edges of the frame for frequencies ranging from 100 Hz up to 10 kHz. The resulting response depicted in Fig. 4.4 reveals a nice high-pass characteristic as described in Eq. (1.3) and Fig. 1.3b converging to the excitation amplitude of 10 nm towards $f \gg f_0$. The value for the damping and, hence, the height of the resonance peak in this plot are arbitrary, since only the solid mechanic part was subject of the simulation.

The next step was to determine the electrostatic force acting onto the moving shutter. Therefore, the MEMS was placed inside a cube of air with $a_c = 1.9$ cm edge length [2] in which a uniform electric field in x-direction was established. This field was determined by the respective potential of the opposite side faces of the air cube. The potential of the left

---

[2] This length corresponds to the actual distance of the capacitor plates uses in the measurement setup (see subsection 4.4.2).

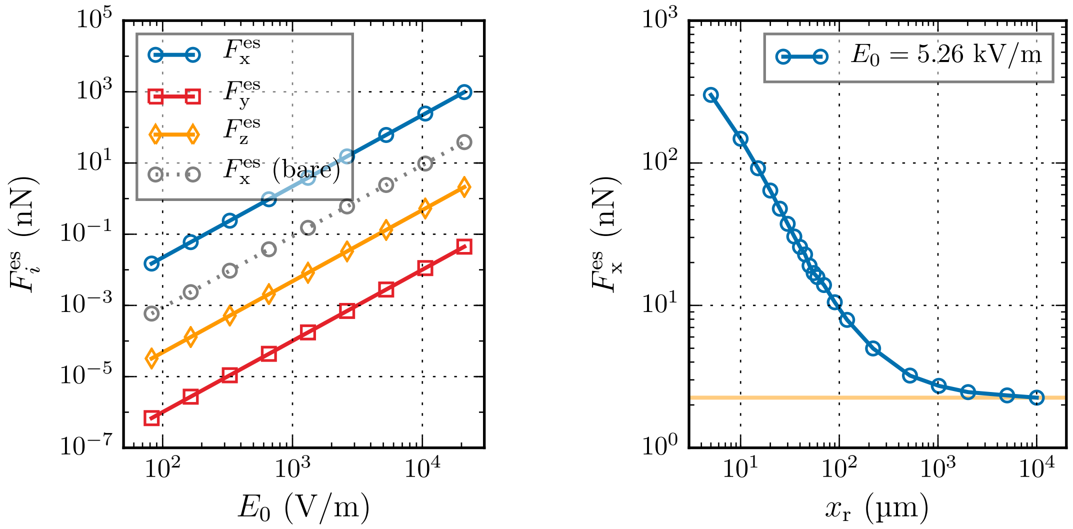

(a)

(b)

Figure 4.5.: (a) Electrostatic force components F_i^{es} acting on the moving part of the MEMS obtained by FVM simulations for a uniform external E-field in x-direction. It can be seen that the force increases quadratically with the electric field $F_i^{\mathrm{es}} \propto E^2$. It can also be seen that the force $F_{\mathrm{x}}^{\mathrm{es}}$ of the bare structure is much smaller as the one with opposing Si wall. This can be seen in more detail in (b) where the distance x_{r} between moving mass and *field concentrator* is varied. The force $F_{\mathrm{x}}^{\mathrm{es}}$ is proportional to x_{r}^{-1} and converges to the force of the bare structure (bottom orange line).

side face was set to 0 V, while the other one was halved eight times starting from 400 V to 1.5625 V. This corresponds to electric fields ranging from roughly 21 kV/m to 82 V/m. The Si structure was treated as ideal conductor which was taken into account by applying a Floating Potential boundary condition to the Si domain.

The resulting force components are plotted in Fig. 4.5a. As argued in the analytical calculation in section 1.3, the force is proportional to the square of the electric field $F_i^{\mathrm{es}} \propto E^2$. Furthermore, due to the low symmetry of the geometry, there occur non-zero components orthogonal to the external field $\mathbf{E} = E\,\mathbf{e}_{\mathrm{x}}$ which was also noted in sec. 1.3. These are, however, much smaller than the wanted x-component and can safely be omitted. Additionally, the layout was compared to the corresponding bare structure of which the moving mass is directly exposed to the electric field. This revealed that the force $F_{\mathrm{x}}^{\mathrm{es}}$ of the bare structure is over an order of magnitude smaller than the force of the semi-covered one. Note that the gap x_{r} width significantly influences the strength of the force. This

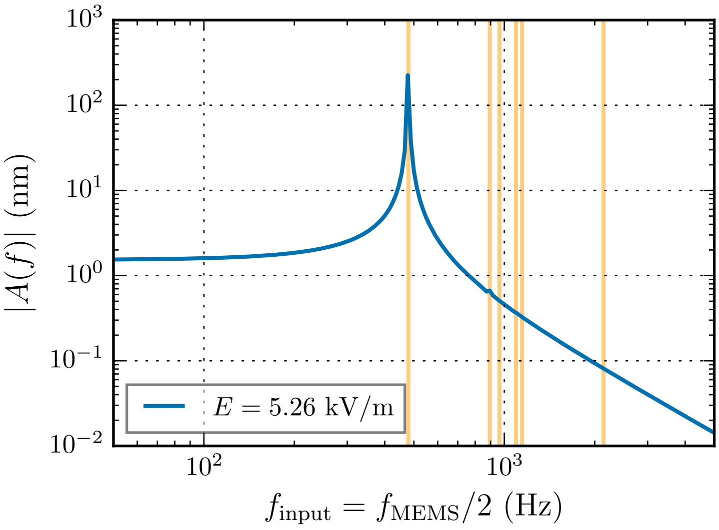

Figure 4.6.: FVM results of the frequency response of the sensor to an input electric field of $E = 5.26$ kV/m in x-direction. As in Fig. 4.4, the vertical orange lines correspond to the individual modes. Only this time they arise at half their original frequency, since the force is quadratic $F \propto (E \sin \omega_{\text{input}} t)^2 = E^2(1 - \cos 2\omega_{\text{input}} t)/2$. Again, only the fundamental mode is excited, apart from small dent due to the torsional mode.

was investigated in more detail in an additional FEM analysis comprising a parametric sweep of $x_{\text{r}} \in [5, 10^4]$ µm. For these simulations, the non-zero potential was set to 100 V which corresponds to an electric field of $E_0 = 5.26$ kV/m inside the air cube. The results are plotted in Fig. 4.5b. It can be seen that for small gap widths $x_{\text{r}} \lesssim 200$ µm F_{x}^{es} decreases linearly with x_{r} and for larger gap widths converges to the bare structure configuration. Thus, the force of the bare structure poses the minimum electrostatic force. Note that the value for the force of the bare structure was taken from the simulation with the largest gap, since there the field concentrator lies outside of the domain of the E-field.

Finally, the three components of $\mathbf{F}_{\text{es}}$ were used as input force on the movable part in a frequency domain analysis to study the response of the MEMS to the electric field. The resulting amplitude function is plotted in Fig. 4.6. In contrast to the mechanical actuation treated above, the response of the force excited system exhibits a low-pass behaviour. Furthermore, since the force depends quadratically on the electric field $F \propto (E \sin \omega_{\text{input}} t)^2 = E^2(1 - \cos 2\omega_{\text{input}} t)/2$ (see sec. 1.3), the resonance peak is visible at half the corresponding input frequency. Therefore, if the external E-field oscillates at half the resonance frequency of the MEMS $f_0/2$, the MEMS oscillates at f_0.

4.4. Prototypes and Measurements

4.4.1. Prototype layouts

Based on these calculations, several prototype layouts were designed which can be divided into two groups. The first one entailed the more stable configuration and consisted of only one layout with smaller mass m, higher stiffness k and wider gap x_r. It will be referred to in this chapter as *stable group*. The dimensions of the mass of the stable group was $l = 3$ mm and $w = 2$ mm as defined in Fig. 4.2. The gap was set to $x_\mathrm{r} = 20$ µm and the stiffness to $k = 4$ N/m. No parameter variations were implemented in this group. This was the safety option, since the dicing step was expected to be accompanied by a large number of losses.

The second group which will be referred to as *test group* contained variations of spring stiffness, and gap width. The dimensions of the moving part was chosen to be larger than the ones of the stable group, i.e. $l = 3$ mm and $w = 2.5$ mm. Two different spring stiffnesses of 1 N/m and 2 N/m and two gap widths of 10 µm and 20 µm were implemented, resulting in four different layouts named *ChXX*. The Xs can each be 0 or 1 with the first X corresponding to the two possible stiffnesses (1 N/m and 2 N/m, respectively) and the second X to the gap widths (10 µm and 20 µm, respectively). Therefore, the Ch00 layout is expected to feature the highest sensitivity while the Ch11 layout is the most robust one. The relatively small gaps correlate with a quite strong damping and, thus, low quality factor as described in sec. 2.2.2. This is, however, hardly a problem, since the MEMS device is not intended for resonant sensing.

Ten copies of each layout were placed onto the wafer to account for possible losses during the problematic fabrication and investigate reproducibility. In total, fifty MEMS electric field sensor prototypes will be fabricated for testing in both a mechanical setup as introduced in subsec. 2.3.1 and in the E-field setup described below.

4.4.2. E-field Characterisation Setup

The electric field which was used as well-defined input for the MEMS sensor was provided by customised Al parallel capacitor plates of 2.7×2.7 cm^2 area. They were separated by a distance of 1.9 cm. The electrical field produced by these plates can be assumed to be uniform in the space between. The MEMS chip was placed in the centre of this uniform field. Originally, it was intended to be clamped in a plastic chip holder[3] which was held by

---

[3] 3D printed in material Verowhiteplus.

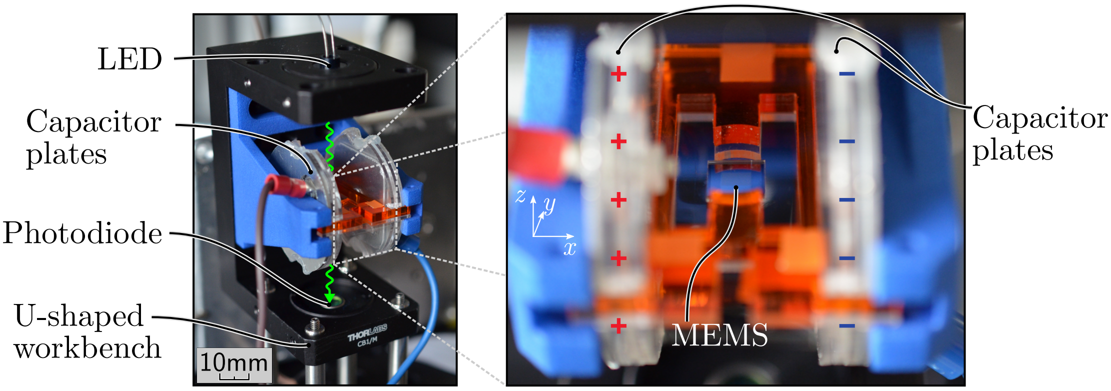

Figure 4.7.: Electric field measurement setup.

an acrylic structure. Despite being an insulator, the material, however, effected a finite parasitic resistivity across the gap in the range of 50 GΩ (see appendix C). This impaired successful E-field measurements. Thus, the chip holders were replaced by adhesive tape held by the acrylic structure. These materials, as dielectrics, do not perturb the electric field significantly. This setup was mounted on a Thorlabs U-bench CB1/M which was set to ground potential (see Fig. 4.7).

In order to provide sufficiently high electric field strengths, a high voltage wideband amplifier (Tabor Electronics 9200A) had been used. It amplifided the amplitude of the sinusoidal voltage output from the waveform generator by a fixed factor of 50 to a maximum of 400 V.

The optoelectronics used in this E-field measurement setup had to be placed outside of the field region in order to avoid cross-talk of the electric field to the optical components and distorting the E-field. This was achieved by placing them into the grounded U-bench. This, however, changed the requirements for the LED, since the distance between light source and detector here was much larger than in the mechanical setup. For efficient use of the emitted light, a well collimated LED was necessary. Therefore, a Thorlabs LED528EHP (λ_{peak} = 525 nm) was chosen which features a very small half angle of 9°. As detector, a large area (3.8×3.8 mm^2) Si photodiode Centronic OSD15-5T was used of which the TO-5 housing improved the shielding. The electronic readout circuit was the same as in subsec. 3.2.3 with a transimpedance resistor of 1 MΩ. The output of the readout circuit was then recorded with a Stanford SR830 lock-in amplifier set to the second harmonic of the waveform generator's sync frequency. Both the waveform generator and the lock-in amplifier were controlled via a Python script (see Fig. 4.8).

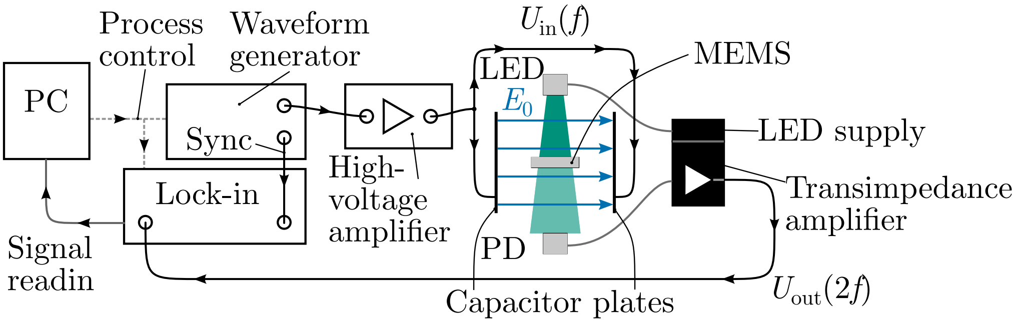

Figure 4.8.: Block diagram of the setup for the electric field measurement.

	ω_0 (1/s)	γ (1/s)	Q (1)	amount working
stable	3845 ± 167.9	31.4 ± 7.59	61.23	5/10
Ch11	2572 ± 193.0	30.3 ± 0.76	42.51	4/10
Ch01	1891 ± 61.5	31.2 ± 2.25	30.31	4/10
Ch10	2663 ± 103.0	74.4 ± 4.02	17.89	5/10
Ch00	1823 ± 33.4	84.0 ± 35.7	10.85	4/10

Table 4.1.: Mechanical parameters of the E-field sensor layouts.

4.4.3. Electric Field Measurements

Before the E-field measurement, the mechanical properties, i.e. ω_0 and γ, of the two groups of MEMS chips were determined in the mechanical vibration sensor setup (subsec. 2.3.1). Only this time, a green LED (Osram LT-673-N2S1-35) and a Si photodiode (Vishay TEMD5510FX01) were used instead of the IR LED and the phototransistor in order to match the E-field setup more closely in terms of applied wavelength. The feedback resistor was, therefore, set to $R_{\mathrm{fb}} = 1\ \mathrm{M\Omega}$. The results for the mechanical properties are listed in Table 4.1. Each device of the five different layout groups was tested in this setup. The fundamental frequencies ω_0 agreed well within each group. Also the decay parameters γ were in agreement with analytical models, even though the variance, especially of group Ch00, is quite high. The damping parameter $d = \mathrm{Re}\, F_{\mathrm{tot}}/v_{\mathrm{str}}$ obtained according to Eq. (2.26) yielded a value of $d = 91.2$ mg/s for the Ch0X layouts and $d = 25.96$ mg/s for the Ch1X layouts. With a calculated inertial mass of roughly $m = 0.64$ mg, this amounts to decay parameters of $\gamma = 70.95\ \mathrm{s}^{-1}$ and $\gamma = 20.2\ \mathrm{s}^{-1}$, respectively[4]. In total, roughly 44% of the MEMS were working and ready for E-field measurement, which was a fair yield for a new device.

---

[4] The value for the Ch1X structures slightly deviates from the measurement, since for this value of $x_{\mathrm{r}} = 20$ µm, the model is less accurate.

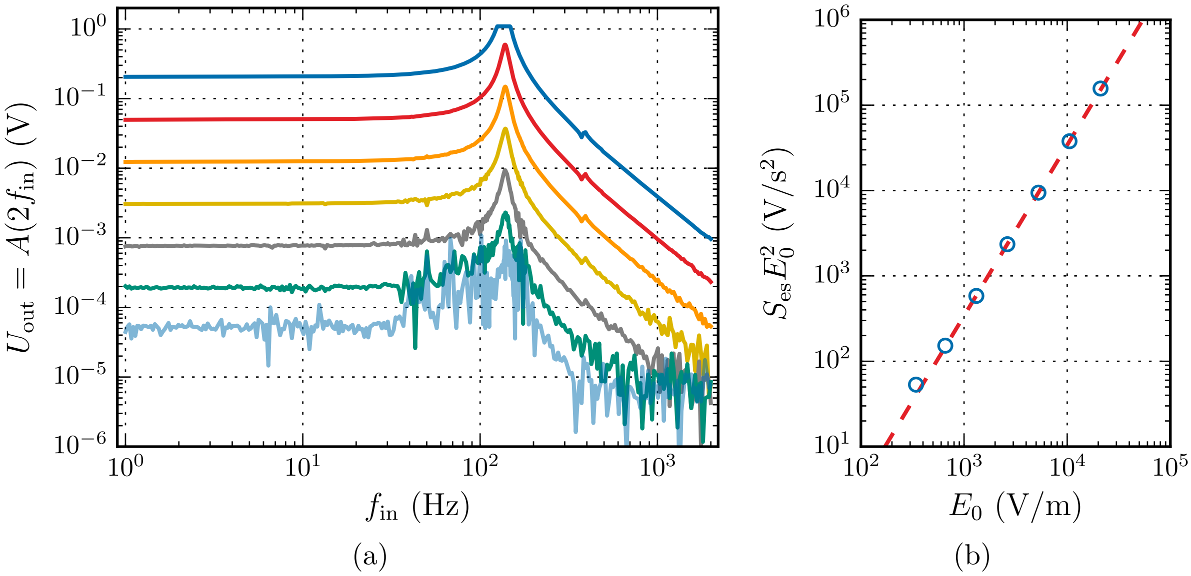

Figure 4.9.: (a) Exemplary response of a MEMS sensor (group Ch00) to the input electric field with amplitudes doubled six times from 342 V/m to 21.05 kV/m. The quadratic transduction of the E-field effects that the doubling steps of the input voltage quadruples the output voltage and that the resonance frequency is observed at $f_{\mathrm{in}} = f_0/2$, here at 139.2 Hz instead of 292.6 Hz. The noisy region from 40-100 Hz reflects the acoustic influence of the ventilation system in the lab. The cutoff at the resonance of the top curve is due to the maxed output voltage range of the lock-in. (b) Strength of the response $S_{\mathrm{es}}\,E_0^2$ as function of the electric field amplitude E_0. The circles correspond to the curves in (a) and the red dashed line to the function $f(E_0) = S_{\mathrm{es}}\,E_0^2$ with the mean value of $S_{\mathrm{es}} = 3.6 \cdot 10^{-4}$ Vs^{-2}/(V/m)^2 obtained from the least-squares fits of the data plotted in (a).

Each of the transducers successfully characterised mechanically was tested in the E-field setup (subsec. 4.4.2). This was done by providing several input voltages ranging from 400 V down to 6.5 V in an input frequency range from 1 Hz to 2 kHz. Exemplary results for the frequency response of one test structure of group Ch00 are shown in Fig. 4.9a. The quadratic behaviour of the transduction can be seen more clearly in Fig. 4.9b. There, each curve has been fit to the mechanical response of the sensor Eq. (1.10) extracting the values of the electromechanic sensitivity S_{es}.

The noise floor of this configuration of roughly 10 µV is determined by the electronic (Johnson) noise of the transimpedance resistor. Considering the quadratic nature of the transduction, this is equivalent to an electric field of roughly *NEF* ≈ 153 V/m. The resolution limit follows from this noise equivalent by relating it to the equivalent noise bandwidth,

	ω_0 (1/s)	S_{es} (µVs^{-2}/(V/m)^2)	r_{es} (V/m/$\sqrt{\mathrm{Hz}}$)	amount working
stable	3845 ± 167.9	96.7 ± 28.5	699 ± 128	5/10
Ch11	2572 ± 193.0	146 ± 32	399 ± 60	4/10
Ch01	1891 ± 61.5	268 ± 82	272 ± 68	4/10
Ch10	2663 ± 103.0	131 ± 38	294 ± 89	5/10
Ch00	1823 ± 33.4	234 ± 101	221 ± 69	4/10

Table 4.2.: Sensitivity and resolution limit of the E-field sensor layouts.

i.e. $r_{\mathrm{es}} = NEF/\sqrt{ENBW}$. With an equivalent noise bandwidth of $ENBW = 0.78$ Hz of the lock-in amplifier at an off-resonance measurement frequency of 100 Hz this yields a resolution of $r_{\mathrm{es}} = 173$ V/m/$\sqrt{\mathrm{Hz}}$.

Translating the observed noise floor of 10 µV to an equivalent displacement of $NED \approx 8$ pm was done by mechanically exciting the MEMS in the E-field setup such that the (sinusoidal) output voltage becomes clipped on both sides. This yielded a peak-to-peak voltage of 12.5 V which corresponds to a displacement of 10 µm, i.e. the width of the holes. Note that this was only a rough estimation. The fundamental limit of the sensor is determined by the Brownian noise which can be estimated by the mean noise force $F_{\mathrm{th}} = \sqrt{4k_{\mathrm{B}}T\,d}$, where $k_{\mathrm{B}}, T, d = 2m\gamma$ are the Boltzmann constant, the temperature and the damping coefficent, respectively. Therefore, the equivalent displacement evaluates to $\delta x_{\mathrm{th}} = \sqrt{4k_{\mathrm{B}}T/m\omega_0^3 Q}$ yielding $\delta x_{\mathrm{th}} = 0.56$ pm with a motional mass of $m = 6.43 \cdot 10^{-7}$ kg. Given a perfect readout circuit, this corresponds to a theoretical resolution limit of 40.55 V/m/$\sqrt{\mathrm{Hz}}$.

The results of the electromechanic sensitivity S_{es} for all layout groups are listed in table 4.2. The values of S_{es} incorporate only the electrostatic force and the intrinsic sensitivity of the device and are, therefore, independent of the mechanical properties, i.e. ω_0 and γ. Thus, groups Ch011 and Ch011 which differ only by their stiffness or ω_0 are equivalent with respect to S_{es}. They have the same gap $x_{\mathrm{r}} = 20$ µm determining F_{es} and the same optomechanic sensitivity S. Combining these groups, one finds $S_{\mathrm{es,ChX1}} = (1.39 \pm 0.36) \cdot 10^{-4}$ Vs^{-2}/(V/m)^2. The same is true for Ch10 and Ch00 with the same sensitivity S but different $x_{\mathrm{r}} = 10$ µm yielding $S_{\mathrm{es,ChX0}} = (2.68 \pm 0.94) \cdot 10^{-4}$Vs^{-2}/(V/m)^2. This is about twice the value of the ChX1 layouts which agrees well with the $1/x_{\mathrm{r}}$ behaviour of the electrostatic force investigated in the FEM simulations.

The relatively large variances are mainly due to the manual positioning of the MEMS in the setup which has a great impact on the light path through the chip. This issue is expected to be accounted for in future devices with optical fibre connections.

4.5. Rotational E-field Sensors

Obviously, the devices presented in the previous section are not only sensitive to electric fields, but also to mechanical interferences such as vibrations or acoustics (see Fig. 4.9a). Therefore, a new generation of MEMS was designed such that these interferences are diminished. This was attempted by employing MEMS which move by rotation instead of translation. Here, the E-field causes a torque which displaces the inertial mass, while, ideally, vibrations do not couple at all into the system since translational displacement of the mass is inhibited by the design.

4.5.1. Layouts

In oder to achive rotational MEMS devices which are susceptible to electric fields and at the same time comprise an optical shutter for the readout, both the mass and the suspension had to be modified while keeping in mind the galvanic separation in the Si frame. The favoured in-plane rotations can be achieved by springs which are evenly distributed around the moving mass and radially oriented around its centre of rotation. For the E-field structures, however, this is not easily possible, if the number of individual springs is larger than two, which is necessary for stability. The inertial mass can only be connected to one part of the Si frame. Furthermore, the mass has to be balanced to sufficiently suppress unwanted modes. Figure 4.10 shows two exemplary layouts for such rotational E-field sensors.

In these first layouts, the suspension consists of three springs which are not evenly distributed. This was necessary to avoid the connection to the right part of the Si wall. However, this also leads to an asymmetric behaviour. Vibrations in x-direction are expected to play no role, while, due to this asymmetry, vibrations in y- and z-direction are expected to cause an unwanted displacement of the mass. Furthermore, two different shapes of springs were implemented. The straight beam springs are stiffer but supposedly more resilient to vibrations, while the U-shaped springs are softer but offer less protection against vibrations. The beams of both types of springs were designed with a width of 4 µm, which means that the (rotational) stiffness is set only by the beams' length.

The optical shutter also had to be adapted to the rotational motion of the mass, since for an unchanged configuration, the change in light flux would be zero. This is due to the fact that the holes on the top half of the moving mass would, e.g., open up, but at the same time the holes on the bottom half would close at the same rate. Therefore, the Cr mask

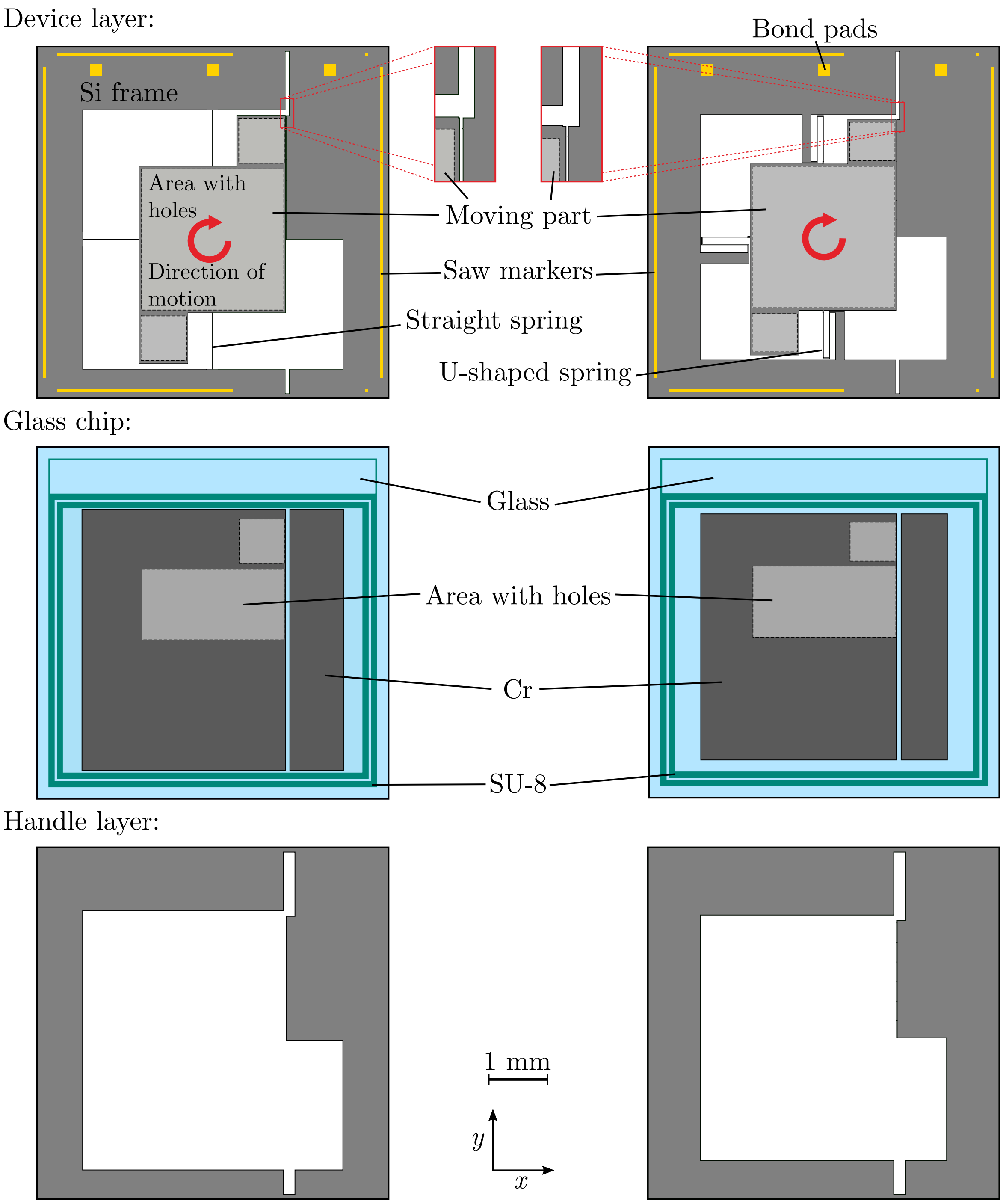

Figure 4.10.: Prototype layouts of rotational E-field sensors. The mass is now suspended onto three springs (left: straight springs, right U-shaped springs) which are now radially connecting to the Si wall. The sensing gap is located only in the top half in order to achieve a torque. Only the holes on the top half contribute to the readout (see glass chip). The holes in the bottom half of the Si mass are necessary for balancing.

was designed with holes only at the top half. The Si mask, however, featured holes on both halves to improve balancing.

For the electric field to generate a torque which actuates the moving mass, the sensing gap also had to be asymmetric. Therefore, only the top half of the gap was narrow, here 10 or 20 µm. The bottom half was made much wider (> 500 µm) in order to inhibit any attractive electrostatic force effect. This, of course, reduces the sensitivity of the sensor. To counteract this, the inertial mass was widened towards the upper end of the chip prolonging the sensing gap. For the sake of balancing, the same addition was made at the lower left corner of the mass.

4.5.2. FEM analyses

Just as for the translational E-field sensor, also the designs for the rotational ones were studied with FEM simulations. First, the mechanical behaviour of these two geometries was studied in the same way as before. The mode shapes and corresponding eigenfrequencies are depicted in Fig. 4.11 for the straight shaped springs and in Fig. 4.12 for the U-shaped ones.

The different shapes of the springs naturally lead to different eigenmodes of the structures. while the fundamental mode of both layouts lies roughly at the same frequency $f_0 \approx 950$ Hz, the respective subsequent mode demonstrates the difference. The second mode of the straight spring structure lies at 4217 Hz and corresponds to a tilting motion. No translational eigenmodes, to which vibrations couple easily, arise at frequencies below 40 kHz. This is in contrast to the U-shaped suspension. There, the second eigenmode is located only ~ 200 Hz above the wanted fundamental mode.

Subsequently, the frequency response to an input vibration amplitude of 10 nm of the two layouts was investigated. This vibration was prescribed first in x-direction and then in y-direction, while observing the displacement of the mass only in x-direction. The results thereof are plotted in Fig. 4.13. What was already indicated in the eigenfrequency analysis, can now be seen more clearly. The straight beam structure is more resistant against the mechanic interferences. This reflects, first of all, in the amplitude of the response function $A(f)$ which is several orders of magnitude lower than for the structure with U-saped beams. Additionally, only the fundamental (rotational) mode is excited. Due to the asymmetric suspension, this is significant only for the vibration in y-direction and even there, the amplitude is relatively small.

As for the U-shaped springs, the amlitude of the response is quite large, comparable with

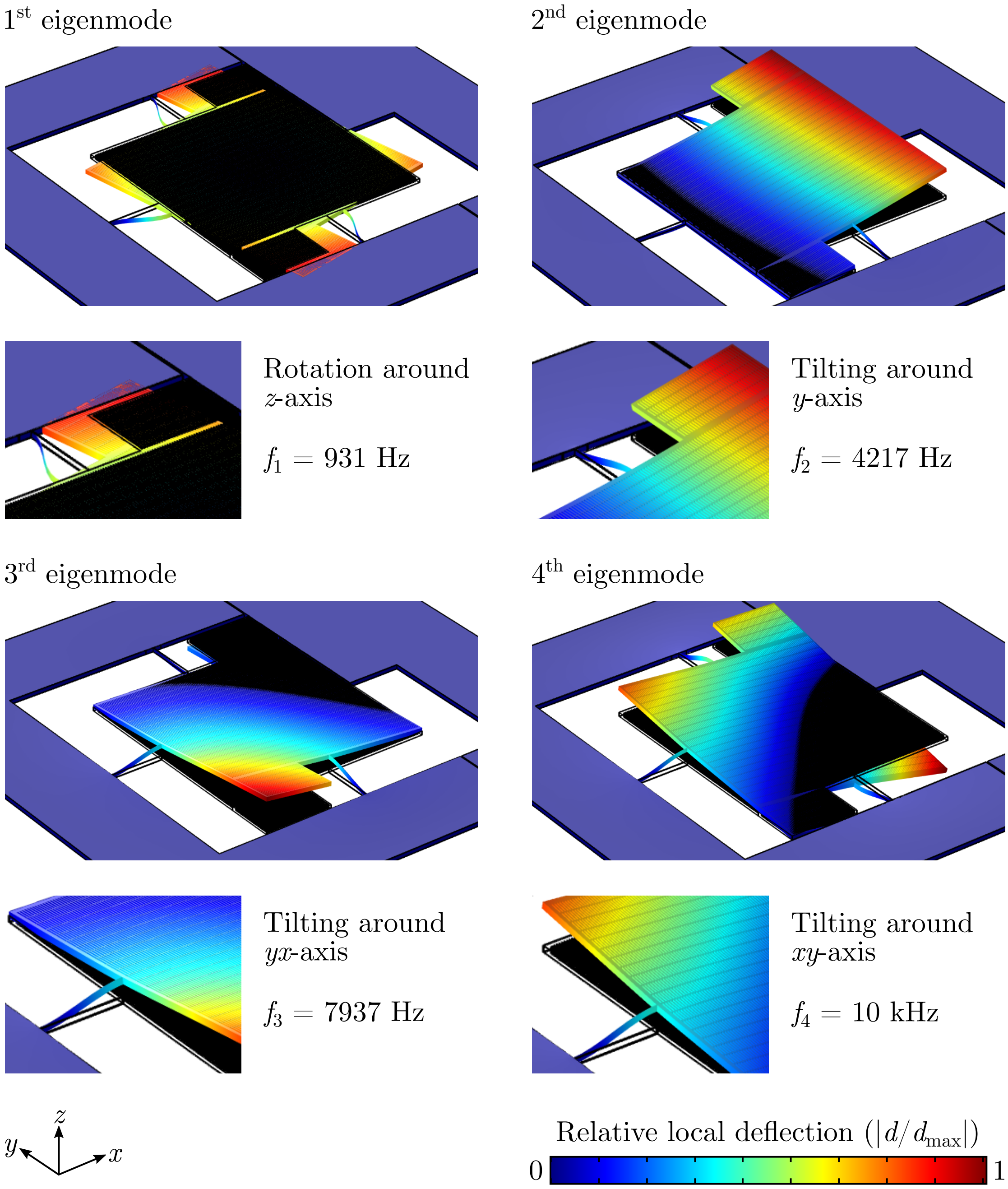

Figure 4.11.: Mode shapes of the first four eigenmodes of a rotational MEMS electric field sensor with straight beam springs. The fundamental mode with calculated frequency $f_0 = 931$ Hz corresponds to the desired rotation around the z-axis. The other depicted modes (all tilting) occur at much higher frequencies.

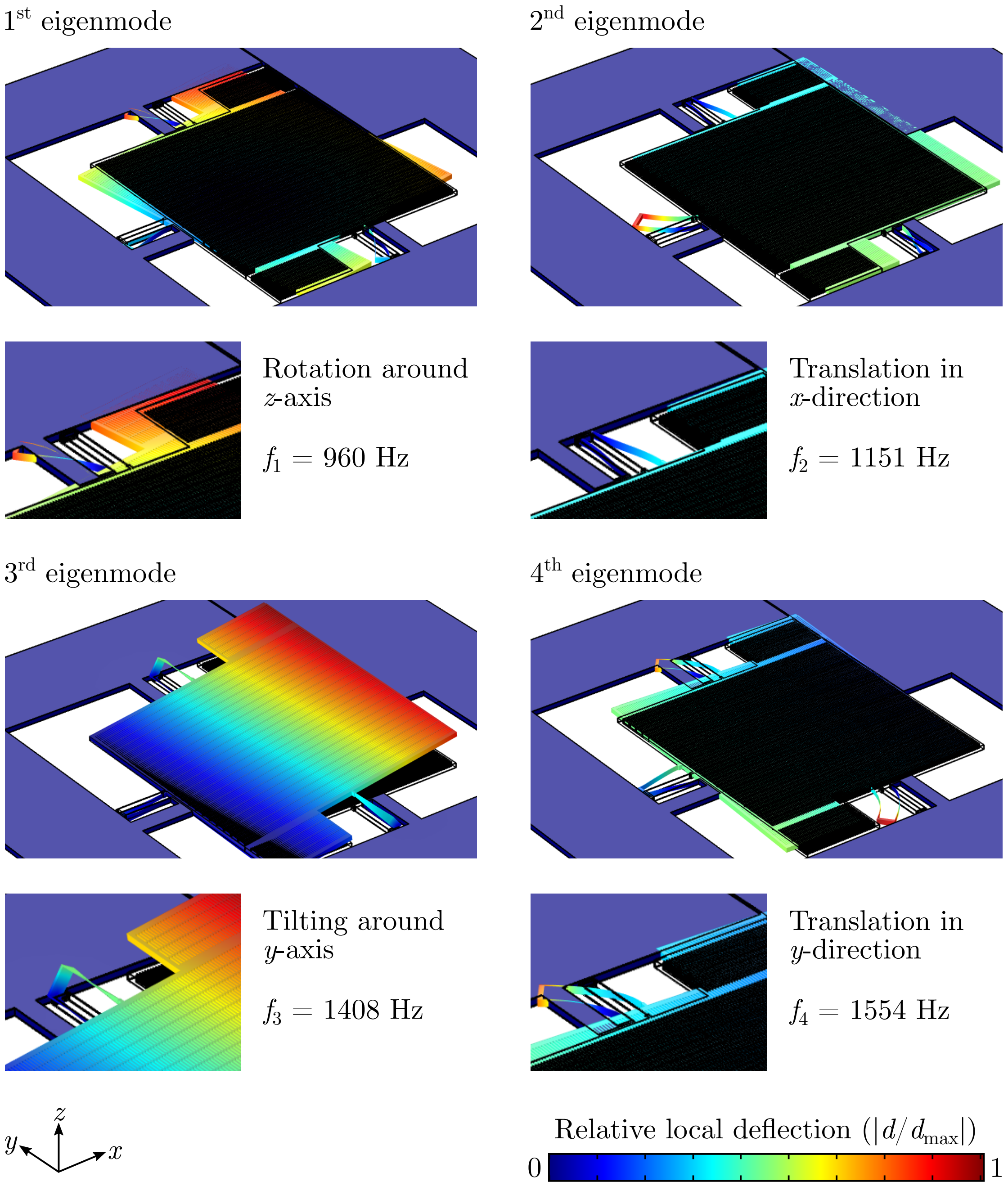

Figure 4.12.: Mode shapes of the first four eigenmodes of a rotational MEMS electric field sensor with U-shaped springs. The fundamental mode with calculated frequency $f_0 = 960$ Hz corresponds to the wanted rotation around the z-axis. The second and fourth modes correspond to the translational modes in x- and y-direction, respectively. Their frequencies are close to the fundamental mode and, thus, it is expected that vibrations will affect the sensor more significantly than for the straight beam structure.

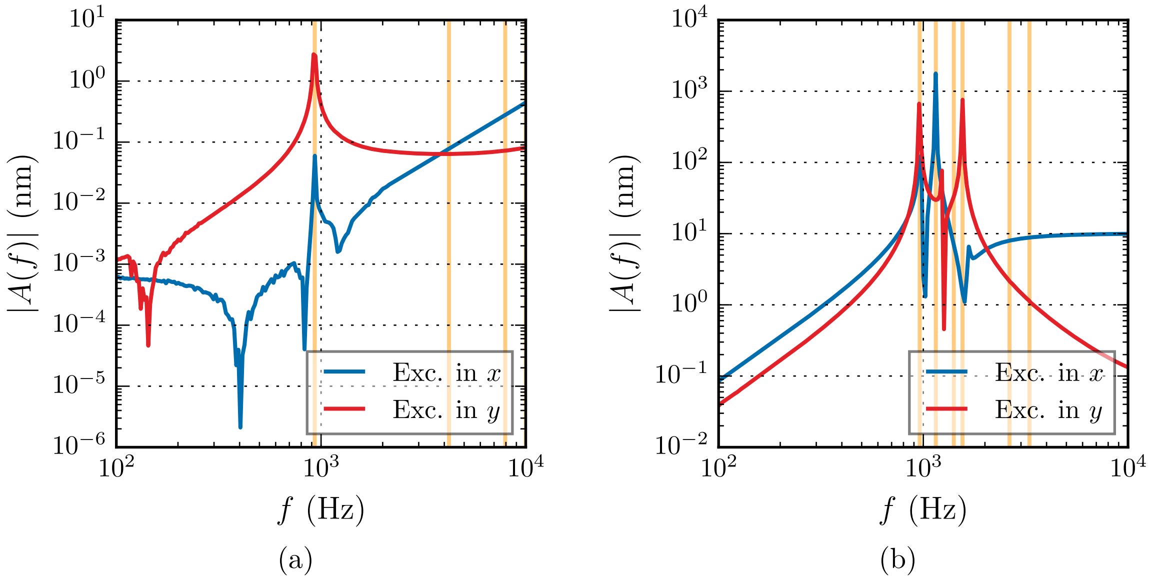

(a) (b)

Figure 4.13.: FEM results of the frequency domain analysis for an input vibration of 10 nm of the two layouts depicted in Fig. 4.10 with (a) corresponding to the straight springs and (b) to the U-shaped springs. It can be seen from the scale of the ordinates that the straight springs suppress the vibrations more effectively than the U-shaped beams. The noisy behaviour of the curves in (a) can be attributed to numerical errors.

the translational layout (see Fig. 4.4). This matches the results from the eigenfrequency study in the fact that the second mode, i.e. the translational mode, is close to the fundamental one. In addition, several other modes are visible in the plot in contrast to the straight beam structure. Furthermore, it can be noticed that the response for the x- and y-direction have roughly the same strength.

Thus, it can be concluded that the straight beam suspension offers superior protection against interfering mechanical vibrations. In the next step, the response to an external electric field was investigated as in sec. 4.3.

This time, not only the displacement in direction of the external field E_0, i.e. the x-direction, was examined, but also the displacement in y-direction, since the inertial mass ought to perform a rotational movement. For this examination, the uppermost point of the motional mass was chosen as reference point. The electric field was again set to $E_0 = 5.26$ kV/m. The resulting transfer functions are depicted in Fig. 4.14.

Similar to the response to the vibrations in Fig. 4.13, for the straight beam structures, the low-pass function $A(f)$ only shows the peak of the fundamental mode. In contrast, for the U-shaped beam structures, also higher modes are excited, however with the rotational

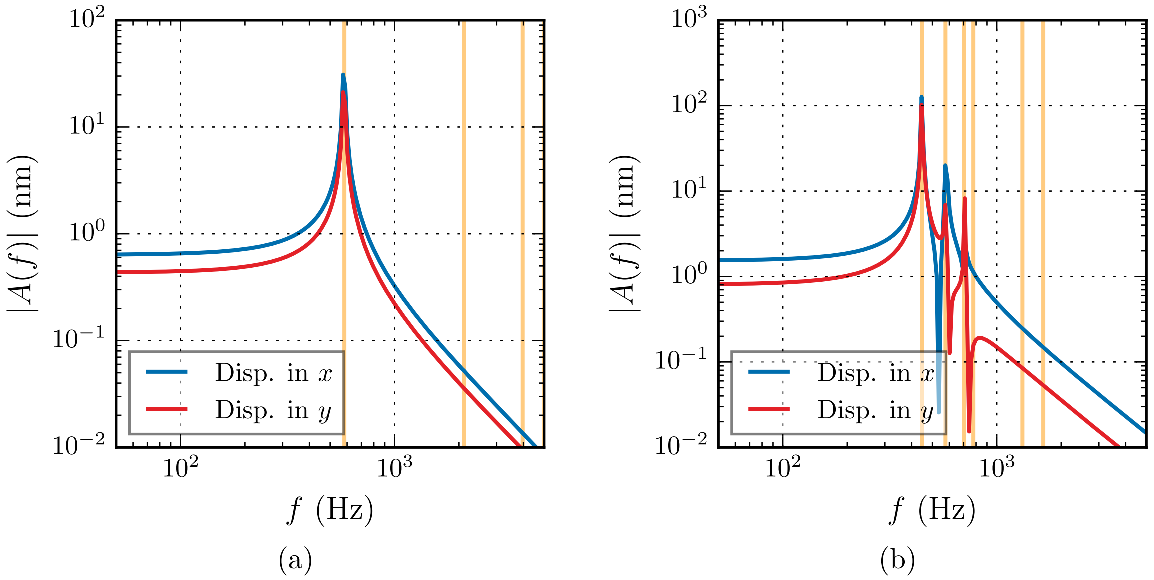

Figure 4.14.: Response of the rotational layouts to an electric field of $E_0 = 5.26$ kV/m for (a) the straight beam springs and (b) the U-shaped beams obtained by FEM simulations. The respective displacements in x- and y-direction have been extracted for the topmost point on the inertial mass. For the straight springs, only the fundamental mode is excited, while for the U-shaped beams also the higher modes are present. Compare Fig. 4.6.

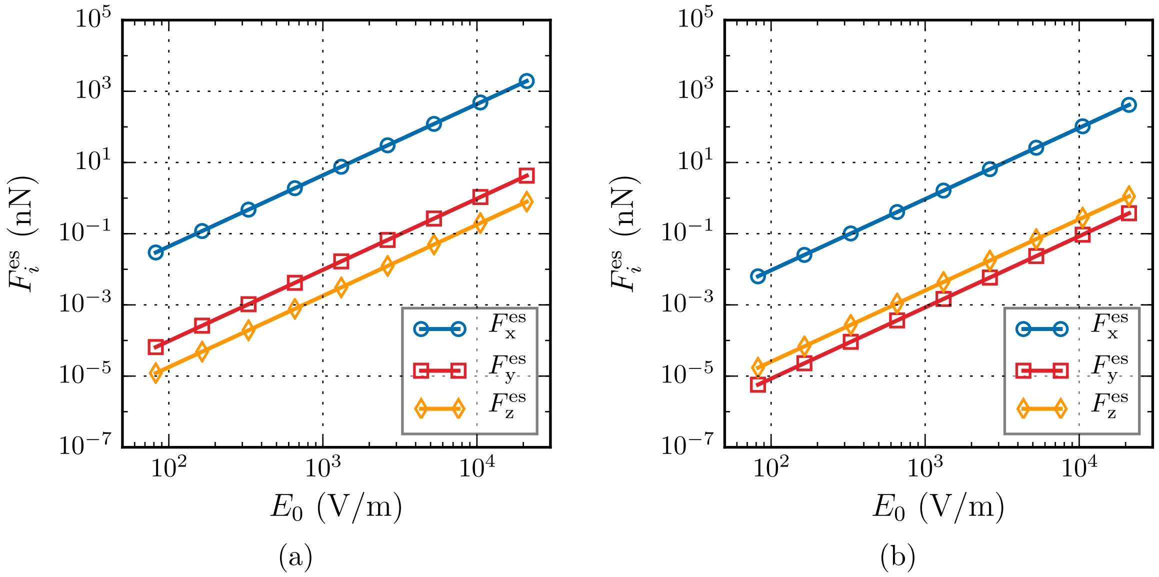

Figure 4.15.: Force components of the rotational E-field sensors for a variation of fields E_0. (a) corresponds to the straight beam structures, (b) to the U-shaped beam structures. Compare Fig. 4.5a.

mode as the highest. Nevertheless, in the relevant frequency range $f \lesssim f_0$, the two layouts behave similarly with the U-shaped beam structure exhibiting a bit larger amplitude.

For the sake of completeness also the individual components of the electrostatic force F_i^{es} are compared and tested for their quadratic behaviour. The results are depicted in Fig. 4.15. The x-component is, as expected, the dominating one. The other components are, as for the translational structure, smaller by several orders of magnitude and, thus, have hardly any influence on the moving mass. Furthermore, it can again be noticed that the force increases quadratically with the external field $F_i^{\mathrm{es}} \propto E_0^2$.

From a FEM point of view, the structures with the straight beam suspension pose a superior layout in terms of vibration suppression. It is, however, expected that the actual sensitivity is lower than for MEMS with U-shaped beams.

4.5.3. Measurements

In order to test these numerical results and assumptions based on them, the two layouts were fabricated. The width of the sensing gap was set to $x_{\mathrm{r}} = 15$ µm. As before, ten copies each of these two layouts have been fabricated. After fabrication, the chips were tested first in the shaker setup (subsection 2.3.1) to investigate the resistance to vibrations and to test if they are working and subsequently in the E-field setup (subsection 4.4.2).

The sensors were excited with three different amplitudes $X_0 \approx 8, 16, 24$ nm. For the straight beam structures it was necessary to excite the chips not only in x- but also in y-direction, since the amplitude and the course of the output signal were quite low and atypical. This can be seen in Fig. 4.16a, where the measured frequency response to both directions is given. This graph agrees quite well with the FEM results Fig 4.13a, especially with respect to the increasing trend above the fundamental mode, here at around 320 Hz, and the fact that the response to the y-directed vibration is stronger due to the assymmetry of the suspension. The low amplitude of $A_{\mathrm{mech}}(f)$ reflects the good resilience of the straight beam suspension against the vibrations.

The results for the electric field measurement are depicted in Fig. 4.16b. Obviously the interferences which were clearly visible for the translational devices in the range from roughly 40 to 100 Hz, e.g. in Fig. 4.9a, are not present in this plot. While the MEMS sensor seemingly works, the amplitude $|A_{\mathrm{es}}(2f)|$ is very low compared to the translational devices (and also to the rotational devices featuring the U-shaped springs). Furthermore, the rotational mode is not visible. Instead, the course of $|A_{\mathrm{es}}(2f)|$ suggests that one of the higher modes is excited which also explains the low amplitudes. In the present form, this

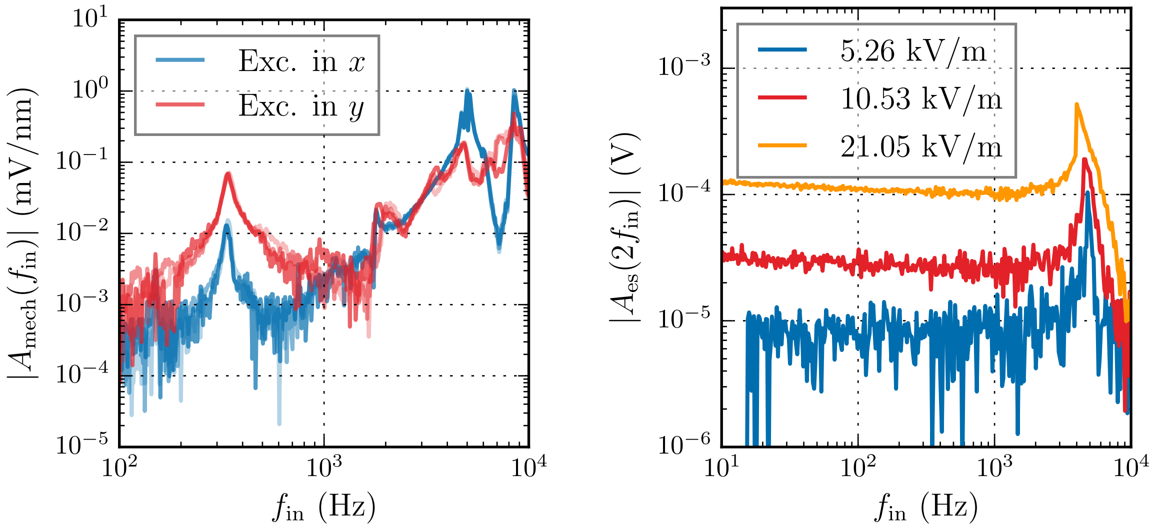

(a) (b)

Figure 4.16.: Mechanical and electrostatic frequency response of an exemplatory MEMS sensor with straight beam suspension. (a) Response for input vibrations in both x and y direction. (b) Electric field measurement.

type of layout does not pose a good approach for the E-field sensor.

As for the MEMS with the U-shaped beam suspension, the results of an exemplatory structure are depicted in Fig. 4.17. In the mechanical frequency responses $|A_{\mathrm{mech}}(f)|$ (Fig. 4.17a) which were also obtained for excitation amplitudes $X_0 \approx 8, 16, 24$ nm, three modes are visible. The lowest mode which has the shape of a bipolar peak corresponds to the rotational one, whereas the second mode corresponds to the translation. This roughly agrees with the FEM results depicted in Fig. 4.13b. Upon a closer look, the second peak actually constitutes two modes one of which is the translational mode and the other presumably the tilting mode depicted in Fig. 4.12. The different locations of the modes can be attributed to the spring width which turned out slightly smaller due to the etching process.

The electric field measurements shown in Fig. 4.17b worked fine and agreed with both the FEM simulations (Fig. 4.14b) and the mechanical measurements. In contrast to the straight beam structures, the same modes are visible here as in Fig. 4.17a. Also, the second peak in $|A_{\mathrm{es}}(2f)|$ contains two modes as in the mechanical response. Furthermore, it can be noticed that even though the resistance to vibrations is not that strong as compared to the straight beam structures, the interferences of the ventilation system (at ~ 40 Hz $< f <\sim 100$ Hz) are hardly present.

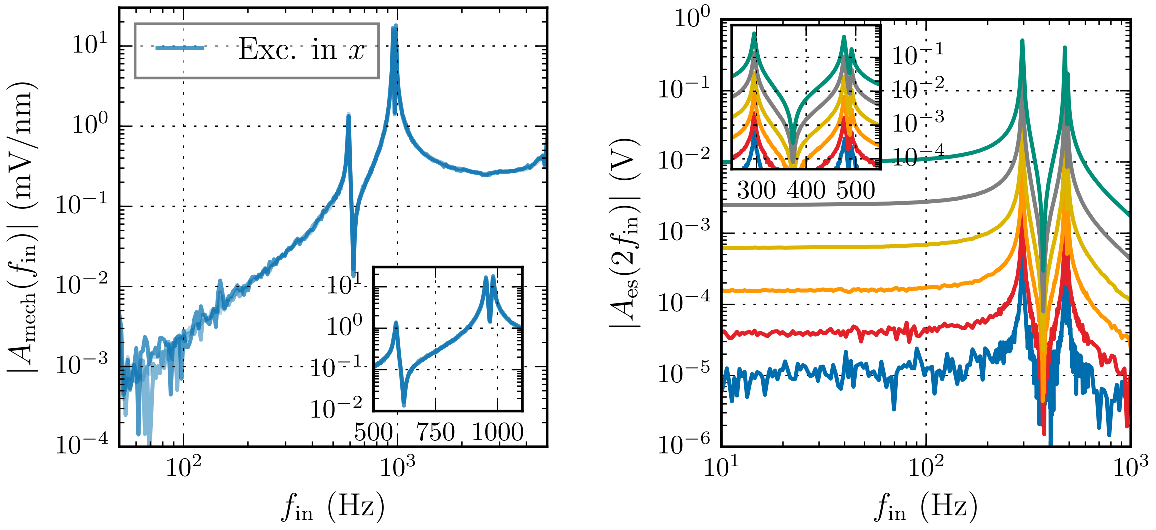

(a)

(b)

Figure 4.17.: Mechanical and electrostatic frequency response of an exemplatory MEMS sensor with U-shaped beam suspension. (a) Response for input vibrations x direction. (b) Electric field measurements for several fields doubled five times starting from $E_0 = 658$ V/m to $E_0 = 21.1$ kV/m. It can be seen in the insets that the peak on the right consists of two modes.

Out of the ten MEMS with U-shaped beams which were fabricated, four have been measured. The others were not working mainly due to the water inflow during the dicing step. The mean mechanical resonance frequency was determined by least-squares fitting to be $f_0 = 590.5 \pm 11.9$ Hz and the mean decay parameter to $\gamma = 45.6 \pm 4.1$ s^{-1}. This yields a quality factor of roughly $Q = 40$.

The mean sensitivity of the MEMS with respect to the external electric field E_0 was also determined by least-squares fitting and revealed a value of $S_{\mathrm{es}} = 62.39 \pm 6.8$ µVs^{-2}/(V/m)^2. The voltage noise limit of roughly 8 µV corresponds, for the structure regarded in Fig. 4.17, to an electric field of $E_{0,n} \approx 651$ V/m. Note that possibly due to the lesser irradiation (DC and AC) on the photodiode the noise level is slightly lower than for the translational MEMS. Considering the *ENBW* at 100 Hz of the lock-in amplifier and the mean resonance frequency, the resolution of this MEMS electric field sensor lies at $r_{\mathrm{es}} = 737$ V/m/$\sqrt{\mathrm{Hz}}$. The theoretical, i.e. Brownian, resolution limit for this device, however, can be calculated to be $r_{\mathrm{es,th}} = 59.3$ V/m/$\sqrt{\mathrm{Hz}}$. This is not far above the theoretical limit of the translational MEMS treated in sec. 4.4.3. The mass of the rotational structure which is necessary for this estimation of the theoretical noise floor was estimated to be $m = 5.11 \cdot 10^{-7}$ kg.

The mean resolution limit of the rotational MEMS devices with U-shaped beams was calculated to be $r_{\mathrm{es}} = 666.6 \pm 40.7\ \mathrm{V/m/\sqrt{Hz}}$. As expected, the resolution limit of these devices is much higher than that of the translational devices. Nevertheless, the vibration resilience of the U-shaped suspension was enough to block the interferences from the ventilation system, in contrast to what the FEM analyses suggested. These rotational E-field sensors, therefore, are promising candidates for future practical applications.

Conclusion and Outlook

In this thesis, an optomechanical MEMS transducer and its physical properties were studied. The transducer consists of a micromechanical silicon structure bearing an array of holes and a Cr layer bearing the same array of holes. These two arrays of holes form an optical shutter which modulates the light flux passing through the device when the moving part of the shutter is subject to a force.

It has been shown that the transfer characteristics of the micromechanic device can be fine-tuned in a wide range of reasonable Q factors. This was achieved based on a quite general analytical model, given in Eq. (2.26), for the air damping of lateral oscillators which was developed in this thesis. The model was proven to yield accurate results by comparison with FVM simulations and actual measurements. Furthermore, the limitations of the model, e.g. in reduced pressure or for intermediate values of the gap width x_r, were indicated. The model also showed that squeeze-film damping can play a major role in the energy dissipation in lateral oscillators. Based on this model, MEMS devices that have been optimised to a low quality factor $Q \gtrsim 1$, reaching a value as low as $Q = 1.16$ were designed and tested. Furthermore, it was shown that holes etched into the moving mass of the oscillator do not affect the damping parameter d. They affect, however, the quality factor, since $Q = \sqrt{k\,m/d}$ depends on the mass.

In addition, the optomechanical sensitivity of the transducer was investigated. It was shown that the sensitivity is indeed proportional to the number of holes N_h as stated in Eq. (1.1), even if the incident light is not collimated. Based on the measurements for varying hole dimensions and distances between, it can be concluded that the sensitivity for a given inertial mass can be increased by increasing N_h via implementing holes of smaller width w_h and smaller distance d_h. This way neither the mass changes nor the other oscillator parameters. Therefore, this does not lead to increased Brownian noise and would result in an improved resolution – given perfect optoelectronics and readout circuit.

Furthermore, it has been shown that using optical lenses to collimate the incident light, the efficiency of the transducer can be increased. Other options, i.e. Fresnel zones and large area organic optoelectronics, for the same purpose were explored, however without success. Both of these approaches did not yield higher efficiency, but the organic optoelectronics are, nevertheless, promising for future applications, e.g. if large-area or custom-shaped optoelectronics are required. It is also possible to integrate the OLED and OPD together with the MEMS onto a flexible substrate which might be interesting for wearable devices.

Since the MEMS part of the transducer is an entirely passive component and does not need electrical connections, it was possible to develop an electric field sensor based on this transducer which works by a unique transduction based on electrostatic induction.

With this completely new method for the the passive measurement of the true amplitudes of E-fields, the disadvantages encountered by state-of-the-art approaches, i.e. field distortion and temperature stability, can be overcome. The transducers were able to resolve electric fields in the quasistatic regime down to a limit of 173 $\mathrm{V/m/\sqrt{Hz}}$. This is near the perfromance of current field mills which have been worked on for a long period of time. At the moment, the resolution limit is determined by the electronic noise of the readout circuit. The fundamental limit of the sensor, i.e. the Brownian noise, estimated by the mean noise force $F_{\mathrm{th}} = \sqrt{4k_{\mathrm{B}}T\,d}$. It was shown that this corresponds to an equivalent displacement of $\delta x_{\mathrm{th}} = 0.56$ pm. The fundamental electric field resolution for the presented designs would, therefore, be $r_{\mathrm{es,th}} = 40.6\ \mathrm{V/m/\sqrt{Hz}}$.

Since these devices are affected by interfering mechanical disturbances, two types of rotational devices were investigated. Due to their primary mode of motion, they feature a much higher resilience against these mechanical interferences. One of these types, i.e. with the straight beam suspension, exhibited an especially outstanding protection against these interferences. On the other hand, it showed a quite strange behaviour when measuring electric fields, since the response amplitudes are very small and the rotational mode is not visible in the spectrum. The other type, featuring U-shaped beam suspension, exhibited a mediocre resilience against vibrations, but the performance as E-field sensor was good with a mean resolution of $r_{\mathrm{es}} = 666.6 \pm 40.7\ \mathrm{V/m/\sqrt{Hz}}$. Furthermore, the protection from the mechanical interferences proved to be good enough to suppress the effects of the ventilation system inside the laboratory.

A further general benefit of the concept is the temperature stability of the device. The temperature affects the Young's modulus of the Si part of the MEMS in the range of 50 ppm/K [87], and leads to thermal expansions in the range of 2.3 ppm/K. This reflects mainly in the stiffness and, thus, the deflections of the motional mass. Hence, the temperature dependence of the MEMS is systematic and small. If optical fibres are used to guide the light to and from the MEMS, the LED, photodiode, and readout circuit can be operated at remote locations at fixed temperatures. This way, the sensing system is hardly affected by temperature changes.

The observed variations of sensitivity and resolution are mainly due to the alignment of the MEMS chip in the measurement setup. This issue will be solved by implementing fibre connections to couple the light to and from the chip in a well defined way. Another issue regarding the yield of MEMS is expected to be solved by changing the dicing step. It is envisaged that dicing along the critical axes, i.e. orthogonal to the separation gap, is performed by breaking the wafer along perforated paths along the cristallographic direction. Since the quadratic behaviour of the electrostatic force $U_{\mathrm{out}} \propto F_{\mathrm{es}} \propto E_0^2$ might be a limiting factor regarding the dynamic range of the E-field sensor, nonlinear springs can be explored which can be used to achieve an effective linear characteristic [88].

Following the results obtained by the FEM simulations and optimising the geometry of the sensing gap, future devices with a resolution down to 1 $\mathrm{V/m/\sqrt{Hz}}$ are feasible. This resolution can be improved even further, if, e.g., the device is packaged in an evacuated encapsulation.

Appendix A.

Device Fabrication

This appendix shall give an overview of how the MEMS transducers were fabricated. The procedure is the same, regardless of the type of MEMS – vibration sensor or electric field sensor – which is processed. The optical shutter presented in this thesis requires two arrays of holes positioned above each other. This was achieved by patterning one (the moving one) in silicon and the other one (the immobile one) in a Cr layer. Therefore, two different wafers were processed in parallel, one silicon on insulator (SOI) wafer and one glass wafer which were bonded together at the end of the procedure [14].

The SOI wafers (all 100 mm) used within the scope of this thesis consist of a p-type doped device layer with a specific resistance of less than 0.01 Ωcm. The low resistance is, actually, not necessary for the optomechanical transduction of the MEMS, but helpful for E-field sensing and other devices fabricated alongside the ones presented in this thesis. Due to availability, wafers with several device layer thicknesses (20, 45, and 50 µm) have been used. The handle layer consisted of less doped Si exhibiting a resistance in the range of 1 – 5 Ωcm and a thickness of 350 µm. The fabrication steps described in the following are depicted in Fig. A.1.

At first, the device layer was processed. After photolithographic patterning of photoresist, metal was deposited onto the device layer. This was done by physical vapor deposition of gold on an adhesive layer of titanium. The metal served two purposes: first of all, for the orientation markers for the dicing, and, if necessary, for defining electrical pathways and bond pads. After lift-off of the remaining photoresist, the device layer – now equipped with metal – was prepared for deep reactive ion etching (DRIE, Bosch process) of the MEMS geometry. This was also done by photolithographic patterning of resist. After the DRIE, the device layer was coated in a protective layer of photoresist in order to preserve the delicate Si structures during processing of the handle layer.

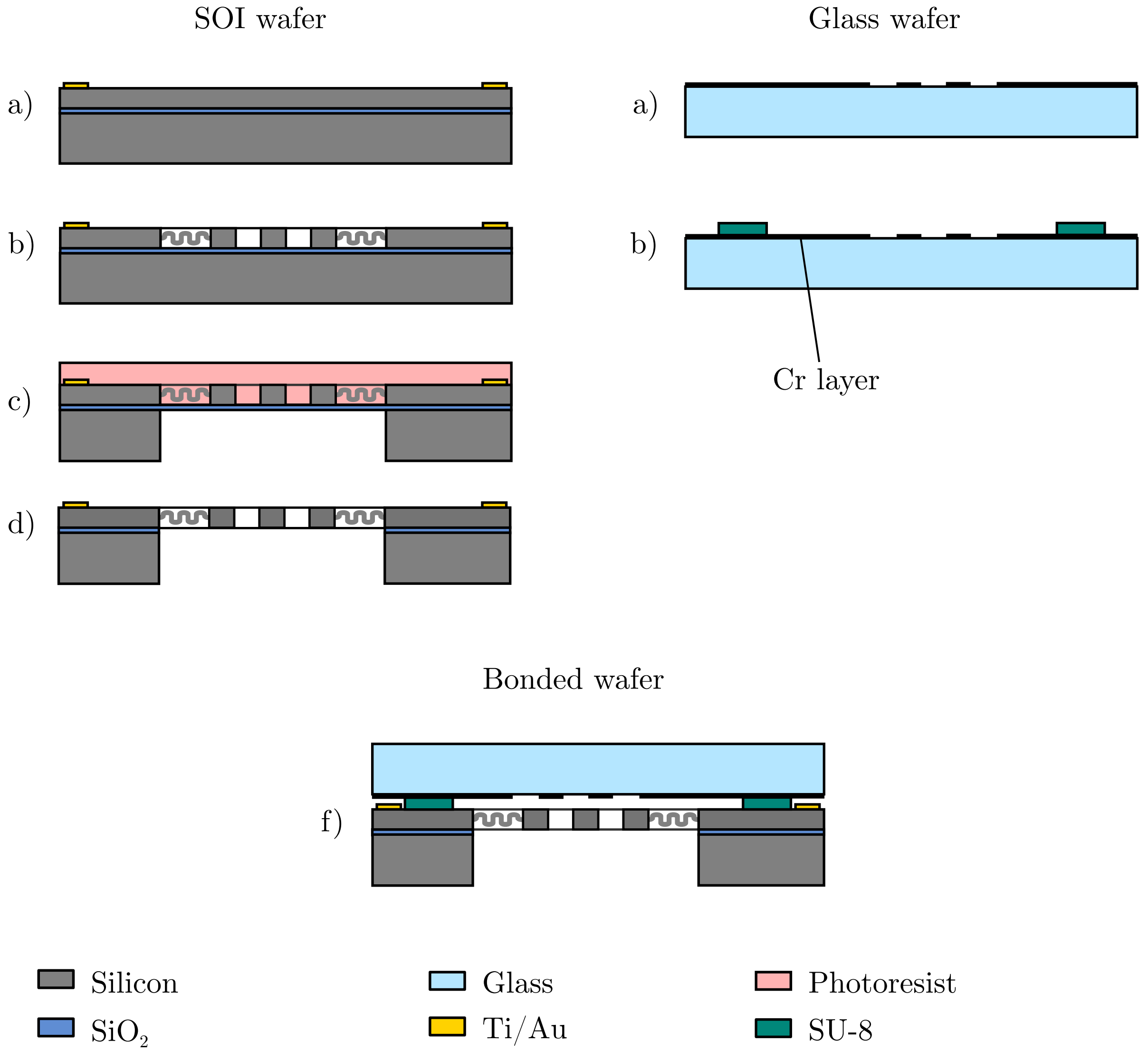

Figure A.1.: Wafer-level fabrication of the MEMS devices.
SOI wafer (left): a) PVD of Ti/Au for saw markers and eventual bond pads or leads. b) DRIE of the moveable structures in the device layer. c) Coating with protective photoresist. d) DRI backside etch and release of the moveable parts.
Glass wafer (right): a) PVD of Cr. b) patterning of SU-8.
f) the two wafers are bonded together and then diced.

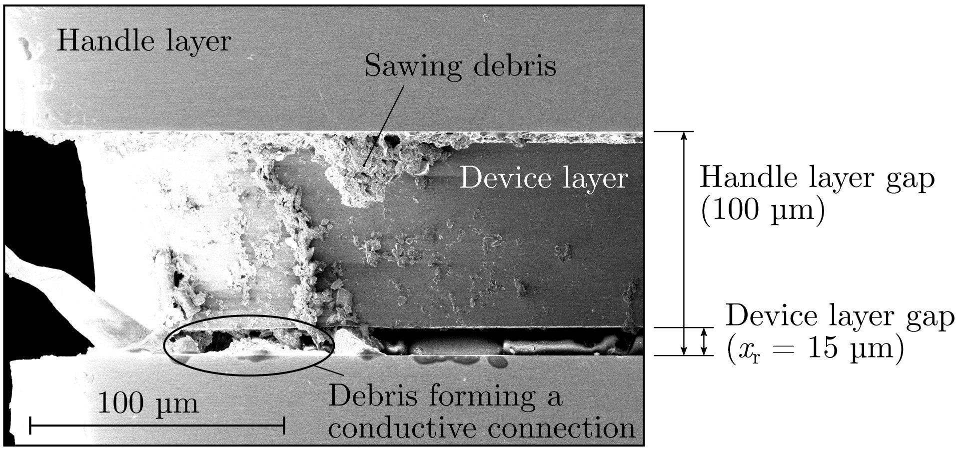

Figure A.2.: SEM image of the backside of a MEMS chip which has been impaired by sawing debris forming a conductive connection between the two device layer Si domains [86].

The handle layer needed to be removed below the moving components etched into the device layer in order for them to be able to move. This was again done by photolithography and DRI etching of the handle layer Si and subsequent wet-chemical dissolution of the insulating SiO_2 layer with BHF. Afterwards, the protective photoresist on the device layer was removed.

In parallel, the glass wafer was processed. In the first step, photoresist was patterned for the PVD by evaporation of Cr. After the PVD and the lift-off, SU-8 was patterned in a second photolithography step. The SU-8, being a photoresist itself, was used as adhesive in the following step.

After separate preparation of the SOI and glass wafers, the two wafers are bonded together. This is done by aligning the two wafers and applying a defined force pressing them together. The SU-8 served as bonding adhesive and spacer. This spacing between the wafers can be adjusted by the original thickness of the spin-coated SU-8 and the force applied during bonding. Distances roughly between 4 and 20 µm have been achieved this way.

In the last step, the wafer was diced. The dicing was done by a wafer saw working with a water cooled, diamond coated blade. As for the E-field sensor chips, this step was quite problematic due to the water. Since the two silicon domains are separated in this step, the water flows into the chip which can be harmful in two ways. First, the water may lead to sticking of the moveable components to the immobile ones which may impair or destroy the MEMS. Another problem can arise when the sawing debris is deposited in the gap separating the domains which is shown in Fig. A.2 [86]. This way, a conducting connection can emerge which eliminates the electromechanic transduction effect. The latter problem was accounted for, by designing the gap near the edges wide enough.

Appendix B.

Readout Circuit

The readout circuit used within the scope of this thesis is one of the crucial components in evaluating the quantities to be measured with the sensor. Its main purpose is to transform the photocurrent through the phototransistor or photodiode into a voltage while at the same time amplifying it [14, 89]. The other purposes of the circuit are to provide a well-defined bias voltage for the phototransistor or -diode and to offer the possibility of offset compensation. This offset compensation is necessary, since, typically, the moving part of the MEMS shutter only performs small amplitude deflections δx around its resting position which, ideally, is shifted by half the width of one hole w_h with respect to the immobile part of the shutter. Thus, with $\delta x \ll w_\mathrm{h}$, only a small portion of the light flux picked up by the detector is proportional to the quantity to be measured. The largest part which reflects in a steady DC component of the photocurrent contains no valuable information and is compensated by the circuit. This appendix shall give a bit more analytical insight to the circuit and provide a profound basis for populating the circuit depending on the kind of photodetector used.

A schematic of this circuit is depicted in Fig. B.1. The photocurrent $i_\mathrm{p} = I_\mathrm{p}^0 + i_\mathrm{p}^\sim$, consisting of the large DC component I_p^0 and the small AC component $i_\mathrm{p}^\sim$, is transformed via the feedback resistor R_f into the output voltage $u_\mathrm{out} = -R_\mathrm{f} i_\mathrm{p} + const.$ Therefore, R_f serves here also as amplification. The constant term takes into account the effects of the other components in the circuit, e.g. voltage divider or potentiometer.

For a given supply voltage U_0 (12 V within the scope of this thesis), the voltage divider consisting of R_3 and R_4 sets the voltage U_+ at the noninverting input of the operational amplifier (OPA). This also sets the voltage U_- at the inverting input and, in-turn, the bias voltage U_b of the PD which can be written for an assumed ideal OPA $U_\mathrm{b} = U_- = U_+ = U_0\, R_4/(R_3 + R_4)$.

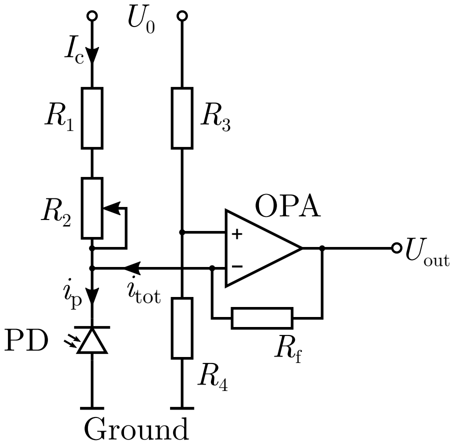

Figure B.1.: Schematic of the readout circuit. The photocurrent through the photodiode (or phototransistor) is transferred into a voltage u_out via the transimpedance R_f. The resistors R_3 and R_4 set the bias voltage for the PD. The summed up resistance $R_1 + R_2$ of the pre-resistor R_1 and the potentiometer R_2 sets the current compensating the DC component of the photocurrent.

The total current across the feedback resistor $i_\mathrm{tot} = I_\mathrm{c} - i_\mathrm{p}$ is the sum of the photocurrent and the compensation current i_c determined by the combined resistance $R_\mathrm{c} = R_1 + R_2$ of the potentiometer R_2 and the pre-resistor R_1 and can be written as $I_\mathrm{c} = (U_0 - U_+)/R_\mathrm{c}$. The output voltage is, then, given as

$$u_\mathrm{out} = -R_\mathrm{f}(I_\mathrm{c} - i_\mathrm{p}) + U_+. \tag{B.1}$$

Inserting the expressions for i_c and U_+, one arrives at

$$u_\mathrm{out} = R_\mathrm{f}(I_\mathrm{p}^0 + i_\mathrm{p}^\sim) + U_0\left[\frac{R_4}{R_3 + R_4}\left(1 + \frac{R_\mathrm{f}}{R_\mathrm{c}}\right) - \frac{R_\mathrm{f}}{R_\mathrm{c}}\right]. \tag{B.2}$$

It can be seen that the output voltage depends on every component of the circuit and not only on the photocurrent. The second term which is proportional to the supply voltage can be used to compensate the voltage stemming from the DC component of the photocurrent by choosing adequate resistors and a potentiometer with the right range. For this consideration, one can set the expression for the output voltage excluding the term $R_\mathrm{f}\, i_\mathrm{p}^\sim$ to zero. This leads to the following expression for the compensation resistance:

$$R_\mathrm{c} = \frac{R_\mathrm{f} R_3}{(R_3 + R_4)\frac{R_\mathrm{f}\, I_\mathrm{p}^0}{U_0} + R_4}. \tag{B.3}$$

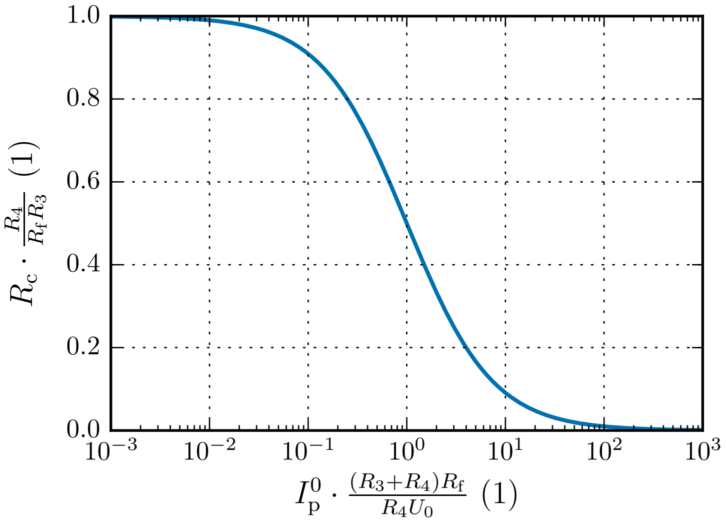

Figure B.2.: Behaviour of the normalised compensation resistance $R_c R_4/R_3 R_f$ as function of the normalised DC photocurrent $I_p^0(R_3+R_4)R_f/R_4 U_0$ as described in Eq. (B.3).

The resistance which is necessary to compensate a given I_p^0 is depicted in Fig. B.2. It can be seen that the maxiumum resistance is necessary for minimum photocurrent and increasing I_p^0 needs decreasing R_c. Hence, for $I_p^0 \to 0$, R_c takes on the maximum value

$$R_{c,max} = R_f \frac{R_3}{R_4}, \tag{B.4}$$

which can be used to adequately choose a potentiometer.

In the case of using the photodiode as light detector (as in chapters 3 and 4), a large feedback resistor of 1 MΩ was chosen for a reasonably good *SNR*. With a supply voltage of U_0 = 12 V and a bias voltage of U_b = 4 V set by R_3 = 20 kΩ and R_4 = 10 kΩ, the potentiometer resistance has to feature a maximum value of R_c = 2 MΩ.

In contrast to that, if a phototransistor is used as light detector (see chapters 2 and 3), a much lower feedback resistor is necessary, since the photocurrents through the transistor are much larger than for the PD. In this case, R_f = 10 kΩ was chosen while having the same resistors of the voltage divider. Hence, from Eq. B.4 follows that the maximum compensation resistance ought to be R_c = 20 kΩ.

Appendix C.

Equivalent Circuit Model of the Electric Field Sensor

The electric field sensor presented in chapter 4 can be qualitatively understood in terms of an equivalent circuit model. This models also allows to take into account eventual parasitic effects and material properties. Such parasitic effects have been observed while evaluating the first electric field measurements performed with the presented MEMS sensors. The explanation provided by the analytical model helped to improve the setup and diminish these parasitic effects.

The measurement setup depicted in Fig. 4.7 in combination with the MEMS chip inside can be understood as three capacitors connected in series (see Fig. C.1). The first capacitor C_1 comprises one of the aluminum plates and the opposing side face of the device layer of the MEMS chip. The second capacitor C corresponds to the sensing gap of the MEMS chip and the third capacitor C_3 encompasses the remaining aluminum plate and opposing face of the MEMS chip. Since the chip is placed in the centre of the setup and the dimensions of the plates are the same, it follows with sufficient accuracy that the external capacitors are the same, i.e. $C_1 = C_3 =: C_\mathrm{e}$. The voltage U_0 applied to this voltage divider corresponds to the voltage which generates the electric field E_0 to be measured. The force picked up by the sensor corresponds to the square of the voltage drop U at C, i.e. $F_\mathrm{es} \propto U^2 = H_0^2 U_0^2$. The voltage drop $U = H_0^2 U_0^2$ can be calculated by evaluating the characteristic H_0 of the capacitive voltage divider. The total impedance Z_tot can be written as

$$Z_\mathrm{tot} = \frac{2}{\mathrm{i}\omega C_\mathrm{e}} + Z_0 = \frac{2}{\mathrm{i}\omega C_\mathrm{e}} + \frac{1}{\mathrm{i}\omega C} = \frac{2\mathrm{i}\omega C + \mathrm{i}\omega C_\mathrm{e}}{-\omega^2 C C_\mathrm{e}}, \tag{C.1}$$

where $Z_0 = (\mathrm{i}\omega C)^{-1}$ is the impedance of the sensing gap. The voltage drop U is given by

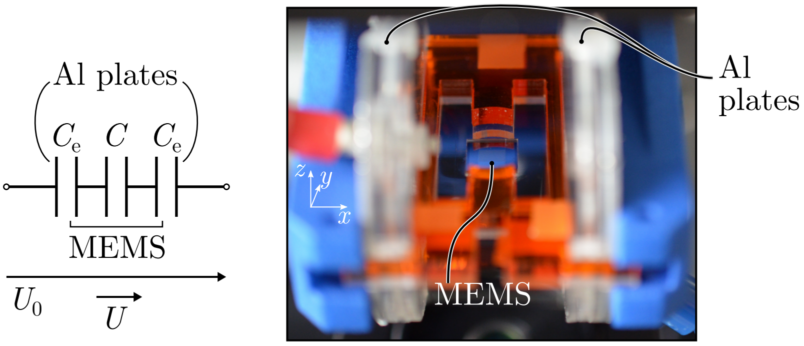

Figure C.1.: Equivalent circuit diagram of the E-field measurement setup. The ideal system can be understood as three capacitors connected in series and the electrostatic force exerted on the sensor as proportional to the square of the voltage drop at the centre capacitor C which corresponds to the sensing gap of the MEMS.

$U = U_0 Z_0 / Z_\mathrm{tot}$ with

$$H_0 = \frac{Z_0}{Z_\mathrm{tot}} = \frac{1}{1 + 2\frac{C}{C_\mathrm{e}}}. \tag{C.2}$$

This expression does not depend on ω and, thus, poses only a constant factor. Equation (C.2) corresponds to the ideal case, i.e. perfect conductance of the Si and infinite resistance of the gaps between. Furthermore, it reveals that a low ratio C/C_e is in favour of a high voltage drop across C and, thus, a high force F_es. In this context, the general frequency response of the sensor can, therefore, be written as

$$A(\omega) = \alpha H_0^2 U_0^2(\omega)\chi(2\omega) = \alpha \frac{1}{(1 + 2\frac{C}{C_\mathrm{e}})^2} U_0^2(\omega) \frac{1}{\omega_0^2 - 4\omega^2 + 4\mathrm{i}\gamma\omega} \tag{C.3}$$

with α being a proportionality factor and χ the mechanical susceptibility – compare Eq. (1.4).

The capacitances of the actual setup can be estimated in order to provide an approximation

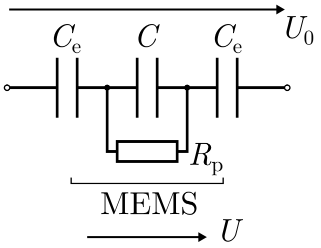

Figure C.2.: Equivalent circuit diagram of the E-field measurement setup with a parasitic resistance R_p in parallel to C.

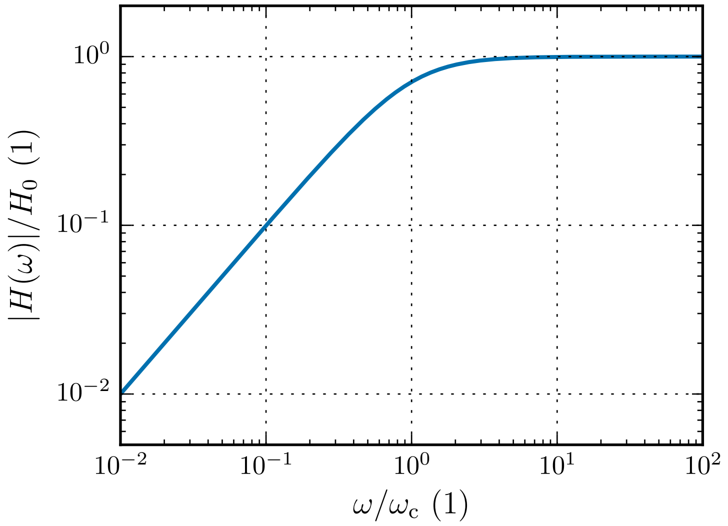

Figure C.3.: Normalised amplitude of $H(\omega)$ according to Eq. (C.4) if a parasitic resistance is present. For large frequencies and $R_p \to \infty$, the function $H(\omega) \to H_0$ approaches the ideal case Eq. (C.2).

for the value of H_0. The external capacitors C_e are composed of one of the Al plates and one face of the device layer of the MEMS chip. Assuming the chip is placed in the centre of the setup and 6 mm wide, the distance between the plate and the chip face is given by $d_e = 6.5$ mm. The mean area of the capacitor can be estimated by $A_e = 3.64 \cdot 10^{-4}$ m^2. Therefore, the external capacitance roughly has a value of $C_e \approx \varepsilon_0 A_e / d_e = 0.49$ pF. The capacitance C of the sensing gap can be estimated in a similar manner and has around $C \approx 0.13$ pF for a 10 µm gap. Inserting these values into Eq. (C.2) yields $H_0 \approx 0.66$.

This equivalent circuit approach can also be used to explore what happens, if a parasitc resistance R_p in parallel to C occurs (see Fig. C.2). The impedance of a resistor in parallel with a capacitor is given as $Z = R_p/(\mathrm{i}\omega R_p C + 1)$. The voltage drop $U = H(\omega)U_0$ over the sensing capacitor C is, therefore, proportional to the characteristic

$$H(\omega) = \frac{Z}{Z_{\text{tot}}} = \frac{1}{\left(1 + 2\frac{C}{C_e}\right)\left(1 + \frac{2}{\mathrm{i}\omega R_p (C_e + 2C)}\right)} = \frac{H_0}{1 + \frac{\omega_0}{\mathrm{i}\omega}}. \tag{C.4}$$

In contrast to the ideal case Eq. (C.2), this expression is frequency dependent. Its normalised amplitude is depicted in Fig. C.3 and corresponds to a first order high-pass with corner frequency $\omega_c = 2/R_p(C_e + 2C)$.

It can be seen that a finite parasitic resistance severely affects the E-field transduction

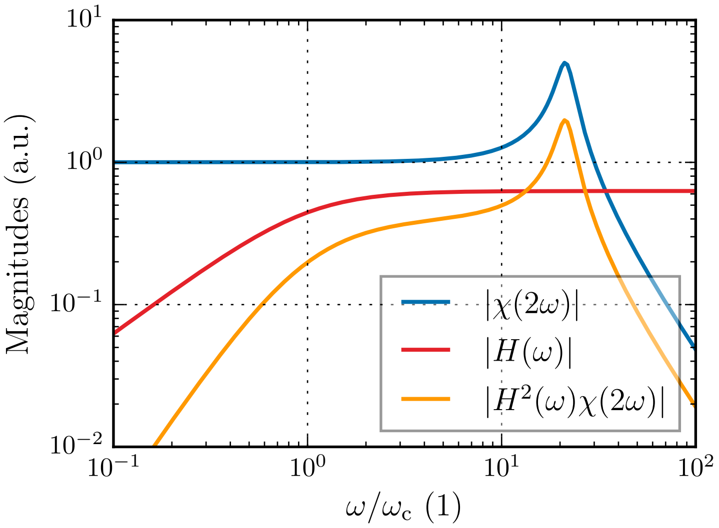

Figure C.4.: Frequency dependent magnitudes of the functions $\chi(2\omega)$ (blue), $H(\omega)$ (red) and $H^2(\omega)\chi(2\omega) \propto A(\omega)$ (orange). It can be seen that the parasitic resistance significantly reduces the bandwidth of the E-field sensor.

for low frequencies and DC. In particular, the bandwidth becomes clipped for frequencies $\omega < \omega_c$. This is especially problematic, if the corner frequency is close to or larger than the mechanical resonance frequency, i.e. $\omega_c \gtrsim \omega_0$. Note that $H(\omega)$ enters the transfer function quadratically, $A(\omega) \propto H^2(\omega)\chi(2\omega)$. Therefore, the linear increase of $|H(\omega)|$ reflects in a quadratic increase in $|A(\omega)|$ worsening the circumstance. This general behaviour is depicted in Fig. C.4 where the three functions $\chi(2\omega)$, $H(\omega)$ and $H^2(\omega)\chi(2\omega) \propto A(\omega)$ are compared.

Due to this analysis, it was possible to identify a problematic component in the original measurement setup. Initially, it was intended that the MEMS chips were held in the setup by a 3D-printed holder, which was supposed to provide better reproducibility regarding the position of the chip. As shown in Fig. C.5, the chip holder material introduced a finite resistance in parallel to the sensing gap. This was not foreseeable, since the material is a typical polymer[1]. The observed corner frequency of roughly $f_c \approx 10$ Hz and the capacitances C_e and C estimated above suggest a parasitic resistance of $R_p = 1/\pi f_c(C_e + 2C) \approx 45$ GΩ. Even though this value is quite large, the effect was clearly noticeable. Therefore, the choice of mounting the MEMS chip is crucial for proper measurements.

One further aspect can be examined within this equivalent circuit model framework. So far, the quite strongly doped Si of the device layer was treated as perfect conductor,

---

[1] VeroWhitePlus

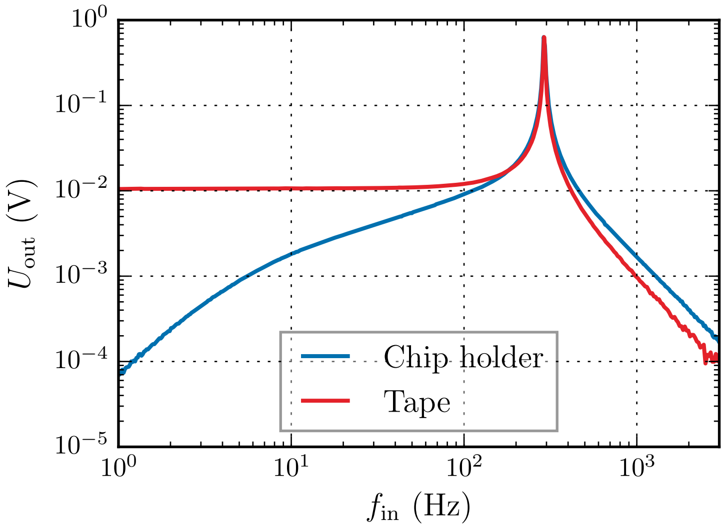

Figure C.5.: E-field recordings of the same MEMS sensor with $E_0 = 21$ kV/m. The measurement performed with the MEMS in the chip holder (blue) exhibits the bandwidth reduction as described by Eq. (C.4). Replacing the chip holder with an adhesive tape solved this issue (red).

i.e. $R = 0$. Since this is physically incorrect, a finite series resistor is introduced which accounts for this matter (see Fig. C.6). This combination is bound to introduce a frequency dependent behaviour to the system.

As before, the voltage divider is evaluated in order to derive the characteristic $H_{\text{s}}(\omega)$ of this configuration. With a total impedance of $Z_{\text{tot}} = 2/\text{i}\omega C_{\text{e}} + 1/\text{i}\omega C + R$, the characteristic can be written

$$H_{\text{s}}(\omega) = \frac{1}{1 + 2\frac{C}{C_{\text{e}}} + \text{i}\omega R_{\text{s}} C} = H_0 \frac{1}{1 + \text{i}\omega \frac{R_{\text{s}} C}{1 + 2\frac{C}{C_{\text{e}}}}}. \tag{C.5}$$

For $R_{\text{s}} \to 0$, the ideal expression Eq. (C.2) is recovered from this equation. According to Eq. (C.5), the finite resistance R_{s} introduces a first order low-pass behaviour to the system as depicted in Fig. C.7. Therefore, the electrostatic force is quenched at frequencies $\omega > \omega_{\text{s}}$ above the corner frequency $\omega_s = R_{\text{s}}^{-1}(C^{-1} + 2C_{\text{e}}^{-1})$. Hence, it is beneficial if R_{s} is as low as possible for given capacitances.

Given the specific resistance ρ_{e} of the device layer of the SOI wafer, the resistance R_{s} can be estimated. Since the narrowest structures of the MEMS are the springs, they are expected to contribute by far the most to R_{s}. According to the layout data of the Ch00 structures, a single U-shaped spring consists of two beams with length $l_{\text{b}} = 645$ µm, width

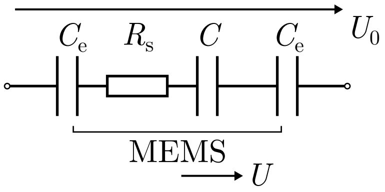

Figure C.6.: Equivalent circuit diagram of the E-field measurement setup with a series resistance R_s accounting for the finite conductivity of Si.

$w_b = 4$ µm and height $h = 50$ µm. The resistance of this beam, therefore, can be calculated to be $R_b = \rho_e l_b / w_b h = 322.5\ \Omega$. With two such beams per spring and four springs in parallel, the series resistance can be estimated to be $R_s \approx 160\ \Omega$. As a result of this low value, the corner frequency lies at roughly 12 GHz. This is very far above the mechanical resonance frequency ω_0 which already cuts off the frequency range of the E-field sensor. Therefore, it can be concluded that approximating the silicon as ideal conductor is a valid approach in this context.

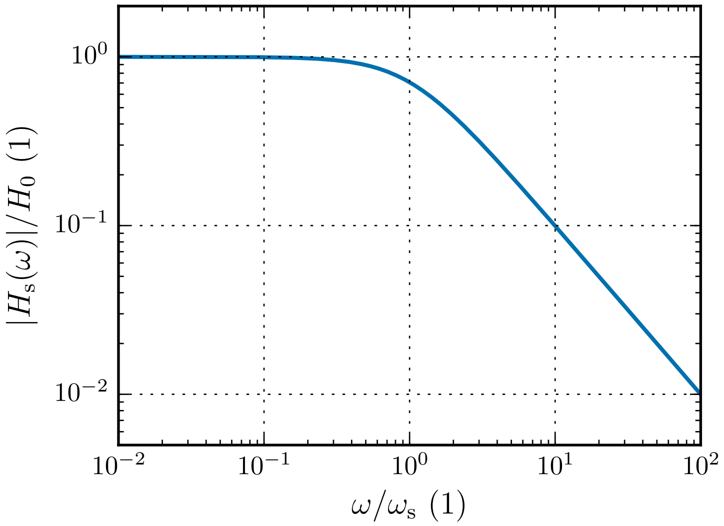

Figure C.7.: Normalised amplitude of $H_s(\omega)$ according to Eq. (C.5). For low frequencies and $R_s \to 0$, the function $H_s(\omega) \to H_0$ approaches the ideal case Eq. (C.2).

Bibliography

[1] Gregory T.A. Kovacs. *Micromachined Transducers Sourcebook*. McGraw-Hill, 1998.

[2] Julian W. Gardner, Vijay K. Varadan, and Osama O. Awadelkarim. *Microsensors MEMS and Smart Devices*. Wiley, 2001.

[3] Kensall D. Wise. Integrated sensors, MEMS, and microsystems: Reflections on a fantastic voyage. *Sensors and Actuators A: Physical*, 136(1):39 – 50, 2007.

[4] Ville Kaajakari. *Practical MEMS*. Small Gear Publishing, 2009.

[5] Marc J. Madou. *Fundamentals of Microfabrication and Nanotechnology: From MEMS to Bio-MEMS and Bio-NEMS : manufacturing techniques and applications*. Fundamentals of Microfabrication and Nanotechnology. Taylor & Francis Group, 2012.

[6] Neil Barbour. Inertial navigation sensors. Technical report, NATO Science and Technology Organisation, 2010.

[7] JD Teufel, Tobias Donner, Dale Li, JW Harlow, MS Allman, Katarina Cicak, AJ Sirois, Jed D Whittaker, KW Lehnert, and Raymond W Simmonds. Sideband cooling of micromechanical motion to the quantum ground state. *Nature*, 475(7356):359–363, 2011.

[8] Jasper Chan, TP Mayer Alegre, Amir H Safavi-Naeini, Jeff T Hill, Alex Krause, Simon Gröblacher, Markus Aspelmeyer, and Oskar Painter. Laser cooling of a nanomechanical oscillator into its quantum ground state. *Nature*, 478(7367):89–92, 2011.

[9] U. Krishnamoorthy, R.H. Olsson III, G.R. Bogart, M.S. Baker, D.W. Carr, T.P. Swiler, and P.J. Clews. In-plane MEMS-based nano-g accelerometer with sub-wavelength optical resonant sensor. *Sensors and Actuators A: Physical*, 145-146:283 – 290, 2008.

[10] Alexander G. Krause, Lin Qiang, and Painter Oskar. A high-resolution microchip optomechanical accelerometer. *Nature photonics*, 6:768–772, 2012.

[11] O. Gerberding, F.G. Cervantes, J. Melcher, and J.R. Pratt. Optomechanical reference accelerometer. *Metrology*, 52(5):654, 2015.

[12] R.P. Middlemiss, A. Samarelli, D.J. Paul, J. Hough, S. Rowan, and G.D. Hammond. Measurement of the earth tides with a mems gravimeter. *Nature*, 531(7596):614–617, 2016.

[13] W. Hortschitz, H. Steiner, M. Sachse, M. Stifter, F. Kohl, J. Schalko, A. Jachimowicz, F. Keplinger, and T. Sauter. An Optical In-Plane MEMS Vibration Sensor. *Sensors Journal, IEEE*, 11(11):2805 –2812, nov. 2011.

[14] Wilfried Hortschitz. *Hybrid MOEMS Displacement Sensor and Accelerometer*. PhD thesis, TU Wien, 2013.

[15] H. Steiner, W. Hortschitz, A. Kainz, M. Stifter, A. Jachimowicz, J. Schalko, F. Keplinger, and F. Kohl. Impact of a non-linear transfer characteristic on the evaluation of static displacements with a {MOEMS} transducer. *Procedia Engineering*, 168:1219 – 1222, 2016. Proceedings of the 30th anniversary Eurosensors Conference – Eurosensors 2016, 4-7. Sepember 2016, Budapest, Hungary.

[16] P.M.C. Morse and H. Feshbach. *Methods of theoretical physics*, volume 2. McGraw-Hill Book Company, 1953.

[17] KF Riley, MP Hobson, and SJ Bence. *Mathematical methods for physics and engineering*. AAPT, 1999.

[18] L.D. Landau and E.M. Lifschitz. *Elektrodynamik der Kontinua*, volume 8 of *Lehrbuch der Theoretischen Physik*. Akademie Verlag, 1991.

[19] L.D. Landau and E.M. Lifschitz. *Hydrodynamik*, volume 6 of *Lehrbuch der Theoretischen Physik*. Akademie Verlag, 1991.

[20] Harold Kirkham. On the measurement of stationary electric fields in air. In *Precision Electromagnetic Measurements, 2002. Conference Digest 2002 Conference on*, pages 524–525. IEEE, 2002.

[21] Behraad Bahreyni, Gayan Wijeweera, Cyrus Shafai, and Athula Rajapakse. Analysis and design of a micromachined electric-field sensor. *Journal of Microelectromechanical Systems*, 17(1):31–36, 2008.

[22] Xianxiang Chen, Chunrong Peng, and Shanhong Xia. Design of a thermally driven resonant miniature electric field sensor with feedback control. In *Nano/Micro Engineered and Molecular Systems, 2008. NEMS 2008. 3rd IEEE International Conference on*, pages 253–256. IEEE, 2008.

[23] Xianxiang Chen, Chunrong Peng, Hu Tao, Chao Ye, Qiang Bai, Shaofeng Chen, and Shanhong Xia. Thermally driven micro-electrostatic fieldmeter. *Sensors and Actuators A: Physical*, 132(2):677–682, 2006.

[24] Timothy A Denison, John S Shafran, Jinbo Kuang, and Kent H Lundberg. A self-resonant mems-based electrometer. In *Instrumentation and Measurement Technology Conference Proceedings, 2007. IMTC 2007. IEEE*, pages 1–5. IEEE, 2007.

[25] Mark N Horenstein and Patrick R Stone. A micro-aperture electrostatic field mill based on mems technology. *Journal of Electrostatics*, 51:515–521, 2001.

[26] Kent H Lundberg, John S Shafran, Jinbo Kuang, Mike Judy, and Timothy A Denison. A self-resonant mems-based electrostatic field sensor. In *American Control Conference, 2006*, pages 6–pp. IEEE, 2006.

[27] Chunrong Peng, Xianxiang Chen, Cao Ye, Hu Tao, Guoping Cui, Qiang Bai, Shaofeng Chen, and Shanhong Xia. Design and testing of a micromechanical resonant electrostatic field sensor. *Journal of Micromechanics and Microengineering*, 16(5):914, 2006.

[28] S. Schmid, L.G. Villanueva, and M.L. Roukes. *Fundamentals of Nanomechanical Resonators*. Springer International Publishing, 2016.

[29] P.K. Kundu, I.M. Cohen, and D.R. Dowling. *Fluid Mechanics*. Elsevier Science, 2015.

[30] Etienne Guyon, Jean-Pierre Hulin, Luc Petit, and Catalin D Mitescu. *Physical hydrodynamics; 2nd ed.* Oxford University Press, Oxford, 2015.

[31] W. E. Langlois. Isothermal squeeze films. *Quarterly of Applied Mathematics*, 20(2):131–150, 1962.

[32] A. Kainz, F. Keplinger, W. Hortschitz, and M. Stifter. Air damping model for laterally oscillating MOEMS vibration sensors. In *IEEE SENSORS 2014 Proceedings*, pages 590–593, Nov 2014.

[33] A. Kainz, W. Hortschitz, M. Stifter, J. Schalko, and F. Keplinger. Optimization of Passive Air Damping of MOEMS Vibration Sensors. *Procedia Engineering*, 87(0):440 – 443, 2014. EUROSENSORS 2014, the 28th European Conference on Solid-State Transducers.

[34] A. Kainz, W. Hortschitz, J. Schalko, A. Jachimowicz, and F. Keplinger. Air damping as design feature in lateral oscillators. *Sensors and Actuators A: Physical*, 236:357 – 363, 2015.

[35] A. Kainz, W. Hortschitz, H. Steiner, and F. Keplinger. Influence of holes on the damping of lateral MEMS/MOEMS oscillators. *Procedia Engineering*, 168:786 – 789, 2016. Proceedings of the 30th anniversary Eurosensors Conference – Eurosensors 2016, 4-7. Sepember 2016, Budapest, Hungary.

[36] A. Kainz, W. Hortschitz, H. Steiner, and F. Keplinger. An accurate analytical squeeze-film model for lateral MEMS/MOEMS oscillators. *Procedia Engineering*, 168:937 – 940, 2016. Proceedings of the 30th anniversary Eurosensors Conference – Eurosensors 2016, 4-7. Sepember 2016, Budapest, Hungary.

[37] A. Kainz, W. Hortschitz, H. Steiner, J. Schalko, A. Jachimowicz, and F. Keplinger. Accurate analytical model for air damping in lateral mems/moems oscillators. *Sensors and Actuators A: Physical*, 255:154 – 159, 2017.

[38] Xia Zhang and William C. Tang. Viscous air damping in laterally driven microresonators. In *Micro Electro Mechanical Systems, 1994, MEMS'94, Proceedings, IEEE Workshop on*, page 199–204, 1994.

[39] Young-Ho Cho, Albert P. Pisano, and Roger T. Howe. Viscous damping model for laterally oscillating microstructures. *Journal of Microelectromechanical Systems*, 3(2):81–87, 1994.

[40] Timo Veijola and Marek Turowski. Compact damping models for laterally moving microstructures with gas-rarefaction effects. *Journal of Microelectromechanical Systems*, 10(2):263–273, 2001.

[41] Po-Ching Yen and Yao-Joe Yang. Macromodels of 3D lateral viscous damping effects for MEMS devices. In *TRANSDUCERS, Solid-State Sensors, Actuators and Microsystems, 12th International Conference on, 2003*, volume 2, pages 1848–1851 vol.2, 2003.

[42] Wenjing Ye, Xin Wang, Werner Hemmert, Dennis Freeman, and Jacob White. Air damping in laterally oscillating microresonators: A numerical and experimental study. *Journal of Microelectromechanical Systems*, 12(5):557–566, 2003.

[43] Y.-JJ Yang and P.-C. Yen. An efficient macromodeling methodology for lateral air damping effects. *Journal of Microelectromechanical Systems*, 14(4):812–828, 2005.

[44] JJ. Blech. On isothermal squeeze films. *J. of Lubrication Tech.*, 105(4):615–620, 1983.

[45] Timo Veijola, Heikki Kuisma, Juha Lahdenperä, and Tapani Ryhänen. Equivalent-circuit model of the squeezed gas film in a silicon accelerometer. *Sensors and Actuators A: Physical*, 48(3):239 – 248, 1995.

[46] Robert B. Darling, Chris Hivick, and Jianyang Xu. Compact analytical modeling of squeeze film damping with arbitrary venting conditions using a green's function approach. *Sensors and Actuators A: Physical*, 70(1):32 – 41, 1998.

[47] M. Bao and H. Yang. Squeeze film air damping in MEMS. *Sensors and Actuators A*, 136:3–27, 2007.

[48] Timo Veijola and Anu Lehtovuori. Numerical and analytical modelling of trapped gas in micromechanical squeeze-film dampers. *Journal of Sound and Vibration*, 319(1–2):606 – 621, 2009.

[49] P.M.C. Morse and H. Feshbach. *Methods of theoretical physics*, volume 1. McGraw-Hill Book Company, 1953.

[50] Jörg Encke, Wilfried Hortschitz, Andreas Kainz, Harald Steiner, Franz Keplinger, and Thilo Sauter. A miniaturized linear shaker system for MEMS sensor characterization. In *SPIE Microtechnologies*, volume 8763, pages 876315–876315–6, 2013.

[51] Georg A. Reider. *Photonik*. Springer-Verlag Wien, 2012.

[52] W. Demtröder. *Experimentalphysik 2*. Experimentalphysik / Wolfgang Demtroeder. Springer Berlin Heidelberg, 2008.

[53] GR Morrison. *Diffractive X-ray optics*. Institute of Physics Publishing, Bristol, 1993.

[54] Alan G Michette. *Optical systems for soft X rays*. Springer, 1986.

[55] David Attwood and Anne Sakdinawat. *X-rays and Extreme Ultraviolet Radiation: Principles and Applications*. Cambridge university press, 2016.

[56] M. Windisch. Untersuchung zur Erhöhung der Sensitivität eines optischen MEMS-Vibrations-Sensors. Technical report, Institute of Sensor and Actuator Systems, 2016.

[57] Marcin Kielar, Olivier Dhez, Gilles Pecastaings, Arnaud Curutchet, and Lionel Hirsch. Long-term stable organic photodetectors with ultra low dark currents for high detectivity applications. *Scientific Reports*, 6, 2016.

[58] Mark Johnson. *Photodetection and Measurement: Maximizing Performance in Optical Systems*. McGraw Hill Professional, 2003.

[59] RH Friend, RW Gymer, AB Holmes, JH Burroughes, RN Marks, CDDC Taliani, DDC Bradley, DA Dos Santos, JL Bredas, M Lögdlund, et al. Electroluminescence in conjugated polymers. *Nature*, 397(6715):121–128, 1999.

[60] N Thejo Kalyani and SJ Dhoble. Organic light emitting diodes: Energy saving lighting technology—a review. *Renewable and Sustainable Energy Reviews*, 16(5):2696–2723, 2012.

[61] Graeme Williams, Christopher Backhouse, and Hany Aziz. Integration of organic light emitting diodes and organic photodetectors for lab-on-a-chip bio-detection systems. *Electronics*, 3(1):43–75, 2014.

[62] Ross D Jansen-van Vuuren, Ardalan Armin, Ajay K Pandey, Paul L Burn, and Paul Meredith. Organic photodiodes: the future of full color detection and image sensing. *Advanced Materials*, 28(24):4766–4802, 2016.

[63] Thilo Sauter, Wilfried Hortschitz, Harald Steiner, Michael Stifter, Hsin Chiao, Hsiao Wen Zan, Hsin-Fei Meng, and Paul Chao. Making optical mems sensors more compact using organic light sources and detectors. In *Emerging Technology and Factory Automation (ETFA), 2014 IEEE*, pages 1–4. IEEE, 2014.

[64] A. Kainz, W. Hortschitz, H. Steiner, Y.H. Hong, C.H. Chen, H.W. Zan, H.F. Meng, T. Sauter, and F. Keplinger. MOEMS Vibration Sensor with Organic Semiconductor Readout. *Procedia Engineering*, 168:1253 – 1256, 2016. Proceedings of the 30th anniversary Eurosensors Conference – Eurosensors 2016, 4-7. Sepember 2016, Budapest, Hungary.

[65] Günther Hammer. Inertial Sensing of Heart Rate and Breath based on MOEMS, OLED and OPD (working title). Master's thesis, TU Wien, 2017.

[66] Private communication with Prof. H.W. Zan and Prof. H.F. Meng, 2017.

[67] E. Pierce. Atmospheric Electricity-Some Themes. *Bulletin of the American Meteorological Society*, 55(10):1186–1194, 1974.

[68] Thomas C. Marshall, William Rison, W. David Rust, Maribeth Stolzenburg, John C. Willett, and William P. Winn. Rocket and balloon observations of electric field in two thunderstorms. *Journal of Geophysical Research: Atmospheres*, 100(D10):20815–20828, 1995.

[69] Maribeth Stolzenburg, Thomas C. Marshall, and Paul R. Krehbiel. Duration and extent of large electric fields in a thunderstorm anvil cloud after the last lightning. *Journal of Geophysical Research: Atmospheres*, 115(D19):n/a–n/a, 2010. D19202.

[70] M. Takeda, M. Yamauchi, M. Makino, and T. Owada. Initial effect of the fukushima accident on atmospheric electricity. *Geophysical Research Letters*, 38(15):n/a–n/a, 2011. L15811.

[71] Earle Williams and Eugene Mareev. Recent progress on the global electrical circuit. *Atmospheric Research*, 135:208–227, 2014.

[72] Gayan Wijeweera, Behraad Bahreyni, Cyrus Shafai, Athula Rajapakse, and David R Swatek. Micromachined electric-field sensor to measure ac and dc fields in power systems. *IEEE Transactions on Power Delivery*, 24(3):988–995, 2009.

[73] D.A. Hill and Kanda M. *The measurement, instrumentation and sensors handbook XXV, ch. 47.* CRC Press, 1999.

[74] Chunrong Peng, Pengfei Yang, Haiyan Zhang, Xin Guo, and Shanhong Xia. Design of a soi mems resonant electric field sensor for power engineering applications. In *Sensors, 2010 IEEE*, pages 1183–1186. IEEE, 2010.

[75] Georges Roussy, Kodjo Agbossou, and Bernard Dichtel. Vector electric field measurement using a non-interfering sensor. *Measurement Science and Technology*, 11(8):1145, 2000.

[76] TE Batchman and George Gimpelson. An implantable electric-field probe of submillirneter dimensions. *IEEE transactions on microwave theory and techniques*, 31(9):745–751, 1983.

[77] Franklin C Chiang, Patrick Pribyl, Walter Gekelman, Bertrand Lefebvre, Li-Jen Chen, and Jack W Judy. Microfabricated flexible electrodes for multiaxis sensing in the large plasma device at ucla. *IEEE Transactions on Plasma Science*, 39(6):1507–1515, 2011.

[78] Georg Gustafsson, M André, T Carozzi, Anders I Eriksson, C-G Fälthammar, R Grard, G Holmgren, JA Holtet, N Ivchenko, Tomas Karlsson, et al. First results of electric field and density observations by cluster efw based on initial months of operation. *Annales Geophysicae*, 19(10/12):1219–1240, 2001.

[79] Jean-Jacques Berthelier, Michel Godefroy, Frédéric Leblanc, M Malingre, Michel Menvielle, D Lagoutte, JY Brochot, F Colin, F Elie, C Legendre, et al. Ice, the electric field experiment on demeter. *Planetary and Space Science*, 54(5):456–471, 2006.

[80] C Barthod, M Passard, M Fortin, C Galez, and J Bouillot. Design and optimization of an optical high electric field sensor. In *Precision Electromagnetic Measurements Digest, 2000 Conference on*, pages 423–424. IEEE, 2000.

[81] Megumu Miki, Vladimir A Rakov, Keith J Rambo, George H Schnetzer, and Martin A Uman. Electric fields near triggered lightning channels measured with pockels sensors. *Journal of Geophysical Research: Atmospheres*, 107(D16), 2002.

[82] Bartos Chmielak, Michael Waldow, Christopher Matheisen, Christian Ripperda, Jens Bolten, Thorsten Wahlbrink, Michael Nagel, Florian Merget, and Heinrich Kurz. Pockels effect based fully integrated, strained silicon electro-optic modulator. *Optics express*, 19(18):17212–17219, 2011.

[83] Takashi Maeno and Tatsuo Takada. Electric field measurement in liquid dielectrics using a combination of ac voltage modulation and a small retardation angle. *IEEE Transactions on Electrical insulation*, 22(4):503–508, 1987.

[84] Allen H Rose, Shelley M Etzel, and Kent B Rochford. Optical fiber current sensors in high electric field environments. *Journal of lightwave technology*, 17(6):1042–1048, 1999.

[85] D Perry, S Chadderdon, Richard Gibson, B Shreeve, Richard H Selfridge, Stephen M Schultz, Wen C Wang, Richard Forber, and J Luo. Electro-optic polymer electric field sensor. In *SPIE Smart Structures and Materials+ Nondestructive Evaluation and Health Monitoring*, pages 79820Q–79820Q. International Society for Optics and Photonics, 2011.

[86] Georg Traxler. Optimization of the electric field microsensor design based on FEM simulations. Master's thesis, TU Wien, 2016.

[87] Euan J. Boyd, Li Li, Robert Blue, and Deepak Uttamchandani. Measurement of the temperature coefficient of Young's modulus of single crystal silicon and 3c silicon carbide below 273 K using micro-cantilevers. *Sensors and Actuators A: Physical*, 198:75–80, August 2013.

[88] Christine Vehar Jutte and Sridhar Kota. Design of nonlinear springs for prescribed load-displacement functions. *Journal of Mechanical Design*, 130(8):081403, 2008.

[89] W. Hortschitz, H. Steiner, M. Sachse, M. Stifter, F. Kohl, J. Schalko, A. Jachimowicz, F. Keplinger, and T. Sauter. Robust precision position detection with an optical mems hybrid device. *IEEE Transactions on Industrial Electronics*, 59(12):4855–4862, Dec 2012.